1-1-2003

An investigation of the interaction between a travelling shock wave and a solid rocket motor nozzle

Harmanjit Singh Chopra
Ryerson University

AN INVESTIGATION OF THE INTERACTION BETWEEN A TRAVELLING SHOCK WAVE AND A SOLID ROCKET MOTOR NOZZLE

by

Harmanjit Singh Chopra,
B.E. (Mechanical Engineering),
University of Pune (India), 2000

A thesis
presented to Ryerson University
in partial fulfillment of the
requirements for the degree of
Master of Applied Science
in the program of
Mechanical Engineering

Toronto, Ontario, Canada, 2003

Author's declaration

I hereby declare that I am the sole author of this thesis.

I authorize Ryerson University to lend this thesis to other institutions or individuals for the purpose of scholarly research.

Harmanjit Singh Chopra

I further authorize Ryerson University to reproduce this thesis by photocopying or by other means, in total or in part, at the request of other institutions or individuals for the purpose of scholarly research.

Harmanjit Singh Chopra

Borrower's page

Ryerson University requires the signatures of all persons using or photocopying this thesis. Please sign below, and give address and date.

Name	Address	Date

Abstract

AN INVESTIGATION OF THE INTERACTION BETWEEN A TRAVELLING SHOCK WAVE AND A SOLID ROCKET MOTOR NOZZLE

© Harmanjit Singh Chopra, 2003
Master of Applied Science
in the program of
Mechanical Engineering
Ryerson University

A gasdynamic mechanism has been identified as a potential source of combustion instability in solid-propellant rocket motors (SRMs). This mechanism involves the reinforcement of a reflected shock wave in the nozzle convergence region of an SRM's exhaust nozzle.

A shock tube apparatus was developed for the experimental component of this study. Various factors, such as the effect of different nozzle geometries and driven channel pressures, were examined. Also, a model of the shock tube was developed for computational fluid dynamics (CFD) simulations. These simulations were generated for comparison with the experimental results and to provide additional information regarding the nature of the flow behaviour.

Experimental and numerical pressure-time profiles confirm the appearance of transient radial wave activity following the initial incidence of the normal shock wave on the convergence region of the nozzle. The results establish that the strength of this activity is markedly dependent upon the nozzle convergence wall angle and the location within the shock tube.

Acknowledgements

I wish to express my sincere gratitude to Dr. David Greatrix (thesis supervisor) and Dr. Greg Kawall (thesis co-supervisor) for their continuous guidance throughout my graduate studies. Financial aid in the form of a graduate stipend provided by Dr. David Greatrix and Dr. Greg Kawall is acknowledged here with thanks. Dr. David Greatrix helped me in providing input concerning the numerical study and in understanding of the various aspects of the theory associated with solid propellant rocket motors. I gratefully acknowledge Dr. Greg Kawall for his input with regard to conducting the experiments. Patience and devotion shown by my supervisors towards helping me complete my thesis cannot be expressed in words. It was indeed a pleasure to work under their supervision.

Special thanks are owed to Jerry Karpynczyk and Nick Stina for contributing to the design and construction of the experimental apparatus. Jerry Karpynczyk always kept my spirits high. His positive attitude towards work and his jokes are highly appreciated. Appreciation is also extended to Stephen Mauthe for helping me in conducting various calibrations and experiments.

I would also like to thank my parents and sisters, my uncle and his family, and Avinash Kaur for their never-ending support and encouragement to pursue my graduate studies.

Finally, I would like to thank God, without whose mercy I would not have finished my thesis in the given stipulated time. **THANK YOU GOD.**

Table of Contents

List of Figures

Nomenclature

Arabic

a	local gas speed of sound
a_t	speed of sound at throat
A	local cross-sectional area of the channel
A_e	cross-sectional area at the exit of the nozzle
A_t	cross-sectional area at throat
B	constant
c	point representing the collision of the reflected shock wave front and the contact surface
c_p	specific heat at constant pressure
d	local diameter of the channel
d_e	diameter at the exit of the nozzle
d_t	diameter at throat
f_{1R}	oscillation frequency of the radial pressure wave
H_2	hydrogen
He	helium
h	local gas enthalpy
l	length of the driven channel
M	local Mach number
M_e	Mach number at the exit of the nozzle
M_R	reflected shock wave Mach number
M_R^*	reflected shock wave reference Mach number
M_S	incident shock wave Mach number
M_S^*	incident shock wave reference Mach number
M_t	Mach number at throat
$\dot{m}_{in}$	mass flow rate

p local gas static pressure

p_{atm} atmospheric pressure

p_c combustion chamber pressure

p_e pressure at the exit of the nozzle

p_t pressure at throat

Q volumetric flow rate

R specific gas constant

t flow time

t_2 time taken by the incident shock wave to reach the nozzle entrance

t_c time at which the contact surface and the reflected shock wave front collide

$t_{CW\text{-}A}$ expected time of arrival of new compression waves at the transducer location

$t_{CWR\text{-}B}$ expected time of arrival of reflected waves generated from new compression waves at the transducer location

t_{ex} time taken by the expansion wave front to reach the reservoir end

$t_{i_{expected}}$ expected time of arrival of the incident shock wave front at any local distance along the axis of the shock tube

$t_{R_{expected}}$ expected time of arrival of the reflected shock wave front at any local distance along the axis of the shock tube

$t_{R_{\substack{expected \\ at \\ collision}}}$ expected time of collision of reflected shock wave front with contact surface

t_{test} time taken by the reflected shock wave to move upstream from the nozzle entrance and collide with the contact surface

T local gas absolute temperature

T_e absolute temperature at the exit of the nozzle

T_t absolute temperature at throat

u local flow velocity

u_e velocity at the exit of the nozzle

u_t velocity at throat

Δu_2 velocity of the induced mass flow behind the incident shock wave

V_{cs} velocity of the contact surface

V_S velocity of the incident shock wave

V_S^* incident shock wave reference velocity

V_R velocity of the reflected shock wave

$V_{R_{new}}$ increased mean velocity of the reflected shock wave front

x local distance along the axis of the shock tube

x_c distance from the diaphragm station at which the contact surface and the reflected shock wave front collide

Δx_R distance travelled by the reflected shock wave front from the nozzle entrance along the axis of the shock tube

Greek

γ local gas specific heat ratio

ρ local gas density

Chapter 1 Introduction

1.1 Background

Under certain conditions, solid-propellant rocket motors (SRMs) may encounter problems related to combustion instability.[1,2,3,4,5,6] These problems arise when an SRM is disturbed from its stable operating condition due to various sources, such as small pieces of propellant or wall insulation passing through the nozzle of an SRM, abrupt burning of reactants in the propellant, etc.[7,8,9] In addition, external pulses, such as those applied for static motor testing, a nearby explosion, etc.,[10,11] may trigger combustion instability in an SRM.

Internal flow oscillations caused by disturbances disrupt the steady-state combustion process taking place inside the combustion chamber of an SRM, with axial pressure waves travelling back and forth along the length of the chamber. This unsteady flow field interacts with the combustion process and can cause an increase in the propellant burning rate.[12] Situations may arise where the initial pressure waves grow rather than decay. As a result, the thrust and base chamber pressure may rise above the normal level, and this, in conjunction with strong motor structural vibrations,[3,4,5] may lead to poor performance of the motor.[13] Moreover, if the base chamber pressure rises beyond the structural design limit of the motor, structural failure of the chamber will occur, leading to the loss of the motor. Thus, the strength of the pressure waves may be sufficient to cause some concern for the safe operation of an SRM. Considerable efforts have been made, and various research endeavours are still in progress, to model the internal ballistics of rocket motors,[9,11,14] in order to help explain the phenomena that lead to combustion instability.

It cannot be said that a particular factor alone is a prime cause of this sort of instability; rather, it is probably a combination of various factors that is responsible. These factors may include higher than normal mean chamber pressures,[6,8] triggering pulse time lag after ignition,[6] propellant burning rate,[7] propellant grain shape and internal area transition,[9,15,16] length of combustion chamber,[16,17] amplitude and shape of triggering pulse,[15,18] type of propellant,[19] percentage of stability additives in the propellant,[15,16,18]

nozzle throat to grain-port area ratio,[9,12] motor gas cavity and structural oscillation frequency,[18] and motor mass.[7]

There are two types of combustion instabilities:[8] linear and non-linear. In the linear case, a small amplitude pulse triggers the flow oscillations within the combustion chamber of an SRM; whereas, in the non-linear case, a larger amplitude pulse triggers the development of sustained waves. At present, the focus is on non-linear combustion instability. This type of instability will be present in an SRM if there exist high-amplitude shock-fronted pressure waves.[12,20] Longitudinal[14] (i.e., axial) and/or transverse[21] (i.e., radial or tangential) waves are generally encountered during the unstable operation of a motor. Longitudinal waves traverse back and forth along the long axis of the motor; whereas transverse waves travel laterally at given locations along the motor.

Over the past years, a number of driving mechanisms have been identified as potential sources for symptoms typically associated with non-linear axial combustion instability. These mechanisms can range from a frequency-dependent, pressure-coupled and velocity-coupled combustion response to the flow above the propellant's burning surface,[22] to cyclic acceleration-augmented burning resulting from local propellant grain/casing structural vibration.[5] Additionally, observation of experimental pulsed-firing pressure-time profiles at higher than normal mean chamber pressures and propellant base burning rates suggests a potential gasdynamic mechanism.[3] This mechanism involves reinforcement of a reflected shock wave in the region of the exhaust nozzle of an SRM and is the main focus of the present investigation.

The most fundamental and simplest configuration of an SRM is the standard radially-burning cylindrical-grain rocket motor,[23] shown in Fig. 1.1. The motor consists of a combustion chamber and a converging-diverging nozzle. The combustion chamber is essentially a high-pressure tank containing the solid propellant, called the grain, and sufficient empty space to allow for proper combustion and internal flow. The walls of the chamber are sufficiently thick and internally coated with an insulating material to withstand thermal stresses from high-temperature combustion, in addition to the high-pressure loading.

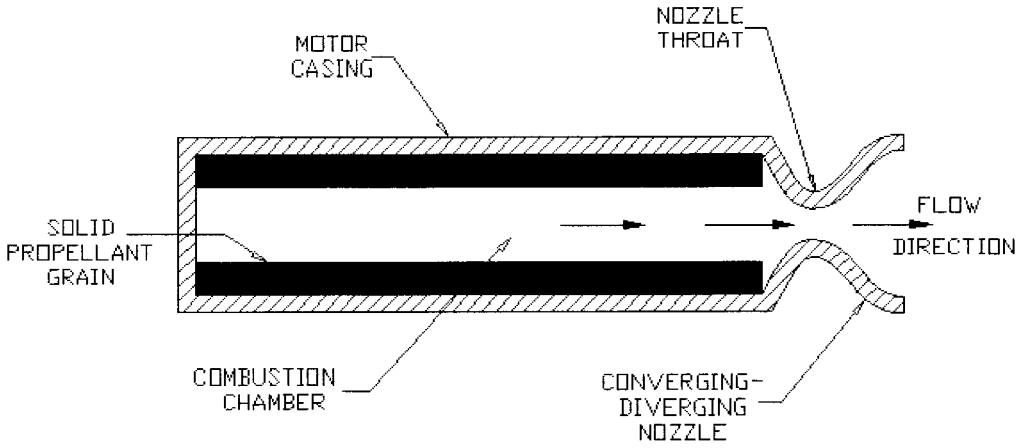

Figure 1.1 Cylindrical grain solid-propellant rocket motor.

Once the surface of the propellant is ignited (through an igniter), the burning surface recedes in a direction perpendicular to the surface. This process produces high-pressure and high-temperature combustion products (generally gases, but sometimes a small fraction of condensed particles) inside the chamber. These hot gases are expanded through the nozzle so as to produce thrust. The combustion chamber pressure p_c rises to a quasi-equilibrium state after ignition, during which the main firing phase occurs, until propellant burnout, as shown in Fig. 1.2.[24] The illustrated head-end pressure-time profile is referred to as progressive, with pressure, thrust, and burning surface area increasing[25] with time in the main firing phase.

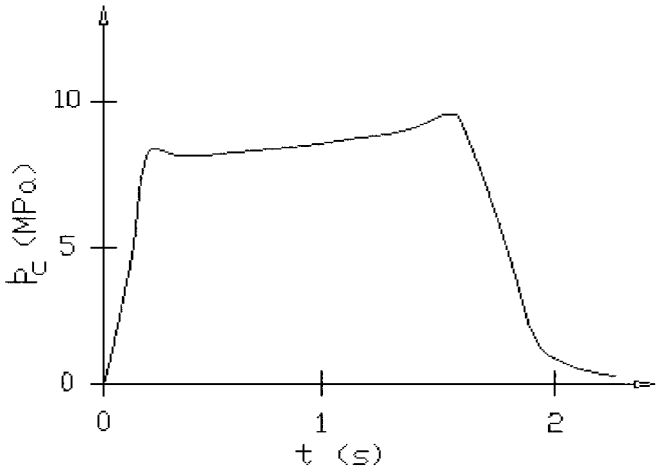

Figure 1.2 Variation of combustion chamber head-end pressure with burning time for normal operation of a cylindrical-grain SRM.

At a given time during the main firing phase, the pressure and the temperature of the gas decrease whereas the velocity increases as a function of motor length, moving from the motor's head end to the aft nozzle entry, as shown in Fig. 1.3[2]. As noted earlier, a disturbance can potentially move the internal ballistic operation away from the nominal condition described above, with a travelling axial compression wave superimposed on the base internal flow, reflecting and re-reflecting from the nozzle (and head end).

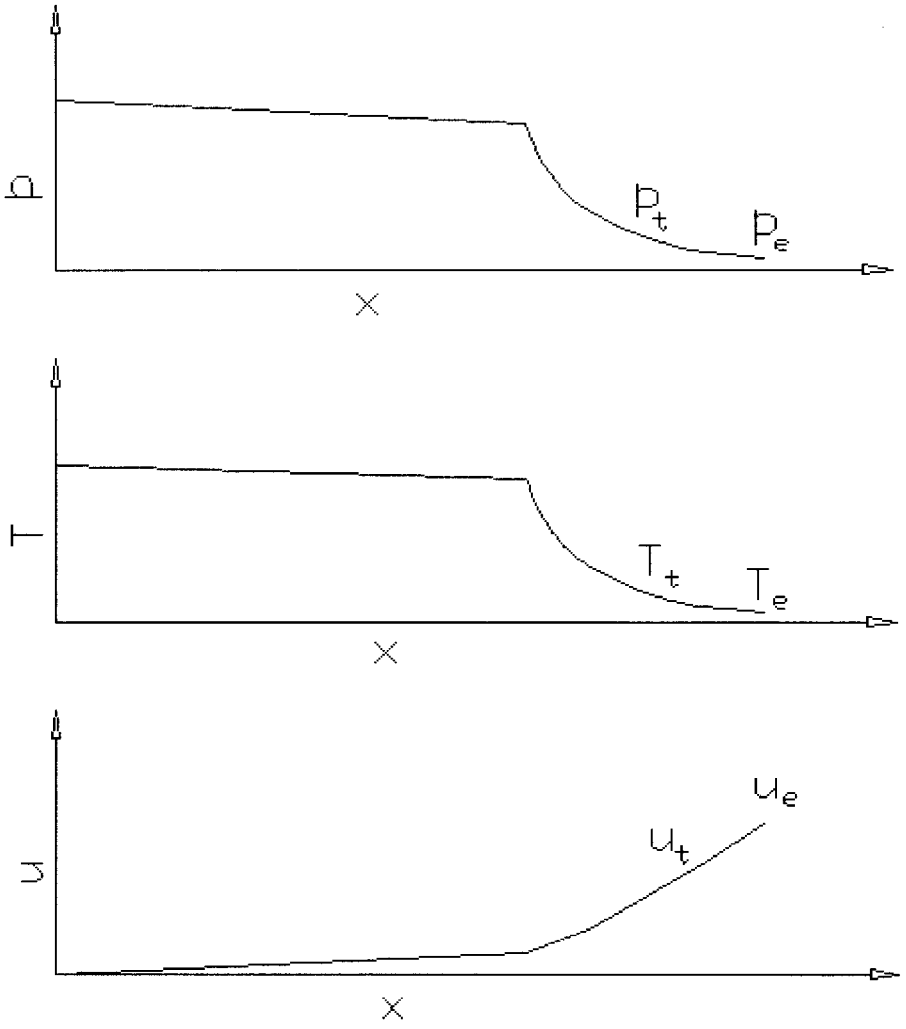

Figure 1.3 Distributions of pressure, temperature, and velocity along the motor axis at a given time in the firing.

1.2 Present Study

An experimental and numerical study has been undertaken to examine various aspects surrounding the interaction of an incident travelling normal shock wave on an SRM's exhaust nozzle, in order to identify any potential gasdynamic mechanism of pressure wave reinforcement. A cold-flow experiment, based on a hybrid shock tube scheme, with air as the working fluid, has been developed. Because of the limitation of the supply air pressure, the shock tube apparatus was operated at substantially lower pressures than those typically occurring in SRMs. There was an expectation that at least some of the key aspects of the flow behaviour experienced in SRMs would be evident in a lower pressure situation. Several experimental runs/firings with a converging-diverging nozzle and an orifice plate (as a limiting case of the converging-diverging nozzle) located at the channel exit and at different channel pressures have been conducted.

Computational fluid dynamics (CFD) simulations have been generated via FLUENT Version 6.0 for comparison with the experimental results and to provide additional information with respect to the nature of the flow. The simulations involve converging-diverging nozzles with 30°, 45°, and 60° convergence half-cone angles, and orifice plates having 0° and 45° inclinations of the orifice.

Chapter 2 Experimental Apparatus

2.1 Introduction to Shock Tube Analysis

A shock tube[26,27] is a laboratory instrument used to generate shock waves under controlled conditions. The shock tube has become an extremely important laboratory instrument for the study of non-stationary problems in fluid dynamics. Shock tubes have also been used for testing of supersonic bodies, hypersonic entry vehicles, and understanding of high-speed compressible flows. Typical shock tube experiments are conducted for the study of various flow properties and phenomena related to shock waves, such as gas density, pressure, temperature, Mach number and chemical kinetics. In addition, a shock tube apparatus offers flexibility in terms of its material, physical size and operating parameters. As mentioned in Section 1.2, a customized shock tube is used for the current investigation. The description of this tube is given below.

The shock tube consists of a long tube having a constant cross-section, with a converging-diverging nozzle at one end. A diaphragm separates a region of high-pressure gas at pressure p_4 (Region 4) from a region of low-pressure gas at pressure p_1 (Region 1) as shown in Fig. 2.1.

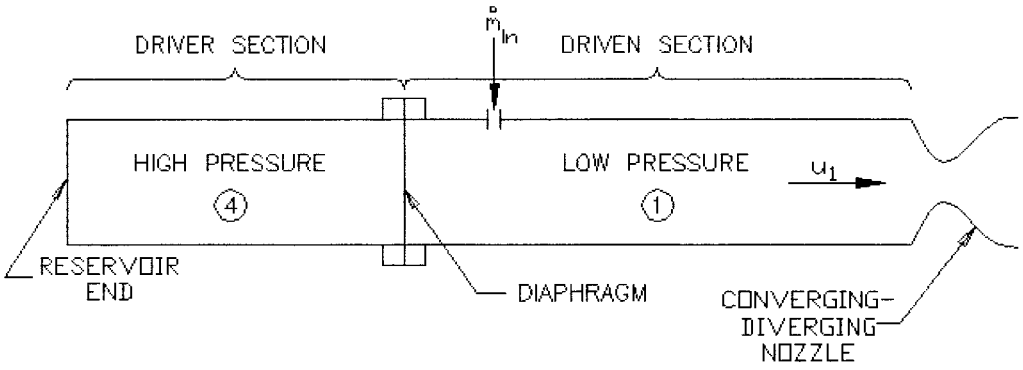

Figure 2.1 Graphical representation of a shock tube.

The gases in the Regions 1 and 4 can be at different temperatures and can have different molecular weights. However, for this particular study, air at room temperature is the

working fluid. The initial pressure distribution inside the shock tube is depicted in Fig. 2.2.[28]

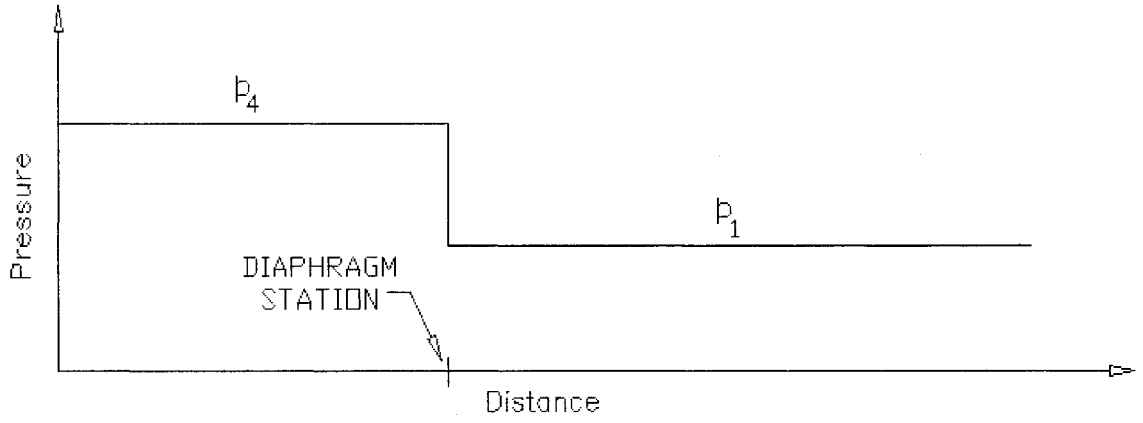

Figure 2.2 Initial pressure distribution along the length of a shock tube.

In Fig. 2.1, Region 4 is called the driver section and Region 1 is called the driven section. The difference in pressure between p_4 and p_1 determines the load on the diaphragm, as well as the shock strength. When the diaphragm is broken by electrical or mechanical means, a (compression) shock wave is propagated into Region 1 and an expansion (or rarefaction) wave into Region 4, as depicted in Fig. 2.3.

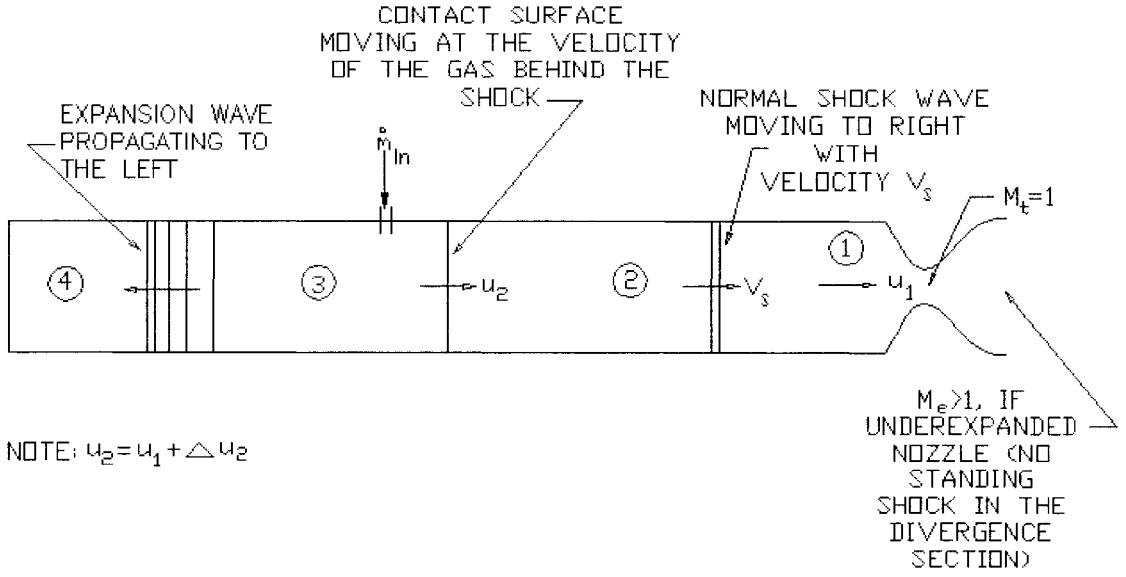

Figure 2.3 Flow inside the shock tube after the diaphragm is broken.

As the normal shock wave propagates to the right with velocity V_S, the pressure of the gas behind it, i.e., in Region 2, increases, and a mass flow with a velocity Δu_2 superimposed on the base flow at velocity u_1, is induced, as depicted in Fig. 2.3. The interface between the driver and the driven gases is called the contact surface, which also moves with velocity $u_2 (= u_1 + \Delta u_2)$. The pressure and velocity in Regions 2 and 3 remain the same, i.e., $p_3 = p_2$ and $u_3 = u_2$. The expansion wave propagates to the left, smoothly and continuously decreasing the pressure in Region 4 to the lower value p_3 behind the expansion wave, as depicted in Fig. 2.4.[28]

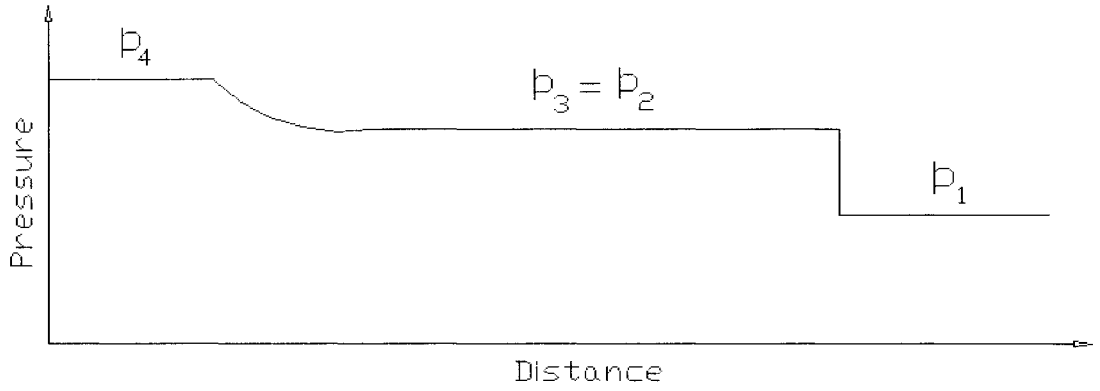

Figure 2.4 Pressure distribution inside the shock tube after the diaphragm is broken.

Before the basic flow expressions for the customized shock tube are presented, it should be noted that the shock-tube theory involves the underlying assumption of quasi-one-dimensional and inviscid flow. In the current investigation, transient two-dimensional flow behaviour may be significant and must be accounted for, with respect to a shock wave reflecting from a choked nozzle. The general analytical approach of a conventional, closed-end shock tube[27,28] can be applied for the shock wave reflection from a converging-diverging nozzle, with the understanding that the estimated flow conditions may only apply at quasi-equilibrium, i.e., after transient behaviour has settled.

It is clear from Fig. 2.3 that the velocity of the gas ahead of the incident shock wave, relative to the wave, will be $(V_S - u_1)$, and the velocity of the gas behind the incident shock wave, relative to the wave, will be $(V_S - u_2)$. Therefore, one can write the

continuity, momentum, and energy equations for a moving shock wave superimposed on the base flow moving at velocity u_1 as

$$\rho_1(V_S - u_1) = \rho_2(V_S - u_2), \tag{2.1}$$

where ρ is the gas density,

$$p_1 + \rho_1(V_S - u_1)^2 = p_2 + \rho_2(V_S - u_2)^2, \tag{2.2}$$

$$h_1 + \frac{(V_S - u_1)^2}{2} = h_2 + \frac{(V_S - u_2)^2}{2}, \tag{2.3}$$

where h is enthalpy of the gas.

For the case of a calorically perfect gas, the following relationships apply:

$$p = \rho RT, \tag{2.4}$$

where R is the specific gas constant and T is the absolute temperature of the gas,

$$dh = c_p dT, \tag{2.5}$$

where c_p is the specific heat at constant pressure,

and

$$a^2 = \gamma RT, \tag{2.6}$$

where a is the speed of sound and γ is the specific heat ratio. In addition, the stagnation temperature remains constant. The stagnation temperature condition[29,30] is written as

$$T_t = T\left(1 + \frac{\gamma - 1}{2}\left(\frac{V_S}{a_1} - \frac{u_1}{a_1}\right)^2\right) \tag{2.7}$$

With the introduction of Mach number, i.e.,

$$M = \frac{u}{a},$$

Equation (2.7) becomes

$$T_t = T\left(1 + \frac{\gamma - 1}{2}(M_S - M_1)^2\right) \tag{2.8}$$

Using Equation (2.8) along with Equations (2.4),[31] (2.5),[31] and (2.6),[31] one can transform Equation (2.3) to

$$T_1\left(1 + \frac{\gamma - 1}{2}(M_S - M_1)^2\right) = T_2\left(1 + \frac{\gamma - 1}{2}(M_S - M_2)^2\right) \tag{2.9}$$

Also, Equation (2.2) becomes

$$p_1(1+\gamma(M_S-M_1)^2)=p_2(1+\gamma(M_S-M_2)^2) \tag{2.10}$$

Combining Equations (2.9) and (2.10) with Equation (2.1) yields

$$\frac{(M_S-M_1)^2}{1+\gamma(M_S-M_1)^2}\sqrt{1+\left(\frac{\gamma-1}{2}\right)(M_S-M_1)^2}=\frac{(M_S-M_2)^2}{1+\gamma(M_S-M_2)^2}\sqrt{1+\left(\frac{\gamma-1}{2}\right)(M_S-M_2)^2}$$

Squaring both sides, one obtains

$$\frac{(M_S-M_1)^2\left(1+\left(\frac{\gamma-1}{2}\right)(M_S-M_1)^2\right)}{\left(1+\gamma(M_S-M_1)^2\right)^2}=\frac{(M_S-M_2)^2\left(1+\left(\frac{\gamma-1}{2}\right)(M_S-M_2)^2\right)}{\left(1+\gamma(M_S-M_2)^2\right)^2} \tag{2.11}$$

Expressing Equation (2.11) in terms of a quadratic equation in $(M_S-M_2)^2$, one obtains

$$(M_S-M_2)^4\left(\frac{\gamma-1}{2}-\gamma^2B\right)+(M_S-M_2)^2(1-2\gamma B)-B=0 \tag{2.12}$$

where,

$$B=\frac{(M_S-M_1)^2\left(1+\left(\frac{\gamma-1}{2}\right)(M_S-M_1)^2\right)}{\left(1+\gamma(M_S-M_1)^2\right)^2}$$

Solving Equation (2.12), one obtains

$$(M_S-M_2)^2=\frac{(M_S-M_1)^2+\frac{2}{\gamma-1}}{\frac{2\gamma}{\gamma-1}(M_S-M_1)^2-1} \tag{2.13}$$

Returning back to Equation (2.9), one can write the temperature ratio across the incident shock wave as

$$\frac{T_2}{T_1}=\frac{\left(1+\frac{\gamma-1}{2}(M_S-M_1)^2\right)}{\left(1+\frac{\gamma-1}{2}(M_S-M_2)^2\right)} \tag{2.14}$$

Substituting Equation (2.13) in Equation (2.14) and simplifying, one obtains

$$\frac{T_2}{T_1}=\frac{\left(1+\frac{\gamma-1}{2}(M_S-M_1)^2\right)\left(\frac{2\gamma}{\gamma-1}(M_S-M_1)^2-1\right)}{(M_S-M_1)^2\left(\frac{2\gamma}{\gamma-1}+\frac{\gamma-1}{2}\right)}$$

or
$$\frac{T_2}{T_1} = \frac{\left(1+\frac{\gamma-1}{2}(M_S^*)^2\right)\left(\frac{2\gamma}{\gamma-1}(M_S^*)^2-1\right)}{(M_S^*)^2\left(\frac{(\gamma+1)^2}{2(\gamma-1)}\right)}, \tag{2.15}$$

where,

$$M_S^* = M_S - M_1 \tag{2.16}$$

From Equation (2.10), one can write the pressure ratio across the incident shock wave as

$$\frac{p_2}{p_1} = \frac{(1+\gamma(M_S-M_1)^2)}{(1+\gamma(M_S-M_2)^2)} \tag{2.17}$$

Substituting Equation (2.13) in Equation (2.17) yields

$$\frac{p_2}{p_1} = \frac{2\gamma(M_S^*)^2-(\gamma-1)}{\gamma+1} \tag{2.18}$$

Re-arranging Equation (2.18), one obtains

$$M_S^* = \frac{V_S^*}{a_1} = \sqrt{\frac{\gamma+1}{2\gamma}\left(\frac{p_2}{p_1}\right)+\frac{\gamma-1}{2\gamma}} \tag{2.19}$$

Finally, from Equation (2.1), one can write the density ratio across the incident shock wave as

$$\frac{\rho_2}{\rho_1} = \frac{V_S-u_1}{V_S-u_2}$$

or
$$\frac{\rho_2}{\rho_1} = \frac{M_S-M_1}{M_S-M_2}\sqrt{\frac{T_1}{T_2}} \tag{2.20}$$

Substituting Equations (2.13) and (2.15) in Equation (2.20) yields

$$\frac{\rho_2}{\rho_1} = \frac{(\gamma+1)(M_S-M_1)^2}{2+(\gamma-1)(M_S-M_1)^2}$$

or
$$\frac{\rho_2}{\rho_1} = \frac{(\gamma+1)(M_S^*)^2}{2+(\gamma-1)(M_S^*)^2} \tag{2.21}$$

Also, the speed of sound ratio[31] across the incident shock wave can be written as

$$\frac{a_2}{a_1} = \sqrt{\frac{T_2}{T_1}} \tag{2.22}$$

It should be noted that the Mach number M_1 is a function of channel and nozzle throat cross-sectional areas. The relevant relationship is given by

$$\frac{A_1}{A_t} = \frac{1}{M_1}\left(\frac{2+(\gamma-1)M_1^{\,2}}{\gamma+1}\right)^{\frac{\gamma+1}{2(\gamma-1)}} \tag{2.23}$$

Equation (2.23)[31] is called the Area Mach number relation, applied between Region 1 and the choked nozzle throat. Equations (2.15), (2.18), (2.21), and (2.22) pertain to properties of a moving normal shock wave superimposed on a base flow with velocity u_1.

Putting $M_S^{\,*} = M_S - \frac{u_1}{a_1}$ in Equation (2.18), simplifying for shock Mach number M_S, one obtains

$$M_S = \sqrt{\left(\frac{p_2}{p_1}-1\right)\left(\frac{\gamma+1}{2\gamma}\right)+1} + \frac{u_1}{a_1} \tag{2.24}$$

Re-arranging Equation (2.19), one obtains

$$V_S^{\,*} = a_1\sqrt{\frac{\gamma+1}{2\gamma}\left(\frac{p_2}{p_1}\right)+\frac{\gamma-1}{2\gamma}} \tag{2.25}$$

In addition to the above set of equations, one can also determine the induced gas velocity behind the incident shock wave from Fig. 2.3, which is denoted by

$$u_2 = \Delta u_2 + u_1 \tag{2.26}$$

where,

$$\Delta u_2 = (V_S^{\,*})\left(1-\frac{\rho_1}{\rho_2}\right) \tag{2.27}$$

Substituting Equations (2.21) and (2.25) in Equation (2.27), one obtains

$$\Delta u_2 = a_1\left(\frac{2((M_S^{\,*})^2-1)}{(\gamma+1)M_S^{\,*}}\right)$$

Hence,

$$u_2 = a_1\left(\frac{2((M_S^{\,*})^2-1)}{(\gamma+1)M_S^{\,*}}\right)+u_1 \tag{2.28}$$

The above relationships are employed to determine the flow properties across a moving normal shock wave inside the shock tube having a base flow of velocity u_1.

Controlling the pressure difference at which the diaphragm ruptures, often expressed in terms of the driver pressure ratio $\frac{p_4}{p_1}$, can control the strength and speed of the normal shock wave. An expression for this ratio can be derived as follows. The pressure and the velocity in Regions 2 and 3 (see Fig. 2.3) are the same, i.e., $p_3 = p_2$ and $u_3 = u_2$. The pressure ratio across the expansion wave (shown in Fig. 2.3) is determined by the *method of characteristics*[28] and is given by

$$\frac{p_3}{p_4} = \left(1 - \frac{\gamma_4 - 1}{2}\left(\frac{u_3}{a_4}\right)\right)^{\frac{2\gamma_4}{\gamma_4 - 1}} \tag{2.29}$$

Re-arranging Equation (2.29) for u_3 and putting $p_3 = p_2$, one obtains

$$u_3 = \frac{2a_4}{\gamma_4 - 1}\left(1 - \left(\frac{p_2}{p_4}\right)^{\frac{\gamma_4 - 1}{2\gamma_4}}\right) \tag{2.30}$$

Since $u_3 = u_2$, Equations (2.28) and (2.30) yield

$$\frac{2a_4}{\gamma_4 - 1}\left(1 - \left(\frac{p_2}{p_4}\right)^{\frac{\gamma_4 - 1}{2\gamma_4}}\right) = a_1\left(\frac{2((M_S{}^*)^2 - 1)}{(\gamma_1 + 1)M_S{}^*}\right) + u_1 \tag{2.31}$$

where,

$$M_S{}^* = \sqrt{\frac{\gamma_1 + 1}{2\gamma_1}\left(\frac{p_2}{p_1}\right) + \frac{\gamma_1 - 1}{2\gamma_1}}$$

Re-arranging Equation (2.31) and substituting for $M_S{}^*$, one obtains

$$\frac{p_4}{p_1} = \frac{p_2}{p_1}\left(1 - \left(\frac{\gamma_4 - 1}{2}\right)\frac{a_1}{a_4}\left(\frac{u_1}{a_1} + \frac{\frac{p_2}{p_1} - 1}{\gamma_1\left(\left(\frac{\gamma_1 - 1}{2\gamma_1}\right)\left(1 + \left(\frac{\gamma_1 + 1}{\gamma_1 - 1}\right)\frac{p_2}{p_1}\right)\right)^{\frac{1}{2}}}\right)\right)^{\frac{-2\gamma_4}{\gamma_4 - 1}} \tag{2.32}$$

Equation (2.32) gives the incident shock strength $\frac{p_2}{p_1}$ as a function of the diaphragm pressure ratio $\frac{p_4}{p_1}$. Although it is difficult to see from inspection of Equation (2.32), an evaluation of this relation shows that, for a given diaphragm pressure ratio $\frac{p_4}{p_1}$, the incident shock strength $\frac{p_2}{p_1}$ will be made stronger as $\frac{a_1}{a_4}$ is made smaller. Moreover, the speed of sound in a light gas is faster than in a heavy gas. Thus, to maximize the incident shock strength for a given $\frac{p_4}{p_1}$, the driver gas should be a low-molecular-weight gas at high temperature (hence high a_4), and the driven gas should be a high-molecular-weight gas at low temperature (hence low a_1). For this reason, many shock tubes in practice use H_2 or He for the driver gas, and the driver gas is heated by electrical means (arc-driven shock tubes) or by chemical combustion (combustion-driven shock tubes).

In general, the flow velocity u can be found by Equation (2.33),[28] i.e.,

$$u = \frac{\dot{m}_{in}}{\rho A}, \tag{2.33}$$

The above discussion and various equations pertain to a situation when a moving normal shock wave is propagating to the right, i.e., towards the nozzle, as depicted in Fig. 2.3. Now, consider that this moving normal shock is incident on the conical surface of the nozzle convergence section, as indicated in Fig. 2.5.

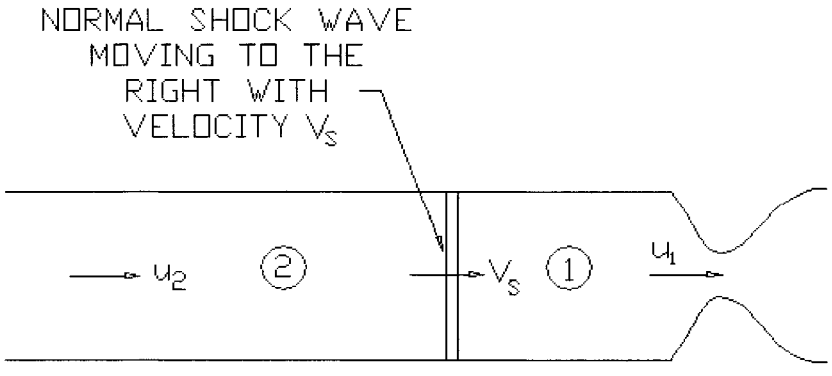

Figure 2.5 Normal shock wave approaching the nozzle convergence section.

At the instant when the incident shock wave impinges on the conical convergence surface, a reflected normal shock wave is created. This reflected normal shock wave travels to the left with velocity V_R, as indicated in Fig. 2.6. The strength of this reflected shock wave is such that the originally induced mass flow with velocity u_2 is decelerated to u_5.

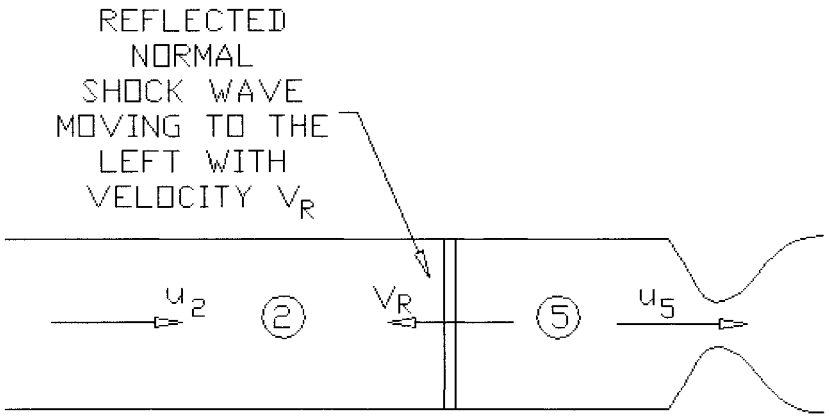

Figure 2.6 Normal shock wave reflected from the nozzle convergence section.

In dealing with unsteady wave motion, it is always convenient to construct wave diagrams. A wave diagram is a plot of the wave motion on a graph of t versus x. A typical wave diagram for a shock tube having a converging-diverging nozzle is shown in Fig. 2.7.[28] At time $t = 0$, the incident shock wave starts from the diaphragm location. Therefore, at $t = 0$, the incident shock wave is at location $x = 0$. At some instant later, say time $t = t_1$, the shock wave is traveling to the right, and is located at point $x = x_1$. This location is labelled as Point 1 in the $x - t$ diagram. It should be noted that the path of the incident shock wave is a straight line in the wave diagram. When the incident shock wave arrives at the conical convergence surface of the nozzle at $x = x_2$, labelled as Point 2 in the $x - t$ diagram, it is reflected towards the left with velocity V_R. At some later instant $t = t_3$, the reflected shock is at location $x = x_3$, labelled as Point 3 in the $x - t$ diagram. The path of the reflected shock wave is also a straight line in the wave diagram.

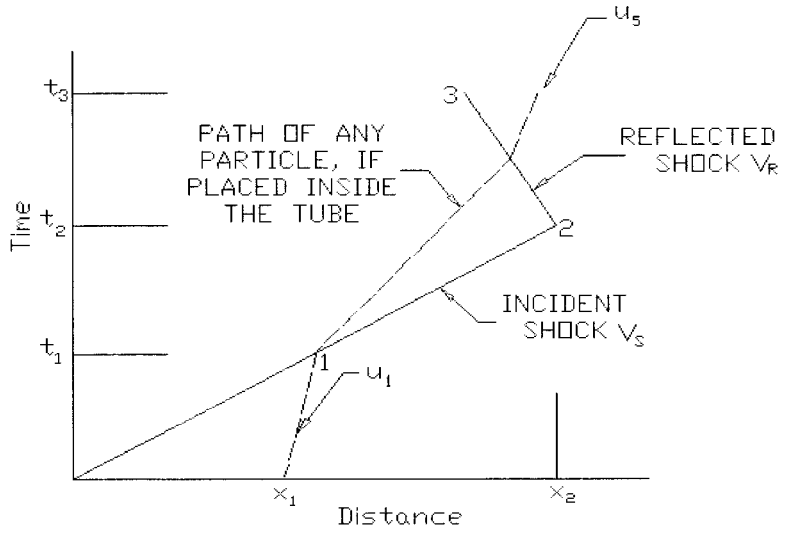

Figure 2.7 Wave diagram of a shock tube having a converging-diverging nozzle.

The slopes of the incident and reflected shock paths are $\frac{1}{V_S}$ and $\frac{1}{V_R}$, respectively. It should be noted that a general characteristic of reflected shocks is that $|V_R| < V_S$. Hence, the reflected shock path is more steeply inclined than the incident shock path.

Returning back to Fig. 2.6, one can write the continuity, momentum and energy equations for a reflected shock wave as

$$\rho_2(u_2 - V_R) = \rho_5(u_5 - V_R) \tag{2.34}$$

$$p_2 + \rho_2(u_2 - V_R)^2 = p_5 + \rho_5(u_5 - V_R)^2 \tag{2.35}$$

$$h_2 + \frac{(u_2 - V_R)^2}{2} = h_5 + \frac{(u_5 - V_R)^2}{2} \tag{2.36}$$

Also, the flow Mach number M_5 behind the reflected shock wave is a function of channel and throat cross-sectional areas, i.e.,

$$M_5 = f\left(\frac{A_5}{A_t}\right) \tag{2.37}$$

Applying the Area Mach number relation between region 5 and the choked nozzle throat yields

$$\frac{A_5}{A_t} = \frac{1}{M_5}\left(\frac{2 + (\gamma - 1)M_5^{\,2}}{\gamma + 1}\right)^{\frac{\gamma+1}{2(\gamma-1)}} \tag{2.38}$$

A similar approach to that taken for the incident shock wave yields the following pressure, density, temperature, and speed of sound ratios across the reflected shock wave:

$$\frac{p_5}{p_2} = \frac{2\gamma (M_R^*)^2 - (\gamma - 1)}{\gamma + 1} \tag{2.39}$$

$$\frac{\rho_5}{\rho_2} = \frac{(\gamma + 1)(M_R^*)^2}{2 + (\gamma - 1)(M_R^*)^2} \tag{2.40}$$

$$\frac{T_5}{T_2} = \frac{((2 + (\gamma - 1)(M_R^*)^2)(2\gamma (M_R^*)^2 - (\gamma - 1))}{(\gamma + 1)^2 (M_R^*)^2} \tag{2.41}$$

$$\frac{a_5}{a_2} = \sqrt{\frac{T_5}{T_2}} \tag{2.42}$$

Re-arranging Equation (2.39), one obtains

$$M_R^* = \sqrt{\frac{\gamma + 1}{2\gamma}\left(\frac{p_5}{p_2}\right) + \frac{\gamma - 1}{2\gamma}} \tag{2.43}$$

where,

$$M_R^* = M_2 - M_R$$

Hence,

$$M_R = M_2 - M_R^* = \frac{u_2}{a_2} - M_R^* = \frac{u_2}{a_2} - \sqrt{\frac{\gamma + 1}{2\gamma}\left(\frac{p_5}{p_2}\right) + \frac{\gamma - 1}{2\gamma}} \tag{2.44}$$

Equation (2.34) can be re-written as

$$u_5 - V_R = (u_2 - V_R)\frac{\rho_2}{\rho_5} \tag{2.45}$$

Dividing Equation (2.45) by a_2, substituting Equation (2.40), and simplifying further, one obtains

$$\frac{u_5}{a_2} = M_R + \frac{2 + (\gamma - 1)(M_R^*)^2}{(\gamma + 1)(M_R^*)} \tag{2.46}$$

The flow Mach number M_5 behind the reflected shock wave front can also be written as

$$M_5 = \frac{\left(\frac{u_5}{a_2}\right)}{\left(\frac{a_5}{a_2}\right)} \tag{2.47}$$

Substituting Equations (2.42) and (2.46) in Equation (2.47), one obtains

$$M_5 = \frac{\left(M_R + \frac{2+(\gamma-1)(M_R^*)^2}{(\gamma+1)(M_R^*)}\right)(\gamma+1)(M_2 - M_R)}{((2+(\gamma-1)(M_R^*)^2)(2\gamma(M_R^*)^2 - (\gamma-1)))^{\frac{1}{2}}} \tag{2.48}$$

Knowing M_2 and M_5, Equation (2.48) can be solved iteratively for M_R^* and the reflected shock front Mach number M_R.

The aforementioned equations provide a brief background about the behaviour of incident and reflected shock waves inside a shock tube having a converging-diverging nozzle at one end. A description of expansion waves has not been provided here, since the purpose of this thesis is to study the reflected shock behaviour before it interacts with the expansion waves. Investigations may be carried out in either section (driver or driven) of the shock tube; however, the most common test section, as in this thesis, is the driven channel. A number of optical methods such as shadowgraphs, Schlieren and Mach-Zehnder interferometry, can be used for obtaining flow measurements inside shock tubes.[27,28] These methods can be expensive, and sometimes difficult to adjust for operation. Other methods employing high frequency data sampling techniques[32] are commonly used, as in this thesis, for pressure measurements. For measuring the flow temperature inside a shock tube (in any section), thermocouples can be installed.[26] Once the pressure and temperature measurements have been taken, it is straightforward to determine various flow parameters inside the shock tube with the help of various incident and reflected shock wave relations. In addition to the above experimental methods, shock tube results can also be predicted through numerical simulations, enabling a more comprehensive understanding of the flow phenomena involved.

2.2 Cold-Flow Rocket Experiment

Section 2.1 provided a brief description of the shock tube used for experimentation in the present study and the various equations related to moving normal incident and reflected shock waves. The experimental apparatus incorporates the application of a steady-state flow in the driven section in simulating the flow within a

rocket motor. Various design considerations together with calculated design parameters for the apparatus, are presented in the following sections.

2.2.1 Design Considerations

It was noted in the planning and designing of the apparatus, that one requires a constant mass air flow at constant pressure through the driven (i.e. primary) channel of the shock tube, under a choked nozzle condition. The air supply is made available through either the university's main air distribution line or by a two-stage compressor installed along with an air reservoir in the laboratory (Room E-33 at Ryerson University).

The shock tube apparatus can be conveniently attached to the existing air reservoir via an isolation ball valve. Also, the apparatus is easily connected to the main distribution line. The reservoir can also be used as an alternative air source in the event that the distribution line is unable to deliver the desired pressure and if there is any difficulty in branching the distribution line to the apparatus location. Furthermore, the reservoir provides a means of passing high-pressure air through the channel by opening the isolation valve to ensure the absence of debris prior to an experimental firing.

The available air supply from the distribution line cannot provide a steady pressure, thus a pressure regulator with an appropriate adjustment range of pressure is used to regulate the pressure in providing a controlled supply to the driven (primary) channel. A major concern of the design is to devise a method of pressurizing the driver (secondary) section in such a way so as to prevent an excess or uncontrolled differential pressure across the diaphragm. The differential pressure control is necessary to prevent any kind of premature rupture of the diaphragm, which separates the two sections. This issue can be resolved by branching the reservoir air supply (connected to the air compressor) to the driver chamber. A boost-pressure valve along with a flow restrictor can control volume and pressure of air supply into the driver chamber. The boost-pressure valve is a push-button-type spool valve that enables fine pressure control in the secondary chamber. This type of control is desired to produce a precise differential pressure, which governs the shock strength upon rupturing of the diaphragm.

When the desired pressure is reached in the primary channel, simultaneously the secondary section is pressurized by the boost-pressure valve so as to avoid premature rupture of the diaphragm. Hence, when the pressures in the primary and the secondary sections are equal, one starts pressurizing the driver to achieve the desired differential pressure across the diaphragm. After rupturing of the diaphragm, the next hurdle is to take transient pressure measurements at a specified location upstream of the nozzle. Employing a high frequency data sampling system, connected to a pressure transducer of appropriate operating range near the nozzle, solves this problem. Fig. 2.8 depicts a schematic diagram of the experimental apparatus. A complete apparatus assembly, with all the necessary dimensional details, is presented at the end of this chapter.

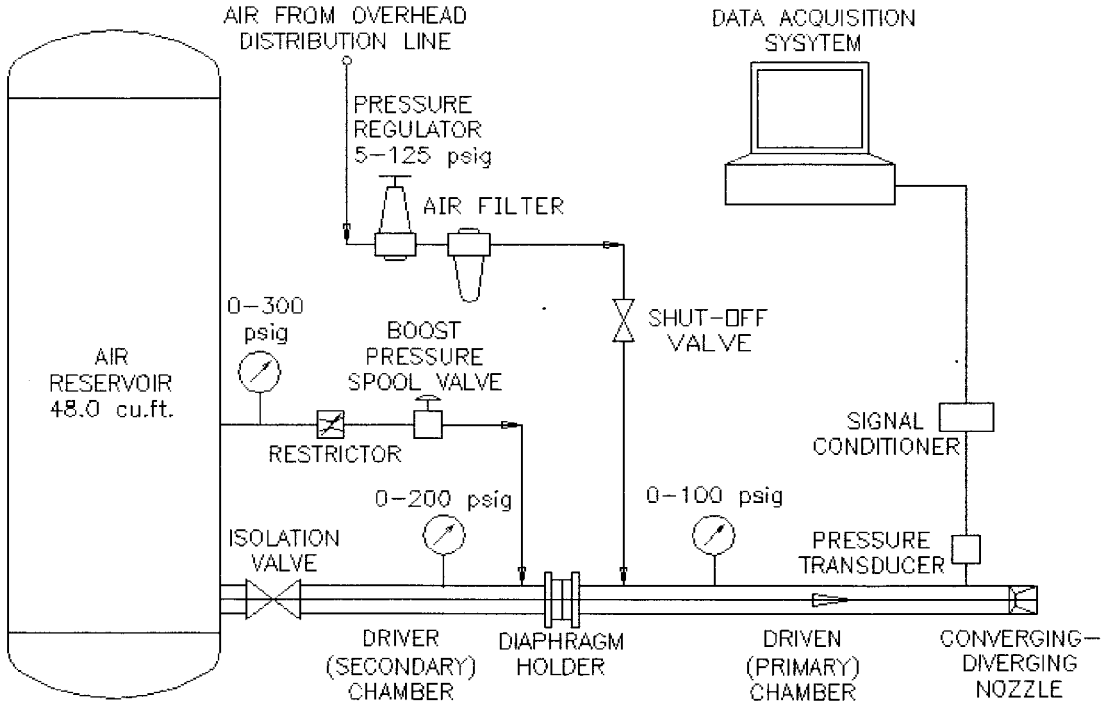

Figure 2.8 Schematic diagram of experimental apparatus.

2.2.2 Operating Pressure and Mass Flow Rate

Once the working components of the apparatus are established, one can proceed further to determine a general starting pressure level for the apparatus. One should be very careful in determining the starting pressure in order to achieve a choked flow through the nozzle; pressure available in the distribution line, size of the nozzle, and

diameter of the channels are important factors to be considered. Also, the structural limits and safe operation of the apparatus should be kept in mind.

For a choked nozzle flow, the Mach number at the nozzle throat is equal to 1, i.e., $M_t = 1$, and the flow stagnation pressure p_1 relative to the ambient outside air pressure p_{atm} is given by

$$\frac{p_1}{p_{atm}} > \left(\frac{\gamma_1 + 1}{2}\right)^{\frac{\gamma_1}{\gamma_1 - 1}} \tag{2.49}$$

Equation (2.49)[28] provides a criterion that serves as a lower limit pressure for our experimental firings.

For air,

$$\gamma_1 = 1.4,$$

$$p_{atm} = 101.325 \text{ kPa (1 atm)}$$

Therefore,
$$\frac{p_1}{101.325} > \left(\frac{1.4 + 1}{2}\right)^{\frac{1.4}{1.4 - 1}}$$

or,
$$p_1 \geq 191.8 \text{ kPa } (\approx 1.89 \text{ atm})$$

Hence, the pressure in the driven (primary) section of the shock tube should be greater than about 191.8 kPa (≈ 1.89 atm) so as to achieve a choked flow through the nozzle. It is worth noting here that we cannot achieve SRM operational pressure levels, due to structural limitations of the apparatus and unavailability of air at higher pressures. Also, the safe operation of the current pressure transducer limits the allowable operating pressure. A driven pressure of 374.9 kPa (≈ 3.7 atm) is a typical level in this cold-flow study, with consideration for incident and reflected shock overpressures above this baseline.

The volumetric flow rate of primary air supply is 0.0096 m^3/s, and the mass flow rate is given by

$$\dot{m}_{in} = Q\rho_1$$

where,

$$\rho_1 = \frac{p_1}{RT_1} = \frac{374902.5}{287 * 294} = 4.44 \text{ kg/m}^3$$

Hence, $\dot{m}_{in} = 0.0096 * 4.44 = 0.043$ kg/s

Also, $a_1 = \sqrt{\gamma R T_1} = 343.7$ m/s

and $\dot{m}_{in} = \rho_1 A_1 u_1$

where,

$$A_1 = \frac{\pi}{4} d_1^{\,2} = \frac{\pi}{4}(0.0508)^2 = 0.002026 \text{ m}^2$$

Hence, $u_1 = 4.777$ m/s

and $M_1 = \frac{u_1}{a_1} = 0.0139$

2.2.3 Channel Size

Sizing of the shock tube involves the selection of diameter and length of driven and driver sections. Primarily, size is governed by the available space in the aerodynamics laboratory (Room E-33 at Ryerson University). Good practice in design suggested that the apparatus should be located close to the available air source. The compressor and the reservoir are installed in the northeast corner of the laboratory, and an overhead air distribution line runs through this location as well. Hence, it was decided that the construction of the apparatus should be done near this location in the available empty space.

A 2-inch-diameter pipe of sufficient length and quality was available in the machine shop. So, it was decided to employ this pipe for the construction of the apparatus. For determining the length of the channel, one can make use of a wave ($x-t$) diagram to estimate the test time that elapses from initial shock reflection to later interaction with downstream-moving rarefaction and compression waves, and the downstream-moving contact surface.

To elucidate this estimation process, consider an incident shock pressure ratio of $\frac{p_2}{p_1} = 1.5$, a high value keeping structural limits like thickness of the pipe in mind. Putting $\gamma = 1.4$ for air and $\frac{p_2}{p_1} = 1.5$ in Equation (2.19), one obtains

$$M_S^* = 1.195$$

Putting $\gamma = 1.4$, $T_1 = 294\,\text{K}$, and M_S^*=1.195 in Equation (2.15) gives the temperature ratio across the incident moving shock as

$$T_2 = 330\ \text{K}$$

Since, $a_2 = \sqrt{\gamma R T_2}$, one obtains

$$a_2 = 364.13\ \text{m/s}$$

Hence, the velocity of the incident shock will be, for a_1=343.7 m/s,

$$V_S^* = (M_S^*)a_1 = 410.798\ \text{m/s}$$

From Equation (2.16), and using $M = \frac{u}{a}$,

$$V_S = V_S^* + u_1$$

Hence, $$V_S = 410.798 + 4.777 = 415.575\ \text{m/s}$$

From Equation (2.28), one can easily calculate the speed of the contact surface as

$$V_{cs} = u_2 = 107.365\ \text{m/s}$$

In order to calculate the reflected shock Mach number M_R from Equation (2.48), first one should determine M_2 and M_5.

$$M_2 = \frac{u_2}{a_2} = \frac{107.365}{364.13} = 0.294$$

and from Equation (2.38) with $A_5 = 0.002026\ \text{m}^2$ (as $d_5 = 0.0508\ \text{m}$) and $A_t = 0.0000486\ \text{m}^2$ (as $d_t = 0.007870\ \text{m}$), one obtains

$$M_5 = 0.0139$$

Putting M_2 and M_5 in Equation (2.48) gives

$$M_R = -0.761,$$

so that $$V_R = (M_R)a_2 = -277.10 \text{ m/s}$$

Putting M_2 and M_R in Equation (2.42) gives

$$\frac{a_5}{a_2} = 1.0179,$$

so that $$a_5 = a_2(1.0179) = 370.65 \text{ m/s}$$

Hence, $$u_5 = a_5 M_5 = 370.65 * 0.0139 = 5.15 \text{ m/s}$$

Let l be the length of the driven (primary) channel. Due to space limitations,

$$l = 2.3 \text{ m}$$

Now, one can check whether the selected length of the driven channel is sufficiently long such that there is adequate time to study the reflected shock before it encounters the contact surface, moving downstream towards the nozzle (assuming this interaction occurs before the principal rarefaction wave arrives). This can be easily accomplished with the help of a wave diagram, as shown in Fig. 2.7. One just has to calculate the time between the reflection of the incident shock and its collision with the contact surface. If this test time is long enough, the channel length is adequate.

The wave diagram of Fig. 2.7 is reproduced here, with the wave and contact surface speeds indicated, as Fig. 2.9. In this Figure, one notes

$$x_2 - x_1 = l \tag{2.50}$$

Also, t_2 is the time when incident normal shock arrives at the nozzle convergence region, c is the point which represents the collision of the reflected shock and the contact surface, and the co-ordinates of point c are given by (x_c, t_c). In other words, x_c is the distance from the diaphragm at which the contact surface collides with the reflected shock, and t_c denotes the corresponding time. Hence, the test time, which determines the time taken by the reflected shock to move upstream and collide with the contact surface, is given by

$$t_{test} = t_c - t_2 \tag{2.51}$$

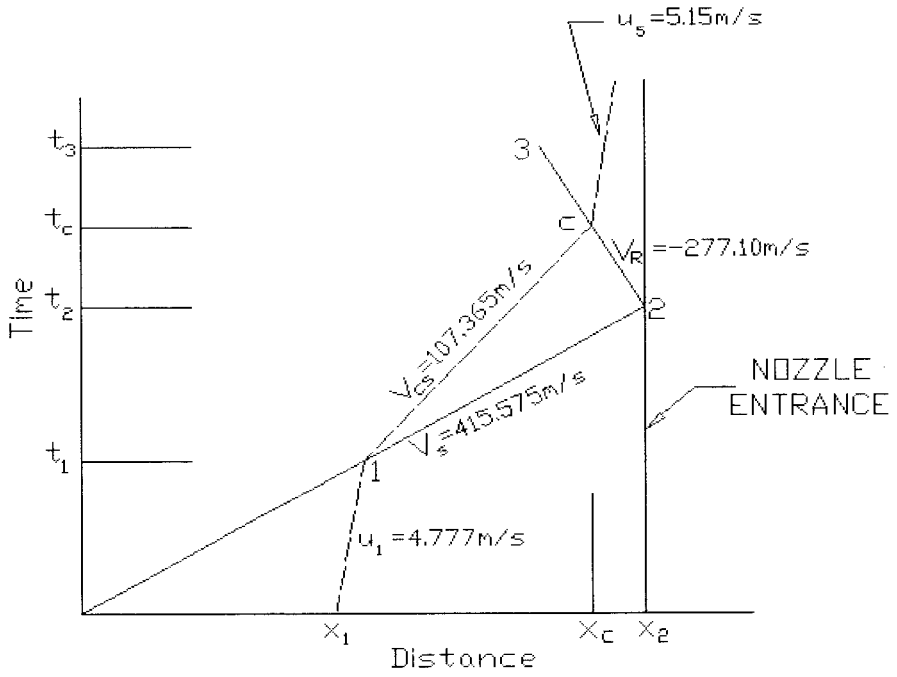

Figure 2.9 Wave diagram for checking the length of the driven chamber.

From the above diagram, it is observed that

$$t_2 = \frac{x_2 - x_1}{V_S} \tag{2.52}$$

Putting $x_2 - x_1 = l = 2.3$ m and $V_S = 415.575$ m/s, in Equation (2.52), one obtains

$$t_2 = \frac{2.3}{415.575} = 5.534 \text{ ms}$$

Hence, it takes 5.534 ms for the incident shock to reach the nozzle entrance. The distance travelled by the contact surface up to point c is given by

$$x_c = V_{cs}(t_2 + t_{test}) \tag{2.53}$$

Also, the distance travelled by the reflected shock wave up to point c is given by

$$x_c = V_S t_2 + V_R t_{test} \tag{2.54}$$

Since, at point c the contact surface and the reflected shock collide with each other, one can therefore equate Equations (2.53) and (2.54) to calculate the test time as

$$t_{test} = \frac{(V_S - V_{cs})t_2}{V_{cs} - V_R} \tag{2.55}$$

Putting $V_S = 415.575$ m/s, $V_{cs} = 107.365$ m/s, $V_R = -277.10$ m/s, $t_2 = 5.534$ ms in Equation (2.55), one obtains

$$t_{test} = 0.004436 \text{ s} = 4.436 \text{ ms}$$

Since, one knows t_{test} and t_2, one can calculate t_c as

$$t_c = t_{test} + t_2 = 4.436 + 5.534 = 9.970 \text{ ms}$$

From Fig. 2.9, it is clear that

$$t_c = \frac{x_c}{V_{cs}} \tag{2.56}$$

Hence, $$x_c = t_c V_{cs} = 0.009970 * 107.365 = 1.070 \text{ m}$$

In other words, the collision between the reflected shock wave and the contact surface occurs at a distance of 1.070 m from the diaphragm station at 9.970 ms. Therefore, we have at least 4.436 ms to measure the transient pressure of the flow in the vicinity near the nozzle entrance. (There is a further time until any wave resulting from this interaction reaches the transducer location.) Since this is a reasonable length of time, one can conclude that a pressure ratio of $\frac{p_2}{p_1} = 1.5$ and a driven chamber length of $l = 2.3$ m fall within the scope of this study.

Similarly, one can find an approximate value of pressure in the driver section from Equation (2.32). Putting $\frac{p_2}{p_1} = 1.5$, $\gamma_4 = 1.4$, $\frac{a_1}{a_4} = 1$ (as the gases in both the sections are at the same temperature), $u_1 = 4.777$ m/s, and $u_4 = 0$ (because gas in the region 4 is at rest) in Equation (2.32), one obtains

$$\frac{p_4}{p_1} = 2.30$$

Hence, $$p_4 = (p_1)2.30 = 374902.5 * 2.30 = 862.275 \text{ kPa}$$

In other words, the pressure in the driver chamber would be about 8.5 atm. One can now calculate the speed of the expansion wave front, which travels upstream of the diaphragm station. The temperature of the gas in this region will be $T_4 = 294$ K, so that

$$a_4 = \sqrt{1.4 * 287 * 294} = 343.699 \text{ m/s},$$

i.e., the expansion wave front in the driver chamber moves with a velocity of 343.699 m/s. The length of the driver chamber is 1.73 m. Therefore, the time taken by the expansion wave front to reach the reservoir end will be given by

$$t_{ex} = \frac{1.73}{343.699} = 0.005033 \text{ s} = 5.033 \text{ ms}$$

Thus, after 5.033 ms, the expansion waves will get reflected from the left end wall and will start moving downstream towards the diaphragm station. This elapsed time, followed by that required for interaction with the upstream-moving reflected shock wave, signifies that this driver length is adequate.

In summary, the nominal reference values for the experimental apparatus are:

1. Length of driven chamber = 2.3 m = 90.55 in
2. Length of driver chamber = 1.73 m = 68.11 in
3. Diameter of pipe = 0.0508 m = 2 in
4. Pressure ratio, $\frac{p_2}{p_1} = 1.5$
5. Driven chamber pressure = 374.902 kPa $\approx$ 3.7 atm
6. Driver chamber pressure = 862.275 kPa $\approx$ 8.5 atm
7. Diaphragm pressure ratio, $\frac{p_4}{p_1} = 2.30$

The above pressure values result from one-dimensional, ideal flow theory. Exact values resulting from experimental firings may differ due to system losses, etc.

2.2.4 Nozzle Selection

Generally, rocket motors employ a converging-diverging nozzle for generating thrust. Hence, such a nozzle is an obvious choice for this study. Based on the required flow conditions, one can determine the various parameters for the nozzle through simple nozzle flow theory. The nozzle should be designed in such a way that it can be easily replaced and allow for other nozzle shapes to be accommodated in the apparatus.

The nozzle's throat diameter d_t is related to the flow Mach number upstream of the nozzle via Equation (2.23). Note that the channel cross-sectional area is:

$$A_1 = \frac{\pi}{4} d_1^{\,2} = \frac{\pi}{4}(0.0508)^2 = 0.002026 \text{ m}^2$$

Putting $M_t = 1$ (for a choked nozzle), $M_1 = 0.0139$, and $\gamma = 1.4$ for air in Equation (2.23), one obtains, for the reference nozzle used in the present study,

$$\frac{A_1}{A_t} = 41.63,$$

so that $$A_t = \frac{A_1}{41.63} = 0.000048657 \text{ m}^2$$

and $$d_t = 0.007870 \text{ m}$$

The pressure at throat is calculated by applying the isentropic relation between region 1 and the choked nozzle throat given by[31]

$$\frac{p_t}{p_1} = \left(\frac{2 + (\gamma - 1) M_1^{\,2}}{2 + (\gamma - 1) M_t^{\,2}} \right)^{\frac{\gamma}{\gamma - 1}} \tag{2.57}$$

Putting $p_1 = 374.902$ kPa (which is the design pressure point for the driven chamber), $M_1 = 0.0139$, and $M_t = 1$, in Equation (2.57), one obtains

$$p_t = 198.060 \text{ kPa}$$

Similarly, applying the isentropic relation for temperature between region 1 and the choked nozzle throat yields

$$\frac{T_t}{T_1} = \left(\frac{p_t}{p_1} \right)^{\frac{\gamma - 1}{\gamma}} \tag{2.58}$$

so that, with $T_1 = 294$ K, $$T_t = 245 \text{ K}$$

Hence, $$a_t = \sqrt{\gamma R T_t} = 313.756 \text{ m/s}$$

and $$u_t = M_t a_t = 313.756 \text{ m/s}$$

Similarly, one can determine the pressure, temperature, gas velocity, and Mach number at the exit of the nozzle, assuming ideal isentropic expansion and an area expansion ratio of $\frac{A_e}{A_t} = \frac{d_e^{\,2}}{d_t^{\,2}} = 6.66$:

$$p_e = 5.0572 \text{ kPa}$$

$$T_e = 85.91 \text{ K}$$

$$u_e = 646.58 \text{ m/s}$$

$$M_e = 3.48$$

Note that, since the pressure at the exit of the diverging section ($p_e = 5.0572$ kPa) is less than the atmospheric pressure, the nozzle is in fact over-expanded.

The convergence and divergence half-cone angles of the reference nozzle are 45° and 15°, respectively. A glass-phenolic nozzle is selected as the reference design, with characteristics as summarized below:

1. Nozzle type: converging-diverging, supersonic, over-expanded, choked.
2. Nozzle material: glass-phenolic.
3. Inlet diameter of nozzle = 0.0508 m = 2 in
4. Throat diameter = 0.007870 m = 0.31 in
5. Exit diameter = 0.0203 m = 0.8 in
6. Length of convergence section = 0.0215 m= 0.85 in
7. Length of throat = 0.001 m = 0.04 in
8. Length of diverging section = 0.02368 m = 0.93 in
9. Overall length of nozzle = 0.04618 m = 1.82 in

The above nozzle dimensions are noted below in Fig.2.10.

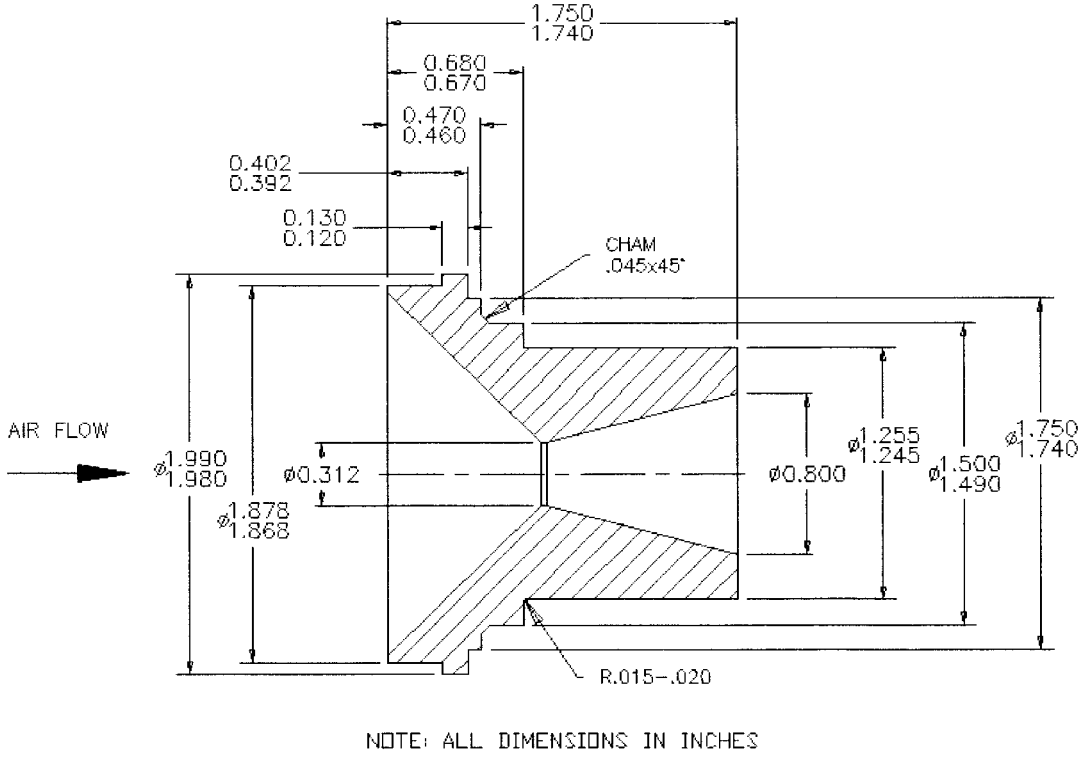

Figure 2.10 Nozzle details.

2.2.4.1 Nozzle Housing

The nozzle housing is designed in such a way that it can be removed along with the nozzle in order to be stored when not in use. Hence, quick assembly and disassembly of the nozzle housing is of prime concern. The housing uses a standard 2-inch National Pipe Thread (NPT) union, whose purpose is to couple the nozzle with the driven chamber of the apparatus so that they appear to be one part. This housing is easy to view in the diagram given below. Fig. 2.11 shows a detailed dimensional drawing of the nozzle housing. For a better understanding, the front view and the side view of the nozzle assembly are shown below in Fig. 2.12. Silicone rubber is used during the nozzle assembly to secure the nozzle from any kind of shifting during the operation of the apparatus.

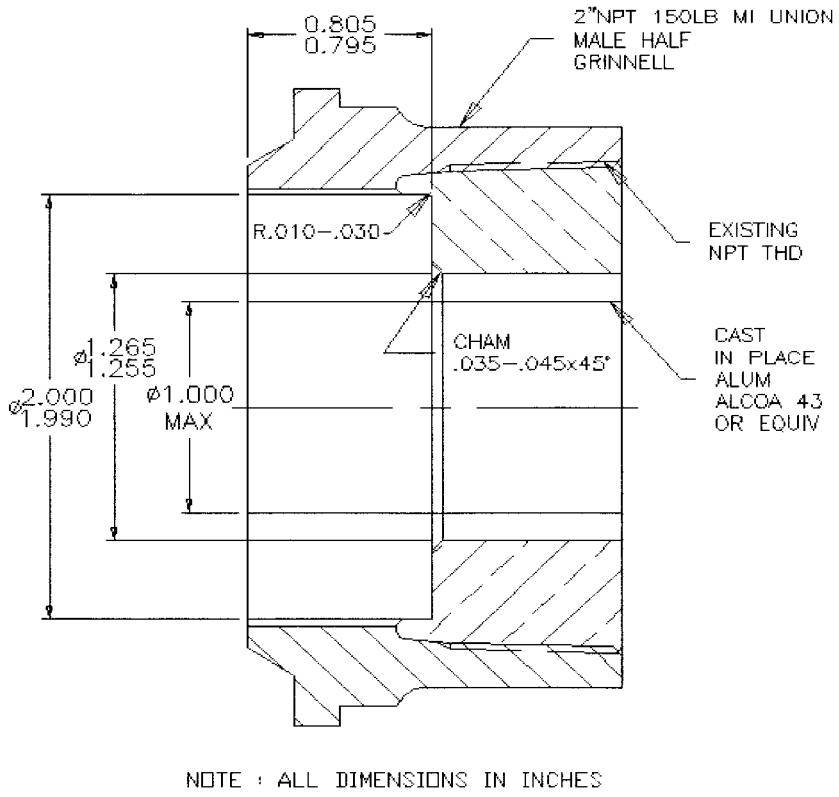

Figure 2.11 Nozzle housing.

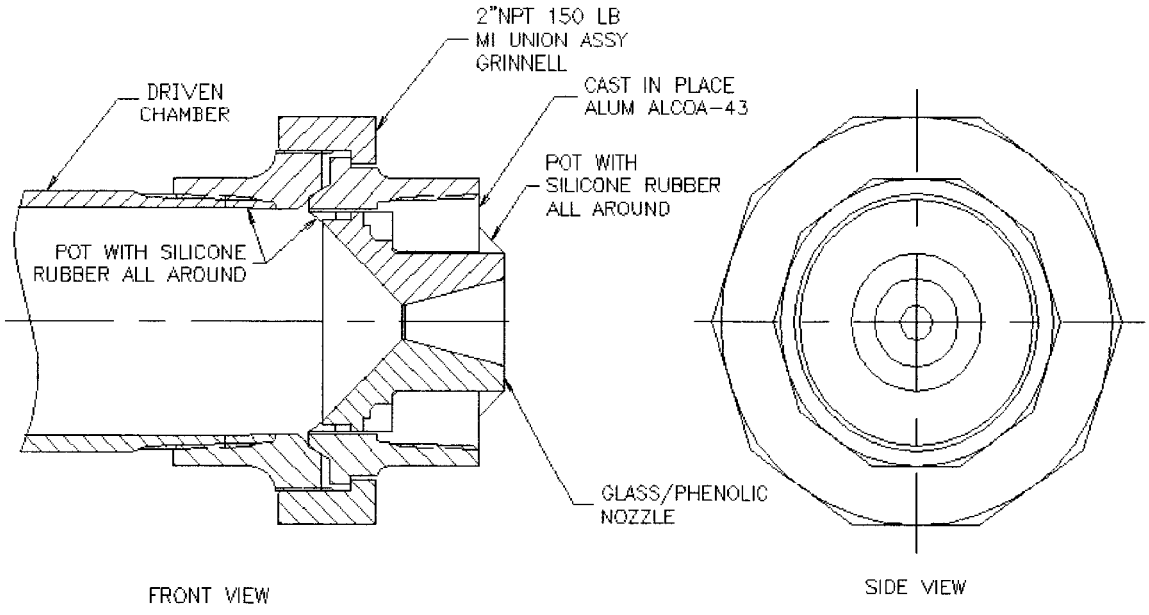

Figure 2.12 Nozzle assembly.

2.2.5 Orifice Plate

An orifice plate is a thin or thick plate having an orifice (i.e., a small opening) of any cross-section (such as circular, triangular, rectangular, and square). A simple orifice plate having a circular, sharp-edged orifice at a 45° divergence (from the horizontal reference) is shown in Fig. 2.13.

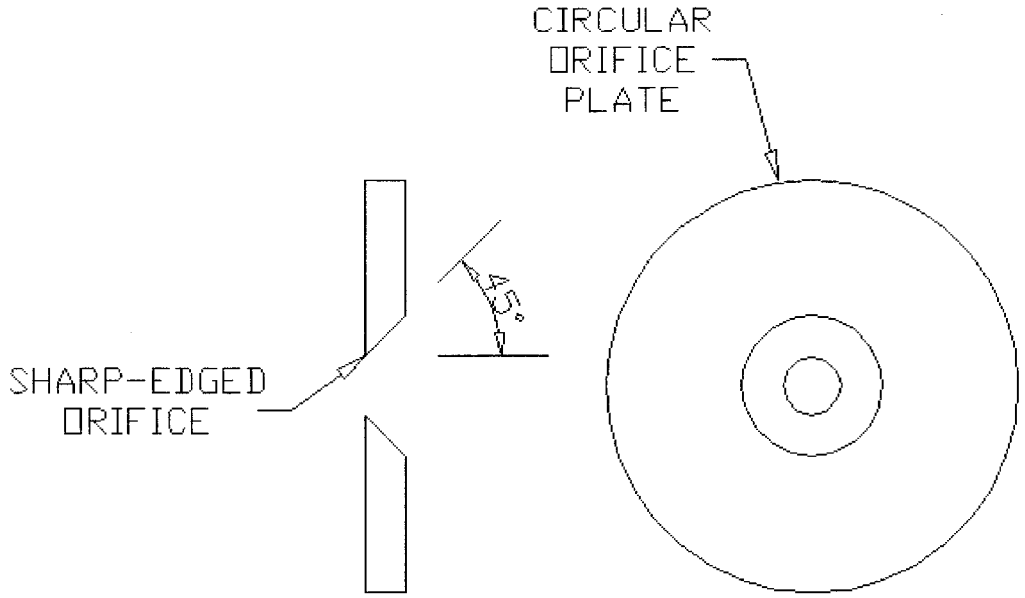

Figure 2.13 Orifice plate.

An orifice plate having 0° and 45° divergence inclinations with the horizontal reference was chosen as a limiting case of the converging-diverging nozzle (with 90° converging surface) for the present study. However, due to time constraints, only the 0° orifice plate was employed for experimentation, but numerical simulations for both divergence inclinations were generated. The exact dimensions of the orifice plate used for experimental firings are shown in Fig. 2.14. The diameter of the orifice is kept the same as the converging-diverging nozzle throat diameter.

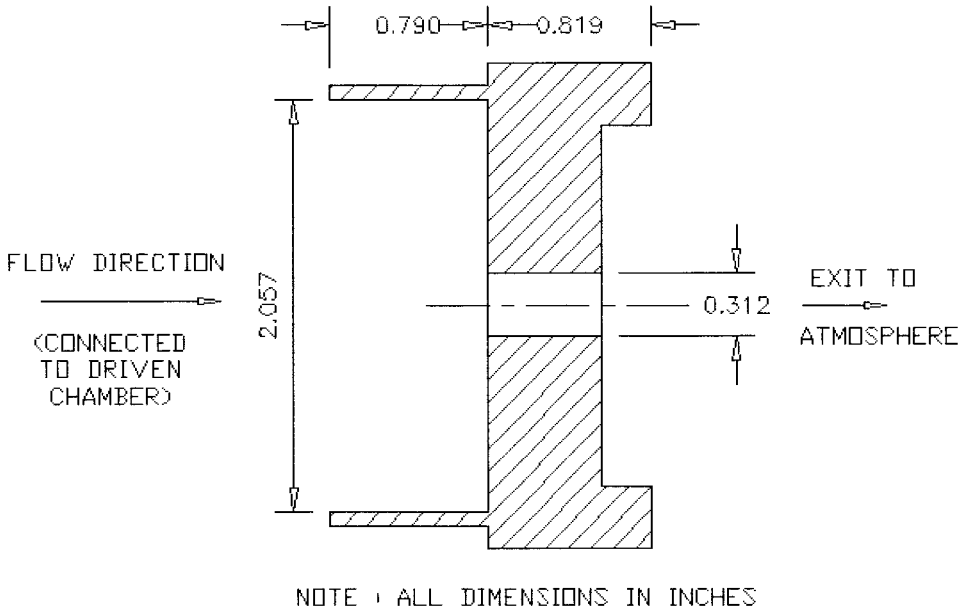

Figure 2.14 Dimensions of orifice plate employed for experimental firings.

2.2.6 Selecting a Diaphragm

As stated in Section 2.1, the diaphragm separates the high-pressure (driver) chamber from the low-pressure (driven) channel, and the diaphragm pressure ratio, $\frac{p_4}{p_1}$, in turn determines the shock strength, $\frac{p_2}{p_1}$. Therefore, selection of the diaphragm material requires appreciable consideration, depending upon the desired shock strength. It was assumed in Section 2.2.3 that a nominal shock strength of 1.5 would be sufficient to conduct our study. Hence, the selected diaphragm should burst at a specific pressure differential so that the desired shock strength is achieved.

Keeping in mind the required diaphragm pressure ratio, it was decided that a polyester film having a thickness of 0.0035 inches would serve the purpose. The film is cut into a circular shape with scissors and is ready to use. However, while performing actual experimental firings, if it is found that there is premature rupturing of the diaphragm and the desired shock strength is not achieved, then other diaphragm material

and thicknesses might be considered. The diaphragm is placed in the diaphragm holder. This holder is placed between the two channel sections and then is tightened with the help of nuts and bolts as shown in Fig. 2.15. In the present study, slowly increasing the pressure in the driver chamber to a certain level ruptures the diaphragm (rather than employing the heated fuse wire technique discussed below).

In order to achieve higher shock strengths, thicker diaphragm materials, such as steel, aluminium, or tin, in single or double mode of operation[26] can be easily facilitated in the diaphragm holder. Usually, thicker materials are more difficult to rupture by increasing the pressure in the driver chamber. Hence, to fulfill this requirement, one can make use of a low resistance fuse wire like nichrome to melt the diaphragm. A direct current (DC) voltage is supplied to the fuse wire, which is in contact with the diaphragm surface. The voltage induces a current, thus heating of the wire takes place at a controlled rate. The localized wire temperature attained is high enough to locally melt the diaphragm, thus producing a rupture of the diaphragm material. The above rupturing mechanism is cost-effective, and desired results are easily obtained. The diaphragm holder along with the fuse wire assembly is shown in Fig. 2.15.

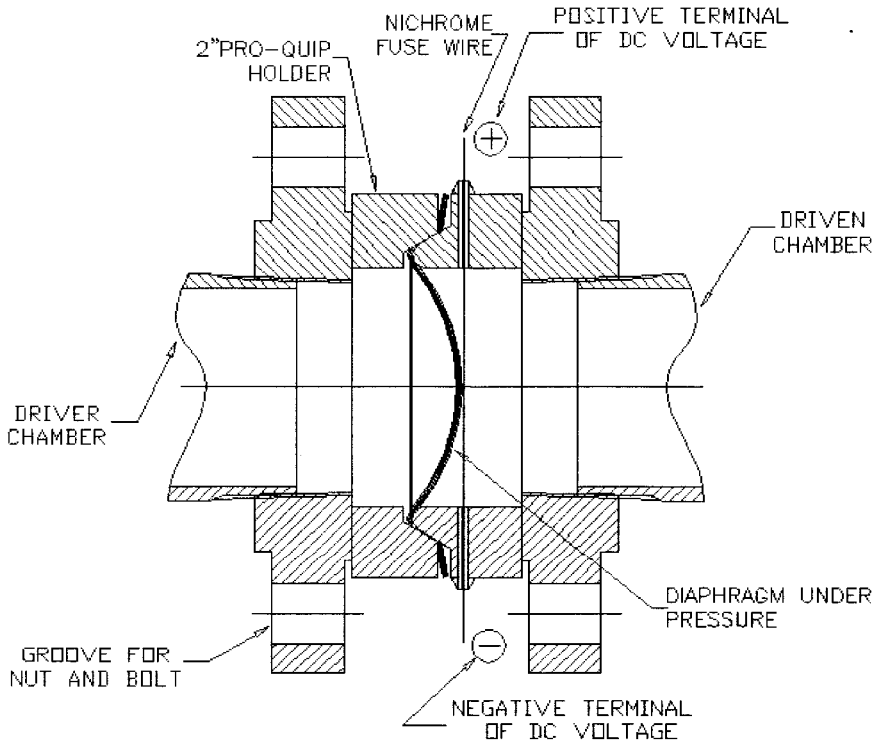

Figure 2.15 Diaphragm holder and fuse wire assembly.

2.2.7 Compressor

The compressor in the aerodynamics laboratory is a two-stage compressor. It is situated in the northeast corner of the laboratory. The compressor is equipped with a receiver tank, which is connected to the driver chamber of the shock tube through an isolation ball valve as shown in Fig. 2.8. In the absence of air supply from the main distribution line, the compressor's capacity is ample enough to sustain steady airflow at the reference channel pressure of 375 kPa (about 3.7 atm), without significant variations in the pressure. The maximum pressure that can be attained in the reservoir tank is 1275 kPa (about 12.6 atm). However, if the pressure in the tank exceeds the maximum value, the compressor is shut down automatically through a pre-installed safety mechanism.

2.2.8 Primary Air Supply

In this section, the method of injecting air into the driven (primary) channel is described. It is desired that the flow field in the shock tube should be uniform for as great a distance as possible. In other words, an established flow is desired in as short a distance as possible. This is necessary to dampen the disturbances occurring at the injection port, so that their effects on the travelling shock wave as it moves further downstream will be minimized. Hence, the inlet port is at a distance of 0.12 m from the diaphragm station, based on practical considerations.

In order to devise a method of tapping air into the chamber, the apparatus utilizes a standard 2-inch coupling manufactured by Victaulic Company. The coupling consists of an annulus chamber, which acts as a plenum (an enclosure in which air or other gas is at a pressure greater than that of the outside atmosphere). This chamber diffuses the incoming airflow and forces the air through a circumferential slit of 0.15 cm width. A groove is made on the primary chamber tube, which provides a seat for the standard coupling as shown in Fig. 2.16. Some flow losses might occur across the slit. Silicone rubber is used as a sealant to seal the area around the coupling-pipe interface, as shown in Fig. 2.17, to prevent any air leakage.

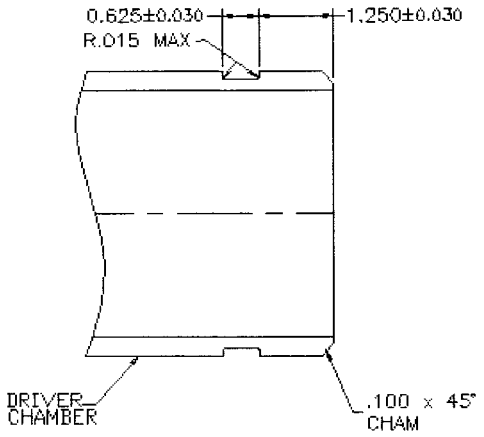

Figure 2.16 Groove details.

The groove details of the driver chamber are only shown in Fig. 2.16. A similar kind of groove is made on the driven channel.

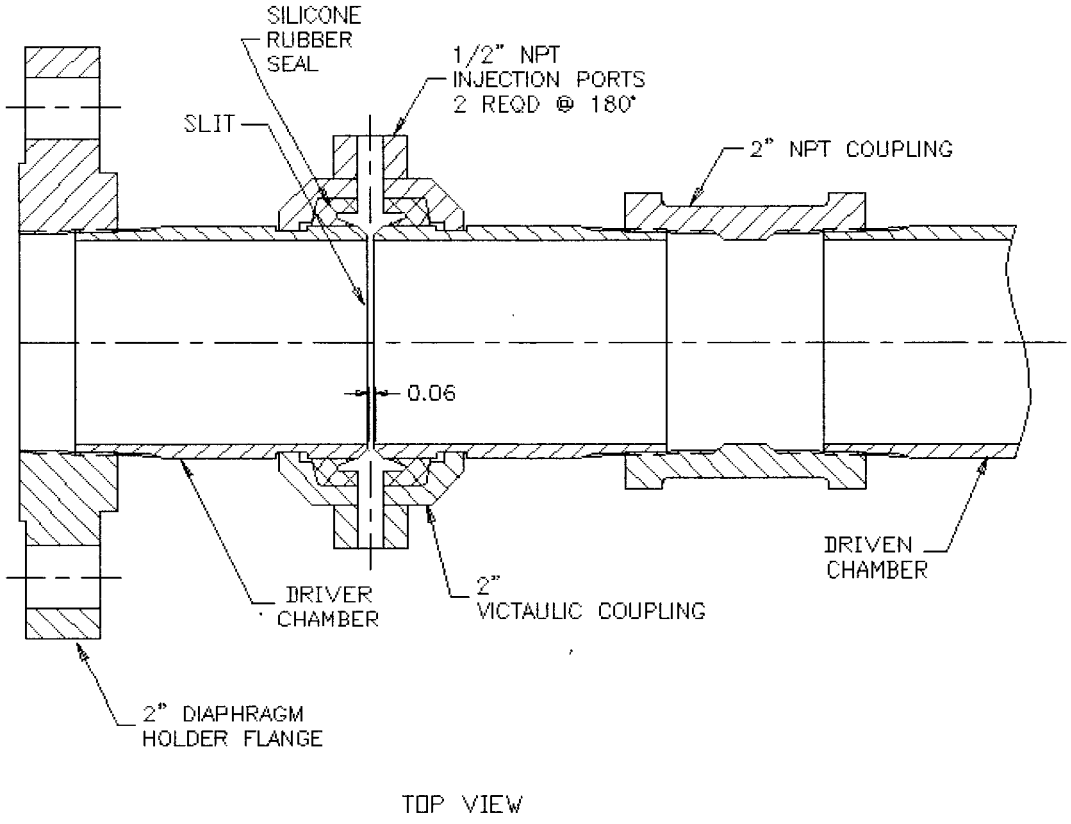

Figure 2.17 Primary air inlet assembly.

2.2.9 Measurements

Various measuring instruments, i.e., pressure gauges, pressure transducer, and thermocouples, can be attached at fixed positions in the wall of the shock tube. Required measurements can be easily taken at a desired time from when the firing is initialized. The high speed and the short duration of the flow necessitate that the measuring systems recording the pressure and the temperature should have a high frequency response.

It should be noted that the tapings in the shock tube wall allow measurements to be taken in the immediate vicinity of the measuring probe.

The range of the pressure gauges used in the apparatus is from 0 to 2200 kPa. Typical pressure and temperature taps used in the apparatus are shown in Fig. 2.18.

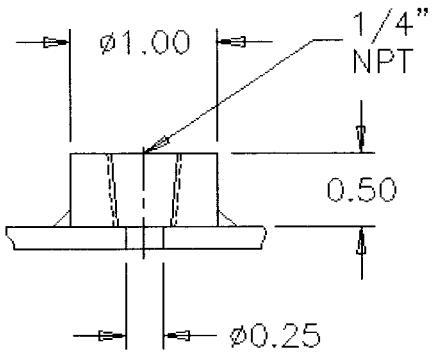

Figure 2.18 Pressure and temperature tap.

2.2.10 Selecting a Transducer

Generally, strain gauges are a common choice for static pressure measurements. However, these gauges lack the frequency response necessary for the measurement of the high speed and short duration characteristics of a shock wave. A better-suited sensor for shock tube dynamic pressure measurements is a piezoelectric transducer. The natural frequency of such transducers depends on the particular crystal unit. In general, these transducers operate on the principle of change in the capacitance between two conducting

plates generating charge in a piezoelectric crystal. The signal can then be conditioned and captured by an imaging oscilloscope or by a computer-based system.

In the present study, a high frequency, piezoelectric pressure transducer (manufactured by PCB PIEZOTRONICS Inc.) is used to measure the transient pressure in the shock tube. The transducer is a probe type, general-purpose quartz pressure sensor, made of stainless steel and hermetically sealed. It produces a high quality signal, which is independent of the cable length used for transmission of the signal. Specifications for the pressure transducer are listed below:[33]

1. Model number: 112A02
2. Serial number: 17993
3. Sensing element: quartz
4. Sensitivity: 0.000145 pC/Pa ($\pm$ 15%)
5. Resolution: 13.78 Pa
6. Measurement range: 689.5 kPa
7. Maximum pressure (static): 6895 kPa
8. Resonant frequency: up to 500 kHz
9. Rise time: $\leq$ 2 μs
10. Temperature range: -478 K to 478 K
11. Flash temperature: 1900 K
12. Capacitance: 18 pF
13. Insulation resistance at 294 K: $\geq 10^{12}$

In the present study, the transducer is mounted at 2.2 m from the diaphragm station, i.e., 10 cm upstream of the nozzle. Therefore, the transducer is quite close to the nozzle entrance region as required, and as soon as the incident shock arrives, the transient pressure is recorded in the present study. The transducer is screwed in a pressure transducer tap, which is different from the normal pressure taps. Such a tap is shown in Fig. 2.19.

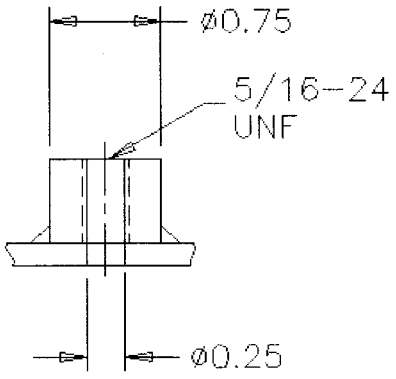

Figure 2.19 Pressure transducer tap.

2.2.11 Data Acquisition

This section provides a description of components and method of recording pressure readings. The instrumentation for measuring the transient pressure in the shock tube was available in the Propulsion Research Facility (PRF at Room E-128B at Ryerson University).

The pressure transducer is connected to a charge amplifier (converter) by means of a coaxial cable.[33] This amplifier converts sensor signals from the pressure transducer to voltage signals for transmission over long cables, and provides an interface to the data acquisition system. It is low in noise, powered by sensor signal conditioners, and installed in-line between the pressure sensor and signal conditioner. This charge amplifier is coupled to a sensor signal conditioner by means of another coaxial cable, which is connected to the data acquisition system. The sensor signal conditioner is a single channel system, with unity gain, and battery-powered.[33] It offers a portable, convenient method for powering sensors and conditioning their output signals for transmittal to readout and recording instruments, as in our case.

The data acquisition system offers high resolution and high-speed signal capturing capabilities. This system enables the capture of analog and continuous signals measured by the sensor and modified by the signal conditioner, and it feeds a digital signal to a computer. In the present study, WaveBook, manufactured by IOtech Inc., is used as a

high-speed data acquisition system. WaveBook has a 16-bit analog-to-digital resolution, 1 MHz analog-to-digital speed, 72 channels, and a sampling rate of up to 1 MHz.[34] The data sampling rate used for the present study is 500 kHz for a period of 20 ms.

WaveBook software includes WaveView,[34] a graphical Windows-based data acquisition program that enables one to acquire data for immediate viewing, or for storage on a desktop PC hard disk. The point-and-click interface simplifies the hardware set-up, without programming or connecting icons. The intuitive control automatically queries the WaveBook upon connection to the PC. Specific channel characteristics, such as gain, are automatically updated. The data collected by the WaveView are stored as a text file on the hard disk and can be easily exported to a Microsoft spreadsheet for preparing graphical results. A simple block diagram, shown in Fig. 2.20, is presented for a better understanding of the various connections in the data acquisition equipment.

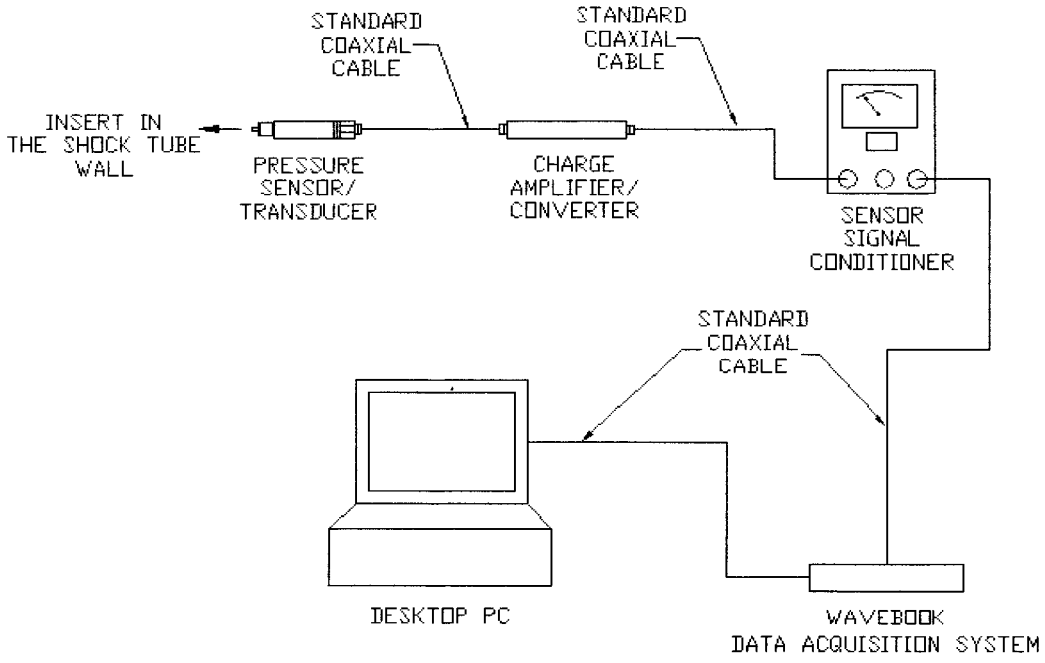

Figure 2.20 Block diagram of data acquisition equipment.

2.2.12 Apparatus Assembly

In the previous sections, all the necessary components required for the experimental apparatus are described and discussed. An important step is to assemble

these components to produce a mechanically sound working system. The apparatus was assembled at the northeast corner of the aerodynamics laboratory (Room E-33 at Ryerson University). In the early stages of assembly, because the outlet air valve of the reservoir tank is at 0.6 m from the ground, a wooden table was constructed so that the whole assembly could be mounted on this table. The table was rigidly attached to the ground and various clamps were used to screw the apparatus to the table. The clamping was very rigid, so as to withstand the high-speed flow and high operating pressures. The driver (secondary) chamber was connected to the outlet valve for utilising air from the reservoir tank.

The driven and driver chambers were cut to the required lengths and the diaphragm holder flanges were coupled to the chambers at one end. Pressure, temperature and transducer taps were made on both of the channel sections at the desired locations. This was done because it was easier to prepare such taps before connecting the chambers to the desired air source. The free end of the driver chamber was connected to the outlet valve of the reservoir tank through an isolation ball valve. The air supply to the driver chamber from the reservoir tank was connected at the boost pressure port.

At the other free end of the driven channel, a converging-diverging nozzle, or an orifice plate, was attached. The overhead air distribution line was connected to this chamber at the primary air inlet port. A diaphragm was loaded in the diaphragm holder and placed in the diaphragm flange. It was further screwed tightly with nuts and bolts, so as to avoid any air leakage.

The various pressure and temperature gauges were mounted on the respective taps. A panel having control valves to monitor the air supply to both chambers was secured permanently and labelled on a nearby cabinet. The complete assembly with all the necessary dimensions is shown in Fig. 2.21. It should be noted that the wooden table on which apparatus was mounted and the control panel having various pressure measuring gauges and valves to control air supply to both chambers and the data acquisition system are not shown in Fig. 2.21.

Once the design of the shock tube was completed and the apparatus was constructed, the assembly was thoroughly checked for air leakages, proper mounting of various gauges, leak-proof connections in piping, etc. The preliminary testing procedures

are listed in Appendix A. A detailed list of procedures for operating the apparatus, conducting tests, and shutting down the apparatus is given in Appendix A.

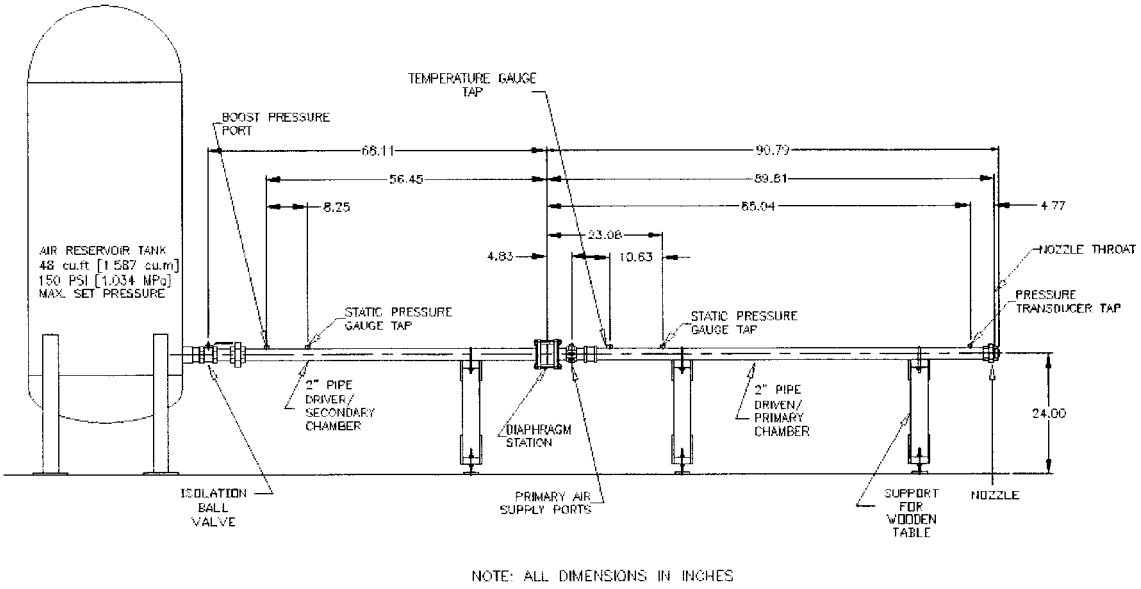

Figure 2.21 Assembly of shock tube apparatus.

Chapter 3 Computational Fluid Dynamics (CFD) Analysis

The CFD analysis for the present investigation, which yields various numerical flow simulation results, is done with the help of FLUENT (Version 6.0). The following sections provide an introduction to FLUENT, its features and its capabilities.

3.1 Introduction to FLUENT

FLUENT is a computer program for modeling fluid flow involving simple or complex geometries. FLUENT provides the capability for solving flow problems via a grid (i.e., a mesh) that is generated inside or around the flow domain of interest. There are several mesh types that are supported by FLUENT, including triangular, quadrilateral, tetrahedral, hexahedral, pyramid, and wedge shapes. These meshes may be high in density (fine) or low in density (coarse), depending on the required flow solution. This capability is useful for accurately predicting flow fields.

FLUENT is written in C computer language. True dynamic memory allocation, efficient data structures, and flexible solver control are the main features of this software. All functions required to compute a solution and display the results are accessible in FLUENT through an interactive, menu-driven interface. The FLUENT package contains:

1. FLUENT, the solver.
2. GAMBIT, the pre-processor for geometry modeling and mesh generation.

One can create the flow model geometry and grid in GAMBIT (Version 2.0.4). Once the grid has been generated and read into FLUENT, the FLUENT solver performs all the remaining operations. These operations include defining physical models and fluid properties, setting boundary conditions, executing the solution, and viewing the results. The FLUENT solver has the following relevant modeling capabilities:[35]

1. Flows in 2D or 3D geometries.
2. Incompressible or compressible flows.
3. Steady state or transient analysis.
4. Inviscid, laminar, and turbulent flows.

FLUENT is capable of handling triangular and quadrilateral elements (or a combination of the two) in two dimensions, and tetrahedral, hexahedral, pyramid, and wedge elements (or a combination of these) in three dimensions. This flexibility allows one to pick mesh topologies that are best suited for a particular application. One can adapt all types of meshes in FLUENT in order to resolve large gradients in the flow field, but the initial mesh should always be generated outside the solver, using GAMBIT or any other CAD package for which the mesh import filters are available in FLUENT.

3.2 Preparation for CFD Analysis

Prior to starting to solve the problem in FLUENT, several aspects were considered. It was decided that a 2D axisymmetric flow model would be adequate to serve the present purpose. The best-suited grid elements were selected and various boundaries were chosen for applying specific boundary conditions related to the flow model. Also, different numerical computational schemes and the process of collecting static pressure variations with time at specific locations were decided. Careful consideration of these key points will contribute to meaningful and successful results. The following sections provide details of the analysis.

3.3 Procedural Steps for Solving Problem

After determining the important features of the problem, the following steps are followed to solve the problem:

1. Create a 2D axisymmetric flow model geometry and grid in GAMBIT.
2. Export the grid as a mesh file.
3. Import (i.e., read) the mesh file in FLUENT through a case file.
4. Check the grid and the grid scale.
5. Select the solver for solving the problem.
6. Choose the basic equations by specifying viscous and energy models.

7. Specify the material properties as air.
8. Specify the boundary conditions.
9. Adjust the solution control parameters.
10. Initialize the flow field and patch the custom field functions.
11. Calculate the solution.
12. Examine the results.
13. Save the results as a data file.

3.4 Inputs for CFD Analysis

This section describes the various input parameters for conducting the CFD analysis.

3.4.1 Model Construction

Since the experimental apparatus is axisymmetric about the x-axis, an axisymmetric model is used in FLUENT. A 2-D, axisymmetric model is generated in GAMBIT to represent the upper half of the experimental shock tube apparatus. The model has dimensions that correspond to the experimental apparatus (see Chapter 2). A schematic diagram is shown in Fig. 3.1.

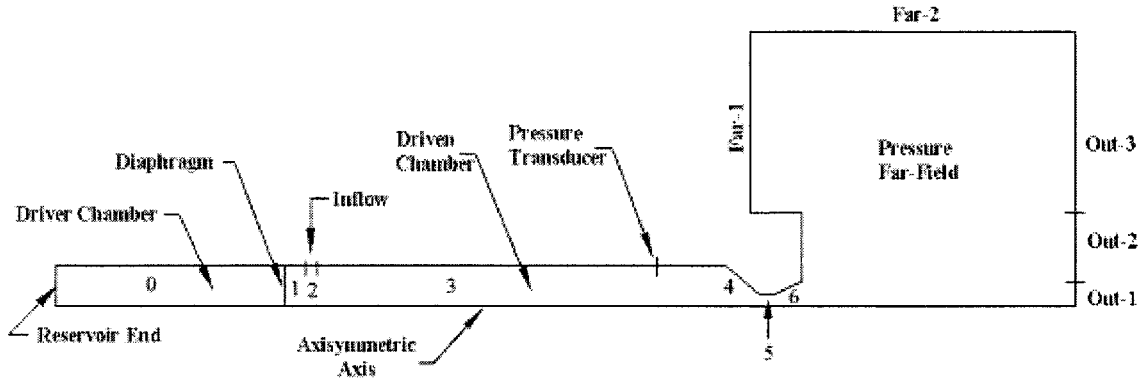

Figure 3.1 A 2D axisymmetric model for CFD analysis.

In Fig. 3.1, some of the edges are named for applying the boundary conditions and regions are numbered for initializing the flow conditions. In addition, a pressure far-field is introduced to model a free-stream compressible flow downstream, with free-stream Mach number and static conditions to be specified.

3.4.2 Grid Generation

After constructing the model, the next step is to generate a mesh in GAMBIT. The choice of grid depends largely on the type of flow to be modeled. However, a few other considerations, such as set-up time, computational expense, and numerical diffusion, should also be given importance. Since the geometry is two-dimensional, the choice of grid cells is restricted to quadrilateral and triangular only. It is common practice to choose quadrilateral cells for simple geometries, in which the flow conforms to the geometry. Furthermore, these cells permit a higher aspect ratio (which is a measure of the stretching of the cell) and also minimize numerical diffusion. Hence, for this particular study, quadrilateral cells are used.

The mesh to be generated should be of good quality and resolution so as to yield high accuracy and stability during numerical computations. Factors contributing to mesh quality are node point distribution, smoothness, and skewness. The flow characteristics depend on the density and the distribution of nodes in the mesh. However, a balance is maintained by keeping all the above factors in mind. Rapid changes in cell volume between adjacent cells, leading to truncation error (which is the difference between the partial derivatives in the governing equations and their discrete approximations), are avoided wherever possible. Highly skewed cells (defined by the difference between the cell's shape and the shape of an equilateral cell of equivalent volume) are avoided as they may decrease the accuracy and destabilize the solution. The grid in the converging-diverging nozzle is shown in Fig. 3.2. A similar grid is used for the other flow regions.

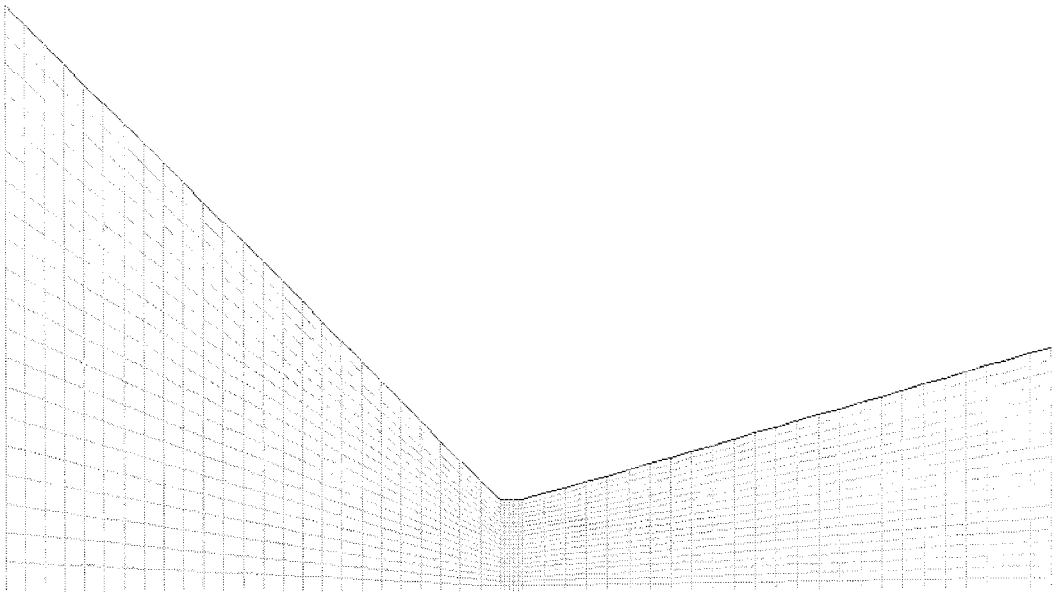

Figure 3.2 Grid in the converging-diverging nozzle (enlarged view).

3.4.3 Exporting and Importing of Mesh

Once the model has been generated, faces are created through wire frame edges, various zones (i.e., regions) are defined, different boundary types are defined, and geometry has been meshed; this information is then exported to FLUENT as a mesh file. This file contains the coordinates of all the nodes, connectivity information that tells FLUENT how the nodes are connected to one another to form faces, and the zone types and numbers/names of all the faces. The file does not contain any boundary conditions, flow parameters, or solution parameters. These characteristics are applied to the existing model in FLUENT.

The mesh file is imported/read directly into FLUENT through a case file (i.e., an input file whose format is understood by FLUENT and is used to read a mesh file). After reading a mesh file, the grid should be checked in FLUENT for possible errors. The area and volume statistics should always be positive; if they are found to be negative, the implication is that one or more cells have improper connectivity, and one should

eliminate these negative values before starting the flow solution process. Simultaneously, grid size and scale should be verified.

3.4.4 Selection of Numerical Schemes

FLUENT employs two alternative numerical methods:[35]

1. Segregated solver
2. Coupled solver

Either method solves the governing equations for mass, momentum, and energy by means of a control-volume-based technique. This technique consists of the following: (i) discretization, i.e., division of the entire domain into discrete control volumes and integration of the governing equations over these individual control volumes to construct algebraic equations for the dependent variables such as pressure, velocity, and temperature, etc., (ii) linearization of these algebraic equations, and (iii) solution of the resulting linear equation system to determine new values of the dependent variables.

In the case of the segregated solver, the governing equations are solved sequentially (i.e., segregated from one another), whereas in case of the coupled solver, the governing equations are solved simultaneously (i.e., coupled together). Both methods employ a finite-volume discretization procedure. However, the approach used to linearize and solve the discretized algebraic equations is different for the two methods. Of these two numerical methods, the coupled solver is used for the present investigation. Iterations of the solution are performed until a converged solution is obtained.

Discretization involves the use of an upwind scheme. This enables fluid and flow values in a given cell to be updated from the values in the cell upstream i.e., upwind. Among the several upwind schemes available in FLUENT, a second-order upwind scheme is used. This is particularly useful when second-order accuracy is desired.

The resulting non-linear algebraic equations are linearized with the help of an implicit or explicit approach. In the implicit approach, for a given variable, the unknown value in each cell is computed using a relation that includes both existing and unknown values from neighbouring cells. Therefore each unknown will appear in more than one

equation in the system, and these equations are solved simultaneously to give the unknown variables. In the explicit approach, for a given variable, the unknown value in each cell is computed using a relation that includes only the existing values. Therefore each unknown will appear in only one equation in the system and the equations for the unknown value in each cell are solved one at a time to give the unknown variables. In the present study, both (implicit and explicit) approaches are employed for linearization of the algebraic equations. In the implicit approach, Gauss-Siedel method in conjunction with an algebraic multigrid (AMG) method is used to solve the system of linear equations, whereas in the explicit approach, Runge-Kutta method is used to solve the system of linear equations. Fig. 3.3 shows a block diagram of control-volume-based technique.

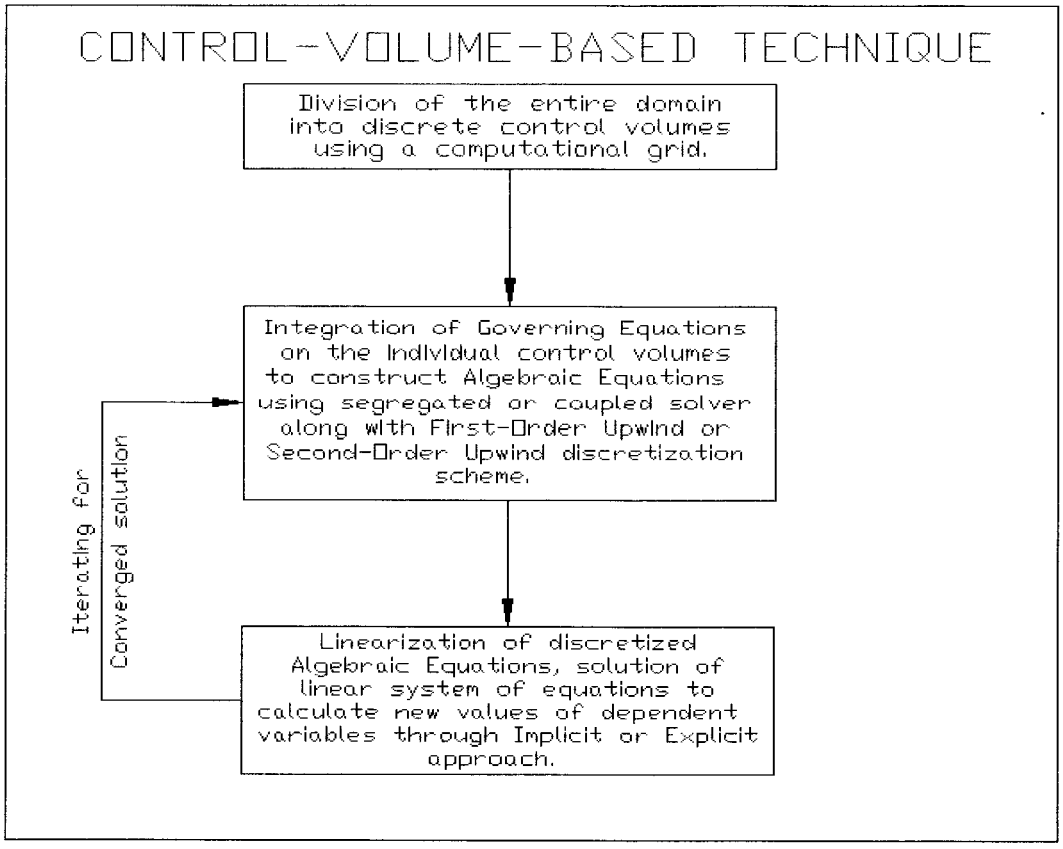

Figure 3.3 Control-volume-based technique.

The solution process for the particular numerical simulation of the shock tube flow application is divided into two stages. The first stage pertains to the steady-state

flow process, which simulates the flow with the diaphragm in place and air passing through the driven (primary) chamber. The next stage pertains to the transient flow process, which simulates the flow after the diaphragm is ruptured with the incident normal shock wave travelling downstream towards the nozzle. A list of all the selected solution options is given below:

1. Coupled solver
2. Implicit for steady-state and Explicit for transient state formulation
3. Energy solver
4. Axisymmetric model
5. Steady-state and transient state formulation

In addition to the above listed solution options, the present analysis includes the modeling of turbulence. FLUENT provides the following turbulence models:[35]

1. Spalart-Allmaras model
2. $k-\varepsilon$ models:
    a. Standard $k-\varepsilon$ model
    b. Renormalization-group (RNG) $k-\varepsilon$ model
    c. Realizable $k-\varepsilon$ model
3. $k-\omega$ models:
    a. Standard $k-\omega$ model
    b. Shear-stress transport (SST) $k-\omega$ model
4. Reynolds stress model (RSM)
5. Large eddy simulation (LES) model

Among the above models, no single turbulence model is best suited for all types of problems. Hence, the choice of the model depends on established practice for a specific class of problem, level of accuracy required, available computational resources, amount of time available for the simulation, etc.

After considering the computational requirements, the $k-\varepsilon$ (RNG) turbulence model was chosen for the present application. This model is quite simple and reliable for many practical engineering flow problems. Robustness, economy in computational time, and reasonable accuracy are a few of its salient features. The model is derived from the

Navier-Stokes equations, using a mathematical technique called renormalization group (RNG) theory.

3.4.5 Physical Properties of Working Medium and Operating Pressure for FLUENT

One of the important steps in the set-up of the model is the defining of the physical properties of the material involved. In FLUENT, one defines the physical properties of fluids and solids as required. These properties are relevant to the modeling problem and generally include density, molecular weight, viscosity, heat capacity, thermal conductivity, mass diffusion coefficients, kinetic theory parameters, etc. A list of the reference properties for the present case, with air as the working medium, is given below:

1. Density: Ideal gas density
2. Specific heat at constant pressure: 1006.43 J/kg-K
3. Thermal conductivity: 0.0242 W/m-K
4. Dynamic Viscosity: 1.7894×10^{-5} kg/m-s
5. Molecular weight: 28.966 kg/kgmol

In FLUENT, the operating pressure can be absolute pressure or gauge pressure. Since it is necessary to use absolute pressure for high-speed compressible flows, for the present model, the operating pressure is absolute.

3.4.6 Boundary Conditions

Boundary conditions are applied for the flow at the boundaries of the model. Various boundary types are available in FLUENT such as mass flow inlet, pressure outlet, pressure far-field, outflow, etc. In Fig. 3.1, various edges are specified with

appropriate boundary types. The boundary conditions for each edge are listed in Appendix D.

In addition, each axis is defined as an axisymmetric axis boundary type, grid as an interior boundary type, each region having fluid as a fluid boundary type, and each wall as a wall boundary type.

It should be noted that, initially, for steady-state flow, the diaphragm is considered as a wall boundary type (indicating that the diaphragm is not ruptured), and for transient flow, the diaphragm is considered as an interior boundary type (indicating that it is removed).

3.4.7 Defining Custom Field Functions

Custom field functions are scalar functions defined by the user for initializing flow conditions, prior to beginning the flow solution process. These functions are patched to each zone/region (see Fig. 3.1) in terms of scalar values or in the form of a function. In FLUENT, all the custom field functions are evaluated and stored in SI units; hence, care should be taken while entering these functions for analysis. A list of these functions is given in Appendix D.

3.4.8 Defining Solution Control Parameters

Basically, under-relaxation factors are used to control the update (i.e., reduce the change) of computed variables at each iteration. In FLUENT, the default under-relaxation factors are set to values that are near to optimal and suitable for almost all problems. One can either increase or decrease these factors depending on the magnitude of the residuals. In the case of a segregated solver, all equations will have under-relaxation factors associated with them; if a coupled solver is used then only those equations that are solved sequentially will have under-relaxation factors. For the present model, the default values of under-relaxation factors are used.

For the coupled flow solvers in FLUENT, the main control over time stepping is via the Courant Friedrichs Lewy (CFL) number, and the time step is proportional to the CFL requirement. Linear stability theory determines a range of permissible values (i.e., for which a given numerical scheme will remain stable) for the CFL criterion. After specifying a CFL number value, FLUENT automatically computes an appropriate time step. In general, a larger time step leads to faster solution convergence of solution for a steady-state flow problem, so it is advantageous to set the CFL number as large as possible but within the permissible range.

In the case of a coupled implicit solver, linear stability theory shows that the Gauss-Siedel scheme is unconditionally stable. The default CFL value for such a solver is 5. However, it is possible to increase the value to 20, 50, 100, or even higher depending on the complexity of the problem. The solver also has the capability of detecting divergence and, if this happens, it will automatically reduce the CFL value and again perform the iteration. Initially, during the start-up of the solution, a lower value of CFL may be more suitable, but as the solution progresses, it may be increased with increasing number of iterations.

In the case of a coupled explicit solver, the default value of the CFL number is 1, but one may be able to increase the value up to 2.5 in a few 2D problems. In the present model, a CFL value ranging from 1 to 5 with increasing number of iterations is chosen for the steady-state flow and a CFL value of 0.75 is chosen for the transient flow. The various solution control parameters are given in Appendix D.

FLUENT also provides an option of keeping the solution stable under extreme conditions by providing limits to the solution within an acceptable range. The limiting values can be applied to pressure, temperature and various other quantities. The purpose of these limits is to keep the absolute pressure, temperature, and other quantities from becoming zero, negative, or excessively large during the iterative calculations.

3.4.9 Defining Monitors

Residual monitors are defined in order to check the solution convergence dynamically during the solution process. A residual for the coupled solvers is the time

rate of change of any variable. One can print and plot the residual values for all relevant variables. For unsteady flows, one can also monitor the elapsed time. FLUENT provides scaled and unscaled residual monitors. In general, it is difficult to judge convergence by examining the unscaled residual, since no scaling (i.e., no comparison with other residual values) is employed. However, in scaled residuals, scaling is done on the basis of residual values obtained from a certain number of iterations. These scaled residuals are useful indicators of solution convergence. Convergence criteria can be modified for each variable being monitored. The solution will stop automatically when each variable meets its specified convergence criterion. Variables to be monitored and checked for convergence are listed in Appendix D.

In addition to residual monitors, surface monitors are also defined in the model in order to record the static pressure at given locations as a function of time. In the model, data are collected at 10 cm upstream of the nozzle (corresponding to the pressure transducer location in the experimental study) in addition to other axial locations, and at the wall and at the centre axis of the shock tube. This information is stored in an output file. The area-weighted average for a given cell location is the means of data collection for the surface monitors.

3.4.10 Convergence

A large number of computational cells, overly conservative under-relaxation factors, and complex flow are a few of the main factors causing a hindrance to solution convergence. There are no universal rules for judging convergence of a solution. Residual definitions for convergence that are useful for one type of problem are sometimes misleading for other types of problems. Therefore, it is a good idea to judge convergence not only by examining residual levels, but also by monitoring relevant integrated quantities such as pressure, velocity, and temperature, etc. Generally, for a majority of flow problems, the convergence criterion is that the residual levels decrease to at least 10^{-3} (except in the case of the energy equation, for which the criterion is around 10^{-6}). The convergence criterion for various equations is defined in Appendix D.

3.4.11 Steady-State Flow Calculations

With respect to the first stage of the solution process, i.e., steady-state flow, the number of iterations to be performed are set and then FLUENT begins calculations using the custom field functions. The monitors are updated automatically after each iteration. These iterations are performed until the solution convergence criteria are met.

3.4.12 Transient Flow Calculations

With respect to the second stage of the solution process, i.e., transient flow, the solution data set obtained from steady-state flow calculations is used as a starting point for performing the transient flow calculations. These calculations are performed to obtain time-dependent phenomena, including the capturing of the transient behaviour of a moving shock wave. Similar to steady-state flow calculations, iterations are performed till a converged final solution is obtained. The location of the moving incident shock wave can be visualized by displaying flow contour diagrams at a given time step. As noted in Section 3.4.9, the static pressure at various locations in the channel is monitored, to provide additional information.

3.4.13 Flow Contours

A number of graphic tools are available in FLUENT, which allow processing of the information contained in the CFD solution and allowing one to easily view the results. One can generate graphic displays showing grids, contours, profiles, vectors, and pathlines. In FLUENT, one can also plot contour lines superimposed on the physical domain. Contour lines are lines of constant magnitude for a selected variable. It is possible to obtain colour-filled contours instead of default line contours, to specify the range of values to be contoured, to choose the portions of the grid to be displayed, and to store plots. One can also draw flow vectors in the entire domain or on selected surfaces. Each flow vector is drawn at the centre of the cell, with length and colour of the arrows

representing the magnitude of the selected variable. However, for tracking the incident and reflected shock wave, contour plots are generated each time the solution is stopped for interim evaluation.

Chapter 4 Results and Discussion

4.1 Experimental Results for Reference C-D Nozzle

After the diaphragm in the shock tube is ruptured, a normal shock wave moves downstream towards the nozzle, the pressure transducer records the pressure data associated with the passage of this incident shock and the data are transmitted to the acquisition system. The data are static pressure values at a specified position (viz., 10 cm upstream of the nozzle, at the wall), which vary with time. Various experimental firings were conducted for driven channel pressures of 340 kPa, 375 kPa, 409 kPa and 444 kPa (absolute pressure) with a converging-diverging nozzle having a 45° convergence half-cone angle and an orifice plate having a 0° inclination.

Figs. 4.1, 4.2, 4.3, and 4.4 show overpressure-time profiles for the driven channel pressures of 340 kPa, 375 kPa, 409 kPa, and 444 kPa, respectively. Fig. 4.5 depicts an enlarged view of Fig. 4.2. These channel pressures are considered as the zero reference for the overpressure values in the respective graphs. As soon as the travelling incident normal shock wave reaches the transducer location, the step change in pressure experienced by the transducer triggers it, and the time is denoted by $t = 0$. It is clear from the profiles that the incident shock overpressure is approximately 170 kPa.

The incident (compression) shock wave travels downstream and is reflected from the nozzle convergence section. As can be seen from the figures, the reflected shock is detected by the pressure transducer at $t \approx 0.5$ ms, for all cases. The reflected shock is manifested as a pressure step with an initial spike in pressure, followed by a series of progressively decaying secondary oscillations superimposed on the quasi-equilibrium base overpressure of 420 kPa, approximately.

The incremental overpressure (i.e., the magnitude) of the initial pressure spike in the various experimental overpressure-time profiles for a 45° C-D nozzle range from 55 to 75 kPa, or correspondingly about 13 to 18 % of the reflected shock's base strength. It appears that there is an increase in the overpressure of the initial pressure spike with increasing driven channel pressure. This observed trend is discussed later in the chapter.

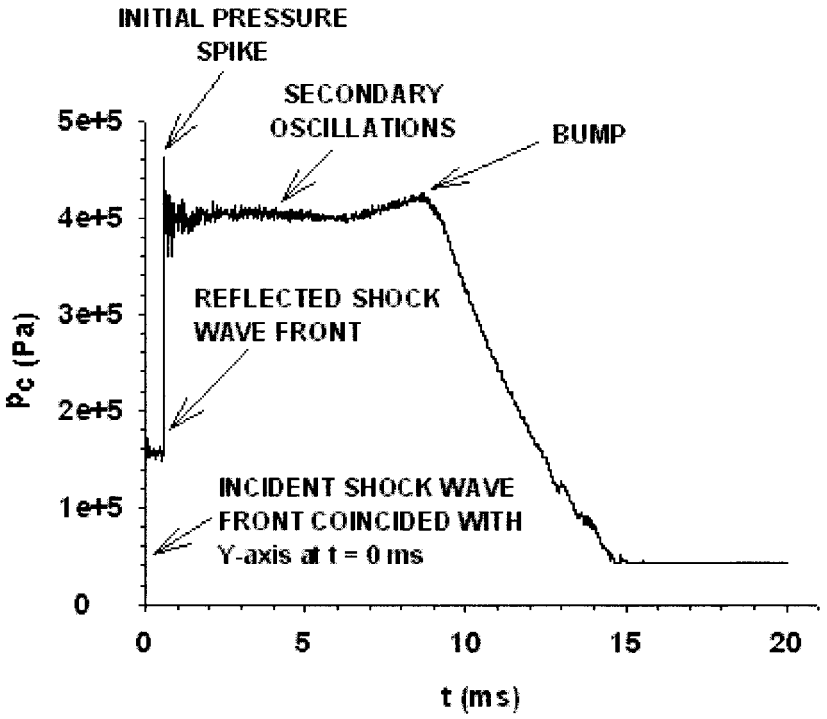

Figure 4.1 Overpressure-time profile for a driven channel pressure of 340 kPa, C-D nozzle.

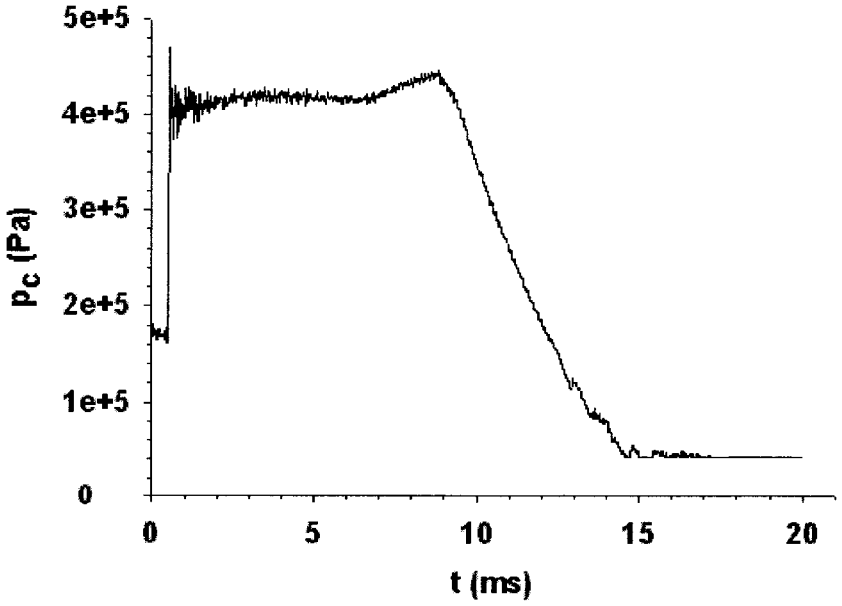

Figure 4.2 Overpressure-time profile for a driven channel pressure of 375 kPa, C-D nozzle.

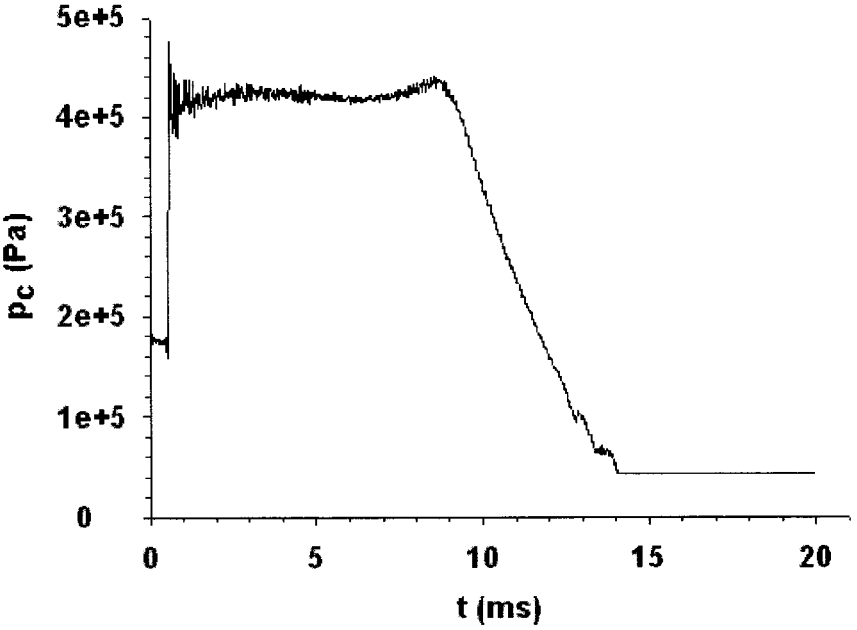

Figure 4.3 Overpressure-time profile for a driven channel pressure of 409 kPa, C-D nozzle.

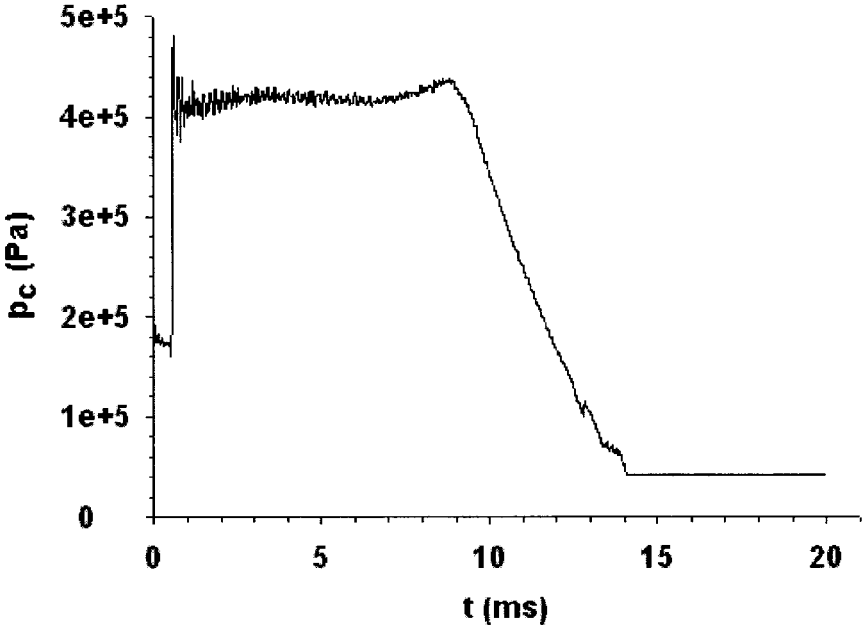

Figure 4.4 Overpressure-time profile for a driven channel pressure of 444 kPa, C-D nozzle.

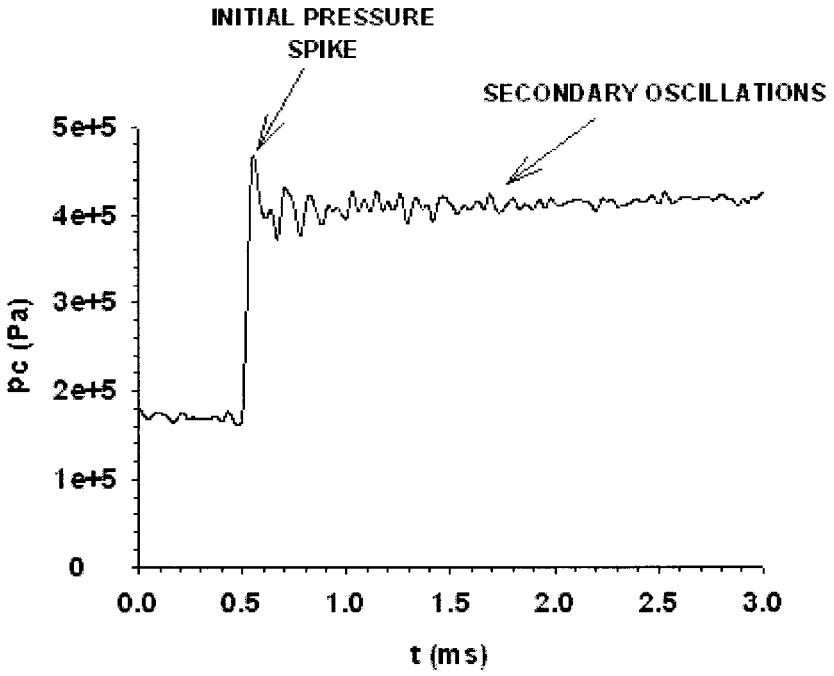

Figure 4.5 Enlarged view of the reflected shock pressure profile for a driven channel pressure of 375 kPa, C-D nozzle.

The secondary oscillations have a characteristic frequency that corresponds to the fundamental radial pressure wave frequency at that location of the chamber, which is given by:[2,22]

$$f_{1R} = 1.22\left(\frac{a_5}{d_1}\right), \tag{4.1}$$

where a_5 is the speed of the sound (as calculated in Chapter 2, page 24) and d_1 is the channel diameter (see Chapter 2, page 22).

Putting $a_5 = 370.65$ m/s and $d_1 = 0.0508$ m in Equation (4.1), one determines

$$f_{1R} = 1.22 * \left(\frac{370.65}{0.0508}\right) \approx 8.9 \text{ kHz}$$

However, the mean radial wave frequency in the various experimental overpressure-time profiles shown in Figs. 4.1, 4.2, 4.3, and 4.4 is around 8.3 kHz, 9 kHz, 11 kHz, and 9 kHz, respectively.

Eventually, the radial wave loses its strength with each reflection in the transverse direction. At around $t = 7.5$ ms, the pressure starts rising and forms a small ramp, which may be referred to as a "BUMP" as indicated in Fig. 4.1. After $t \approx 9.5$ ms, it is apparent that the principal *rarefaction* wave (which is initiated by the diaphragm removal, propagates upstream, and then downstream upon reflection at the driver end wall) passes by the transducer as it moves downstream. As a result, the pressure drops to the quasi-steady level.

4.2 Numerical Results for Reference C-D Nozzle

Numerical simulations of the flow in the shock tube are generated via FLUENT for the 45° C-D nozzle at a driven channel pressure of 375 kPa. For these simulations, both viscous and inviscid flow models are used. Also, static pressures are obtained at different axial and radial locations, viz., at 5 cm, 10 cm, and 15 cm upstream of the nozzle at the wall and at the centre axis of the shock tube. These numerical results will assist in the determination of any trends with regard to the radial wave activity occurring at different axial and transverse locations. The pressure profiles are presented in terms of the absolute static pressure (rather than with a gauge reference).

Fig. 4.6 shows the predicted profile, based on the viscous flow model, pertaining to a location of 5 cm upstream of the nozzle at the wall, and Fig. 4.7 depicts an enlarged view of Fig. 4.6. At the wall, 5 cm upstream of the nozzle, the magnitude of the predicted initial pressure spike (see Fig. 4.7) is similar to that in the experimental overpressure-time profile, which pertains to 10 cm upstream of the nozzle (see Fig. 4.5). The corresponding mean radial wave frequency is around 8.83 kHz in agreement with the value of about 8.9 kHz determined at the wall, 10 cm upstream of the nozzle. Notice that the radial wave activity for the experimental result (Fig. 4.5) has a longer duration and is stronger as compared to the numerical result at the wall, 5 cm upstream of the nozzle (Fig. 4.7).

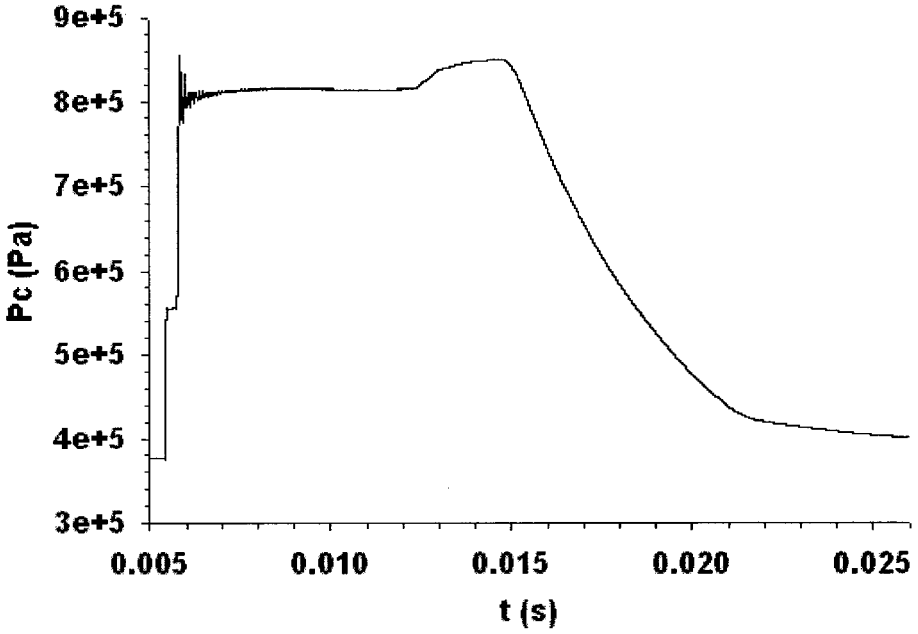

Figure 4.6 Predicted pressure-time profile for a driven channel pressure of 375 kPa, 5 cm upstream of C-D nozzle, at the wall of the shock tube.

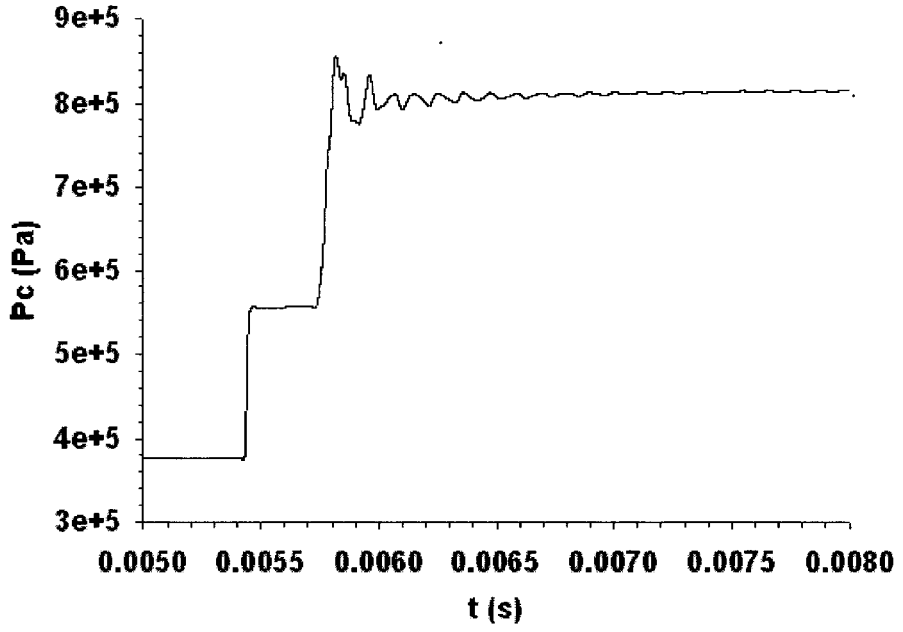

Figure 4.7 Enlarged view of predicted pressure-time profile for a driven channel pressure of 375 kPa, 5 cm upstream of C-D nozzle, at the wall of the shock tube.

In addition to obtaining the pressure at the wall of the shock tube, the predicted pressure is also obtained at the centre axis of the shock tube. Obtaining the pressure at the centre axis of the shock tube will help in determining any potential differences in the radial wave activity occurring at different transverse locations. The pressure-time profile at the centre axis of the shock tube at 5 cm upstream of the nozzle is presented below in Fig. 4.8, with an enlarged view shown in Fig. 4.9.

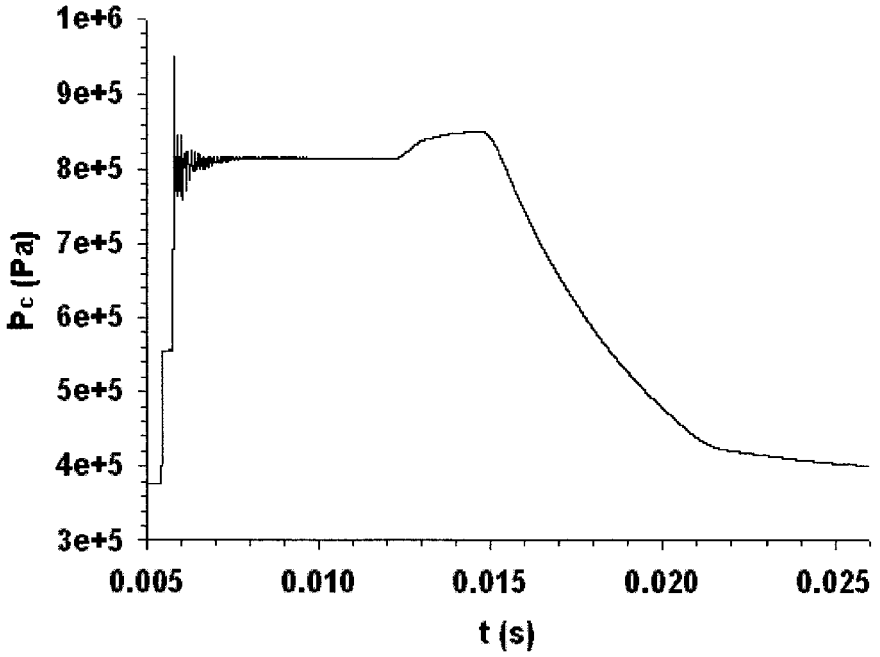

Figure 4.8 Predicted pressure-time profile for a driven channel pressure of 375 kPa, 5 cm upstream of C-D nozzle, at the centre axis of the shock tube.

At the centre axis of the shock tube, 5 cm upstream of the nozzle, the magnitude of the initial pressure spike is of the order of 150 kPa, relative to the reflected shock's base strength (see Fig. 4.9), whereas for the same axial channel position, the magnitude of the predicted initial pressure spike at the wall of the shock tube is of the order of 50 kPa (see Fig. 4.7). Also, at the centre axis, the radial waves are stronger. In general, one would expect radial waves to strengthen as one moves radially from the wall of the shock tube towards the centre axis of the shock tube. The mean radial wave frequency at the centre axis, 5 cm upstream of the nozzle, is around 8.56 kHz, lower than that at the wall of the shock tube (8.83 kHz).

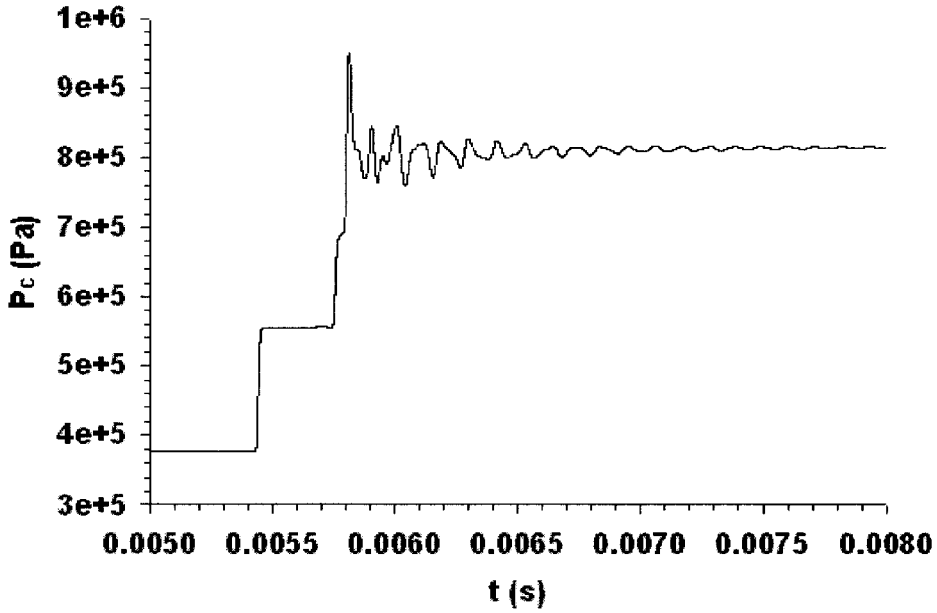

Figure 4.9 Enlarged view of predicted pressure-time profile for a driven channel pressure of 375 kPa, 5 cm upstream of C-D nozzle, at the centre axis of the shock tube.

The numerical results at the wall, 10 cm upstream of the nozzle, are presented in Figs. 4.10 and 4.11.

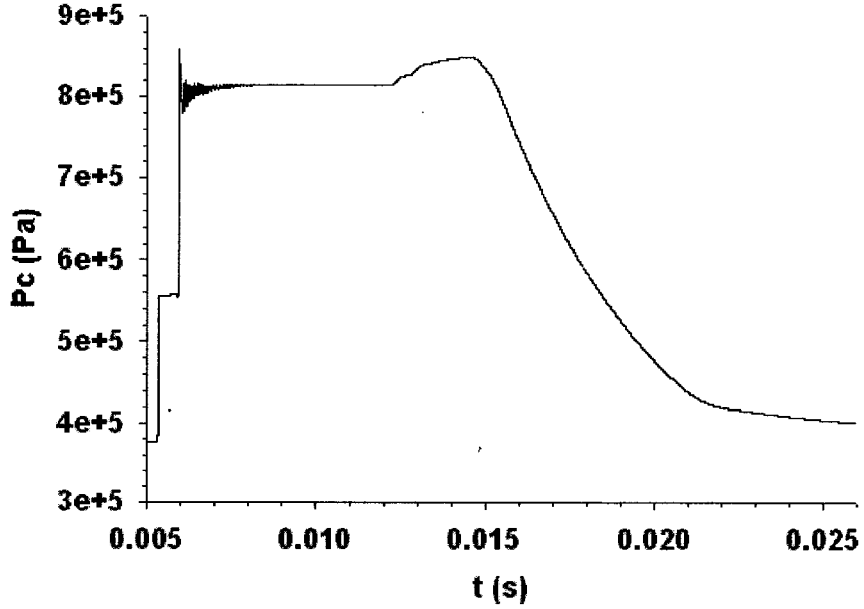

Figure 4.10 Predicted pressure-time profile for a driven channel pressure of 375 kPa, 10 cm upstream of C-D nozzle, at the wall of the shock tube.

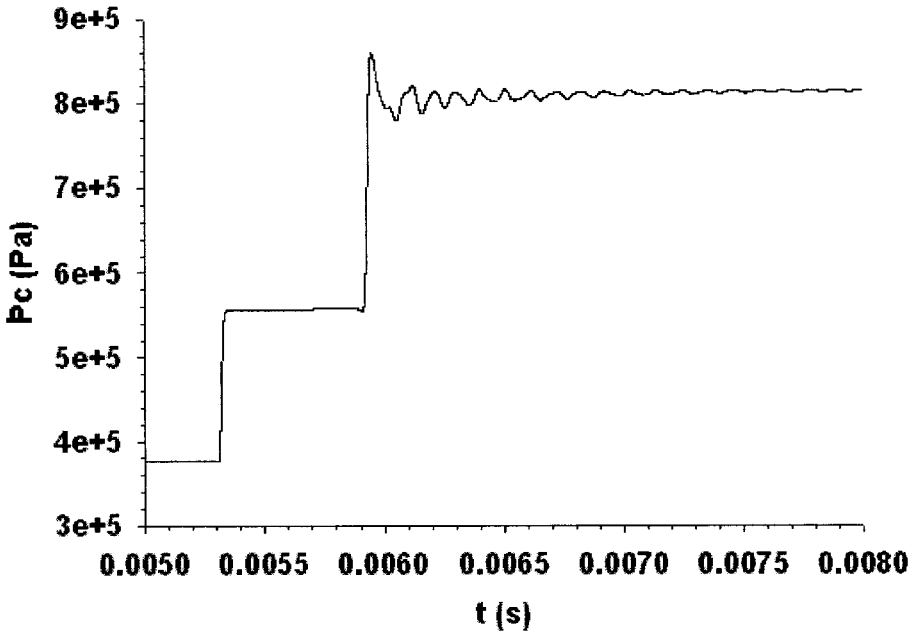

Figure 4.11 Enlarged view of predicted pressure-time profile for a driven channel pressure of 375 kPa, 10 cm upstream of C-D nozzle, at the wall of the shock tube.

The magnitude of the predicted initial pressure spike in Fig. 4.11 is approximately the same as that obtained for the experimental overpressure-time profile in Fig. 4.5, for the same axial position at the wall. Also, the experimental and numerical profiles (see Figs. 4.5 and 4.11) exhibit a similar value for the mean radial wave frequency. However, the strength of the secondary oscillations appears to be somewhat less in the predicted case.

Figs. 4.12 and 4.13 show the numerical results at the centre axis of the shock tube, 10 cm upstream of the nozzle. A comparison of Figs. 4.11 and 4.13 indicates that the magnitude of the predicted initial pressure spike is lower at the centre axis than it is at the wall, i.e., the radial waves at the centre axis are superimposed on an initially lower quasi-equilibrium base pressure, unlike the previous observations for the 5-cm position. At the centre axis, the mean radial wave frequency is around 8.2 kHz, lower as compared to that at the wall of the shock tube (8.9 kHz).

Similar to the 5 cm case (Figs. 4.7 and 4.9), the radial wave activity at the 10-cm position (Figs. 4.11 and 4.13) is more pronounced at the centre axis of the shock tube

than at the wall of the shock tube. Also, the mean radial wave frequency is lower at the centre axis than it is at the wall.

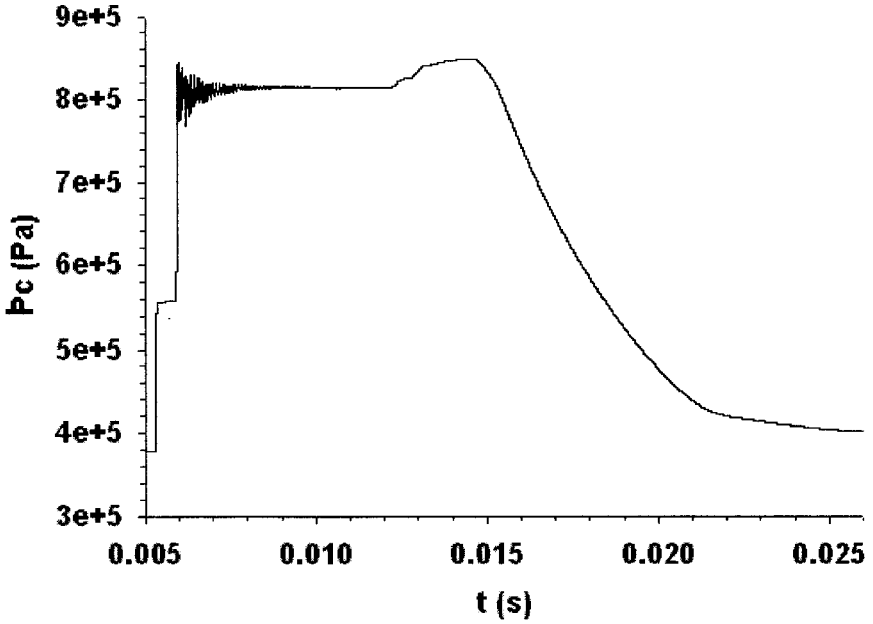

Figure 4.12 Predicted pressure-time profile for a driven channel pressure of 375 kPa, 10 cm upstream of C-D nozzle, at the centre axis of the shock tube.

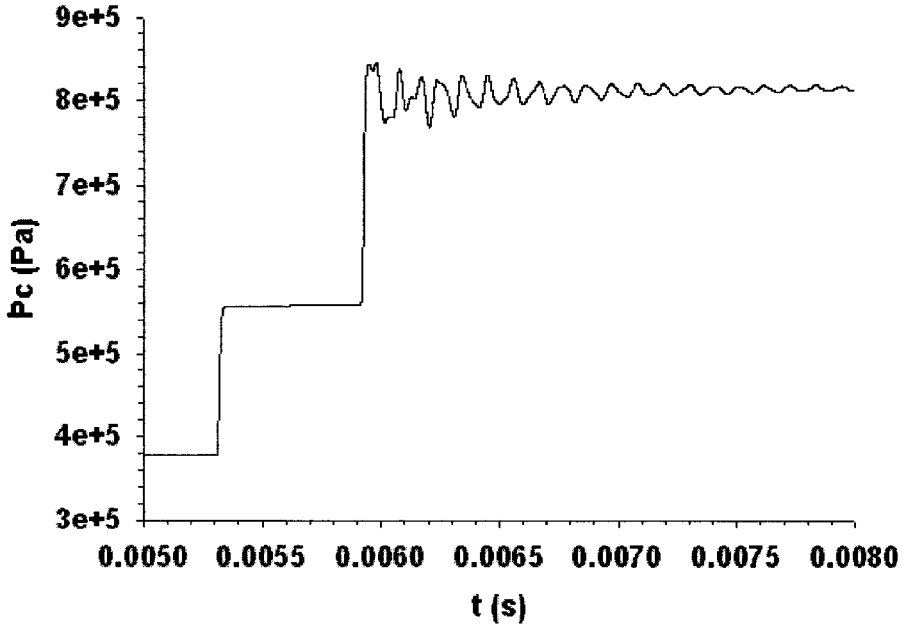

Figure 4.13 Enlarged view of predicted pressure-time profile for a driven channel pressure of 375 kPa, 10 cm upstream of C-D nozzle, at the centre axis of the shock tube.

A pressure-time profile for a driven channel pressure of 375 kPa at 10 cm upstream of a 45° C-D nozzle (as in the viscous case) is predicted numerically with an inviscid flow model, so as to ascertain the influence of gas viscosity on the results discussed earlier. The results are presented in Figs. 4.14 (at the wall) and 4.15 (at the centre axis of the shock tube).

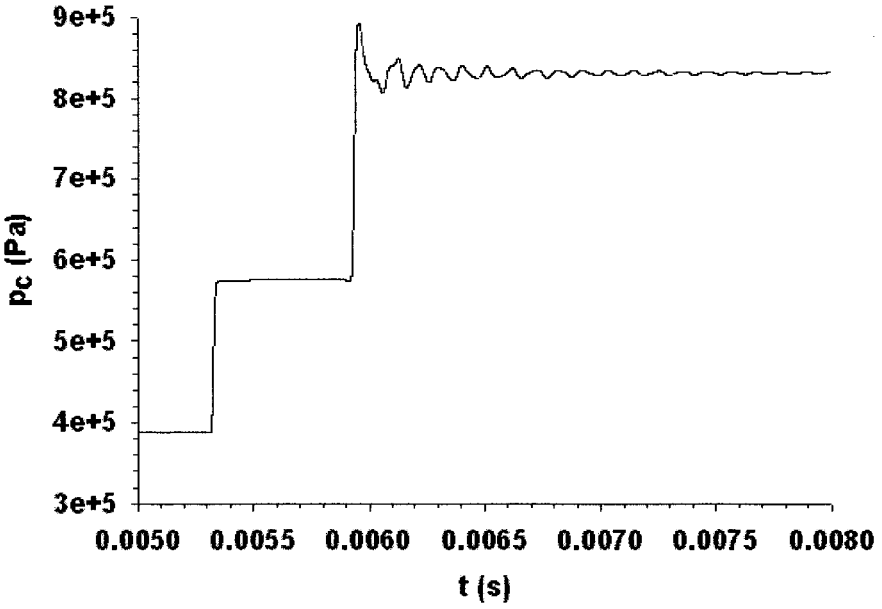

Figure 4.14 Enlarged view of predicted pressure-time profile for a driven channel pressure of 375 kPa, 10 cm upstream of C-D nozzle, at the wall of the shock tube, inviscid case.

The magnitudes of the predicted initial pressure spikes at the wall and at the centre axis of the shock tube in the inviscid case (see Figs. 4.14 and 4.15) are similar to those presented in Figs. 4.11 and 4.13 for the viscous case. Other features, such as the strength and duration of the radial waves and the mean radial wave frequency, have comparable values for both the viscous and inviscid cases. The implication here is that the viscous effects on the pressure wave development are negligible. It should be noted that all the experimental and numerical pressure-time profiles discussed here are generated at a lower pressure than that used in practice, so there is the possibility that the viscosity/boundary layer effects might be more significant in a higher pressure scenario.

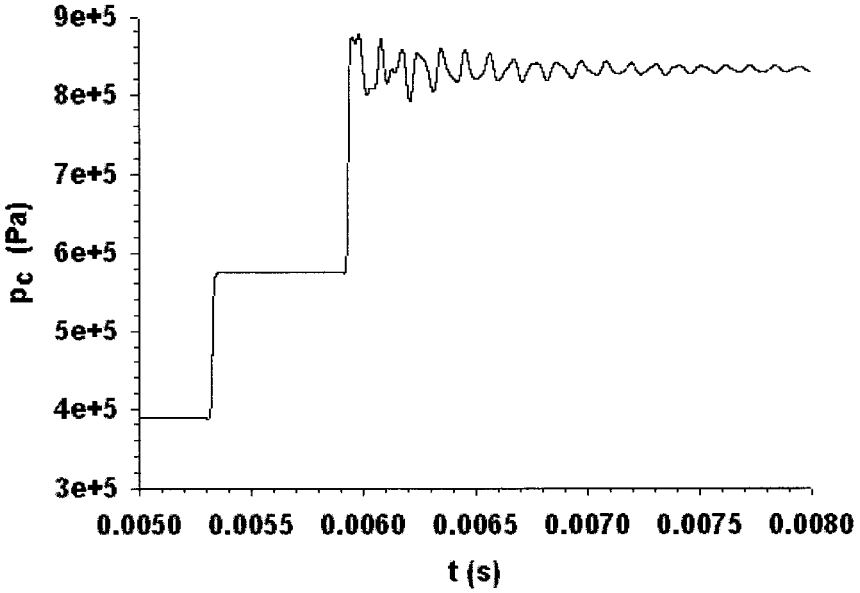

Figure 4.15 Enlarged view of predicted pressure-time profile for a driven channel pressure of 375 kPa, 10 cm upstream of C-D nozzle, at the centre axis of the shock tube, inviscid case.

The numerical results at the wall, 15 cm upstream of the nozzle are presented in Figs. 4.16 and 4.17. The magnitude of the predicted initial pressure spike is seen to be substantially lower (see Fig. 4.17) than that observed in the experimental overpressure-time profile (see Fig. 4.5). The mean radial wave frequency is marginally higher and the radial waves have a lower strength at 15 cm, when compared with the experimental profile in Fig. 4.5.

Figs. 4.18 and 4.19 show the numerical results at the centre axis of the shock tube, 15 cm upstream of the nozzle. Unlike the 10 cm case, the magnitude of the initial pressure spike is higher at the centre axis than that at the wall of the shock tube, as can be seen in Figs. 4.17 and 4.19. Similar trends for the initial pressure spike were observed in the 5 cm case; however, the values were different. The radial waves are stronger at the centre axis than at the wall of the shock tube in this case, as in the 5 cm and 10 cm cases. The mean radial wave frequency at the centre axis is marginally lower in this case to that in the 5 cm case; however, it is marginally higher than that in the 10 cm case.

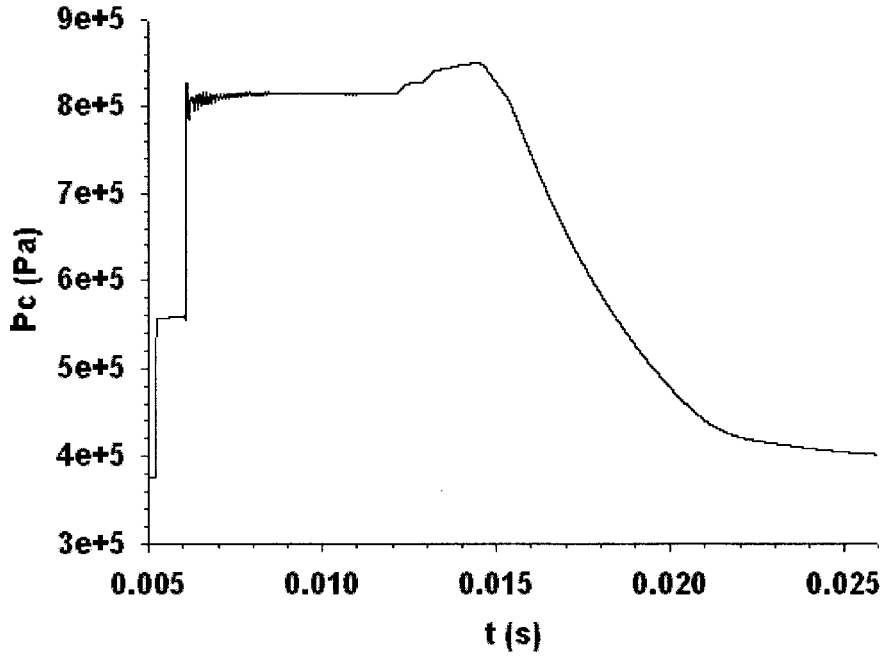

Figure 4.16 Predicted pressure-time profile for a driven channel pressure of 375 kPa, 15 cm upstream of C-D nozzle, at the wall of the shock tube.

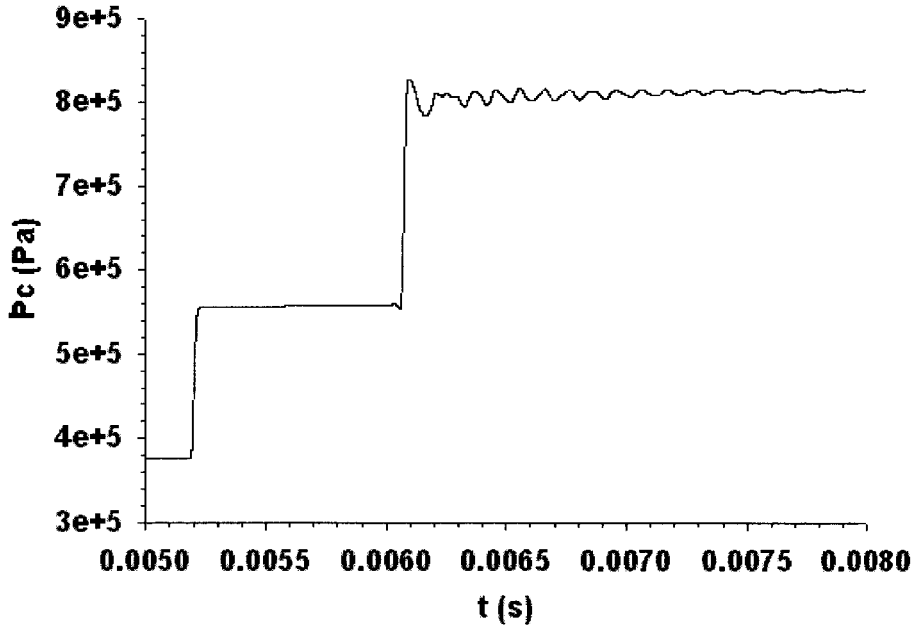

Figure 4.17 Enlarged view of predicted pressure-time profile for a driven channel pressure of 375 kPa, 15 cm upstream of C-D nozzle, at the wall of the shock tube.

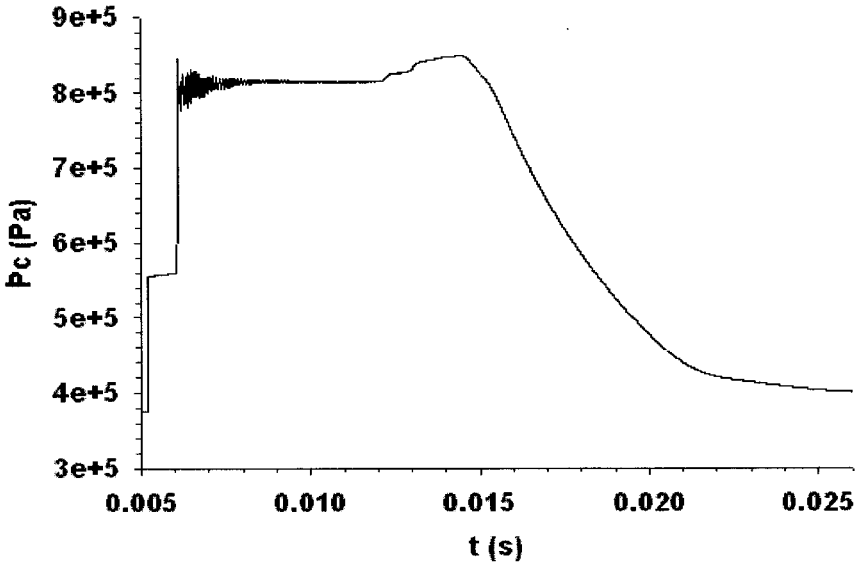

Figure 4.18 Predicted pressure-time profile for a driven channel pressure of 375 kPa, 15 cm upstream of C-D nozzle, at the centre axis of the shock tube.

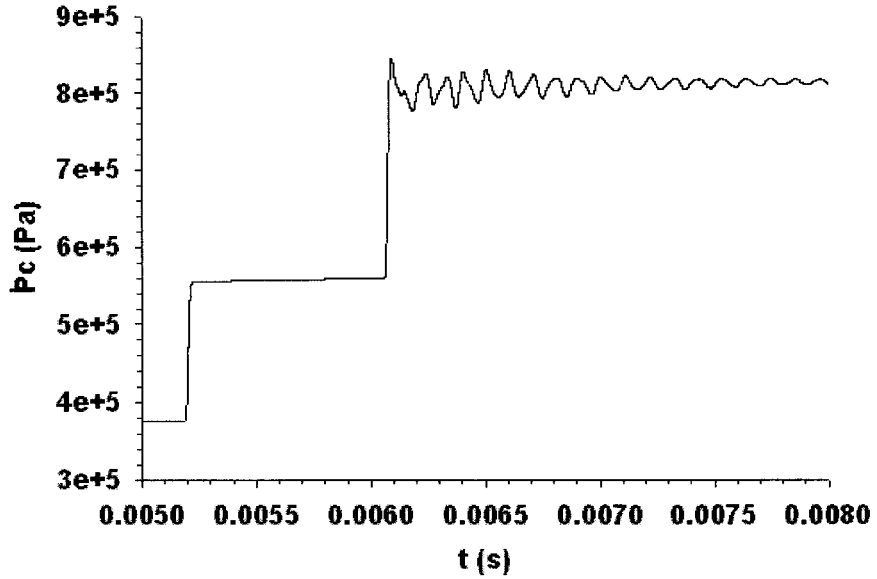

Figure 4.19 Enlarged view of predicted pressure-time profile for a driven channel pressure of 375 kPa, 15 cm upstream of C-D nozzle, at the centre axis of the shock tube.

The above experimental and numerical profiles at different driven channel pressures and at different axial and transverse locations exhibit a "BUMP" prior to the arrival of the principal rarefaction wave (e.g., Figs. 4.1, 4.6, 4.8, and 4.10). The

explanation for the appearance of such a "BUMP" can be established through an estimation of the approximate time of arrival of compression waves (at the transducer location) that arise due to the collision between the upstream-moving reflected shock wave and the downstream-moving contact surface. Further in time, the reflected shock wave moves upstream after the collision and interacts with the mass input valve. As a result, another set of downstream-moving waves is generated. This estimation process can involve the use of flow contour diagrams, which illustrate the static pressure variation along the length of the shock tube and which enhances the visualization of the waves moving upstream and downstream. Graphs showing the spatial distribution of pressure along a given axis of interest can also be employed. The observed pressure difference enables one to determine the location of pressure waves along the length of the shock tube. The above visualization tools at different selected flow times are presented in Figs. 4.20, 4.21, 4.22, 4.23, 4.24, 4.25, and 4.26.

The pressure flow contour at t = 4.008 ms is shown in Fig. 4.20, and the corresponding spatial distribution of the pressure is shown in Fig. 4.21. It is clear from the latter that the incident shock wave front is located at 1.66 m from the diaphragm station. The expected time of arrival of the incident shock wave front at x = 1.66 m can therefore be estimated as

$$t_{i_{expected}} = \frac{x}{V_S}, \tag{4.2}$$

where V_S is the velocity of the incident shock wave (see Chapter 2, page 23).

Putting $V_S = 415.575$ m/s and $x = 1.66$ m in Equation (4.2), one obtains

$$t_{i_{expected}} = 3.994 \text{ ms},$$

which is in good agreement with the selected flow time of 4.008 ms.

Fig. 4.22 depicts the pressure flow contour at t = 5.5634 ms. It can be seen that the incident shock wave front is located at the nozzle entrance, which is at 2.3 m from the diaphragm station. The expected time of arrival of the incident shock wave front at x = 2.3 m can be obtained as above, from Equation (4.2) as

$$t_{i_{expected}} = \frac{2.3}{415.575} = 5.534 \text{ ms},$$

which is again in good agreement with the selected flow time of 5.5634 ms.

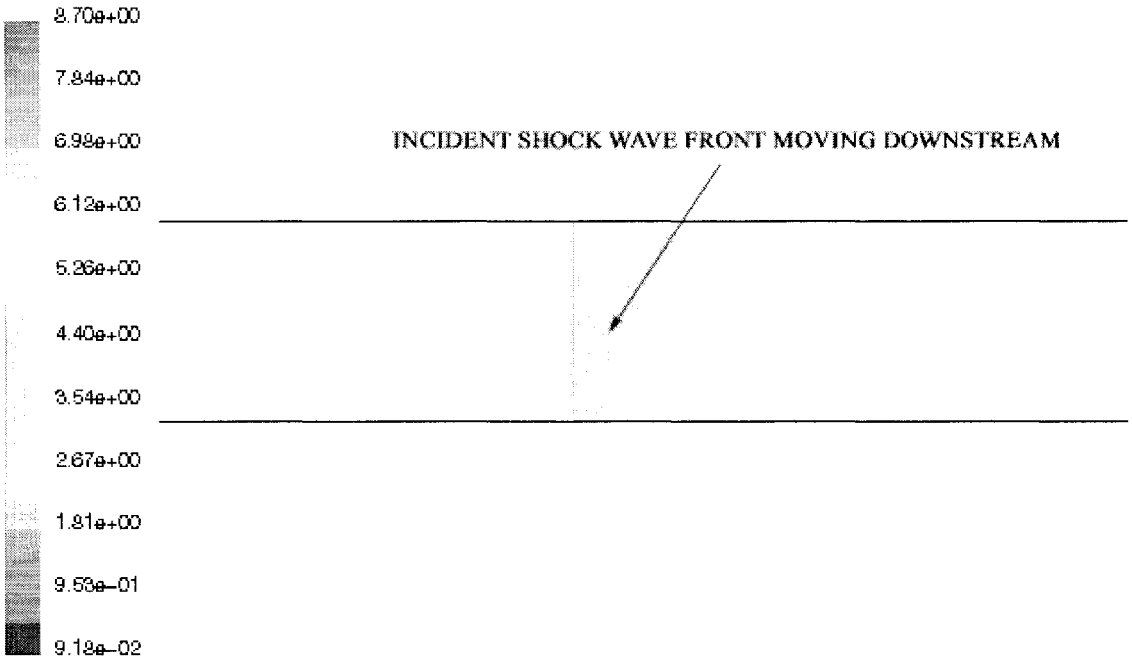

Figure 4.20 Pressure flow contour at $t = 4.008$ ms.

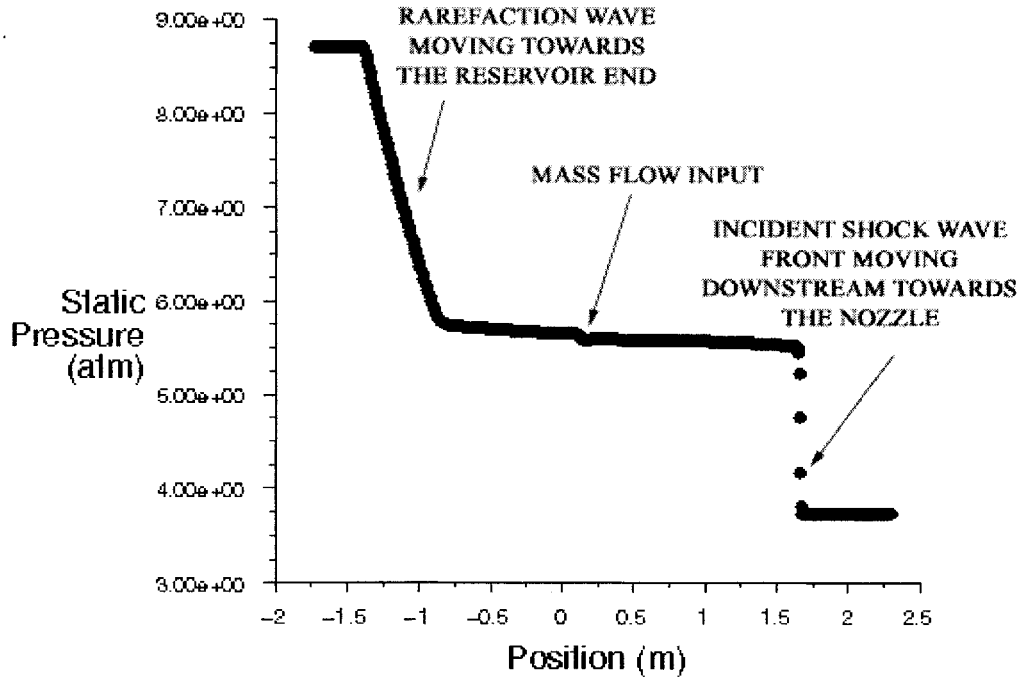

Figure 4.21 Static pressure variation along the length of the shock tube relative to diaphragm station at $t = 4.008$ ms, centre axis (nozzle region not included).

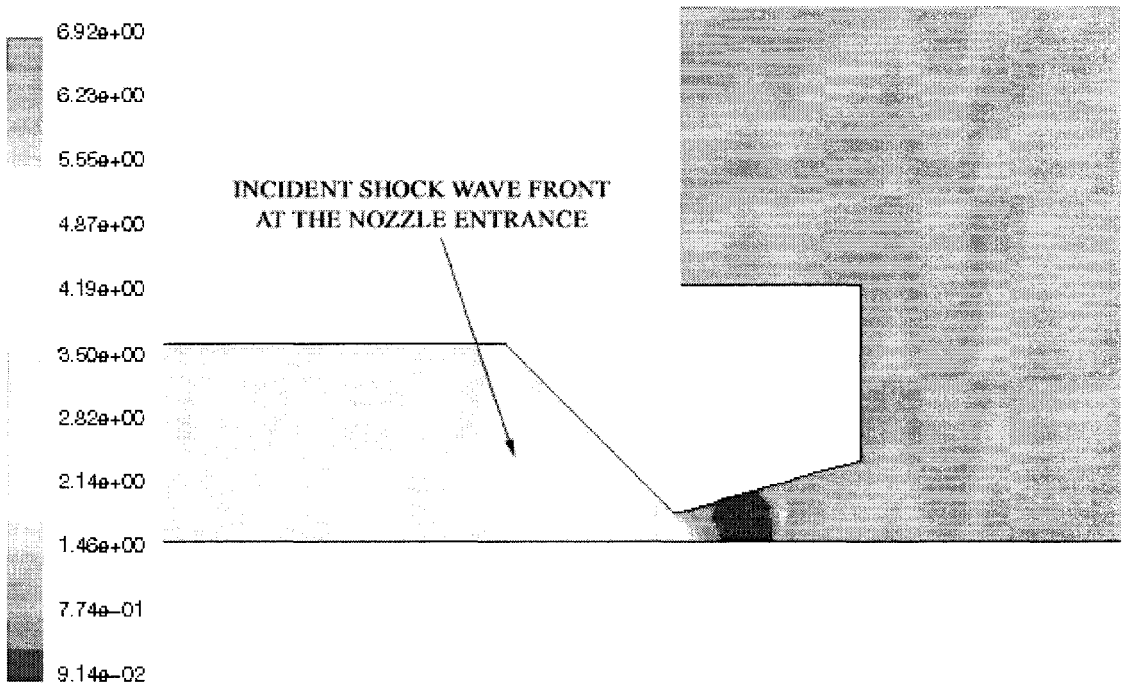

Figure 4.22 Pressure flow contour at $t = 5.5634$ ms.

The appearance of the reflected shock wave front near the nozzle entrance is depicted in Fig. 4.23.

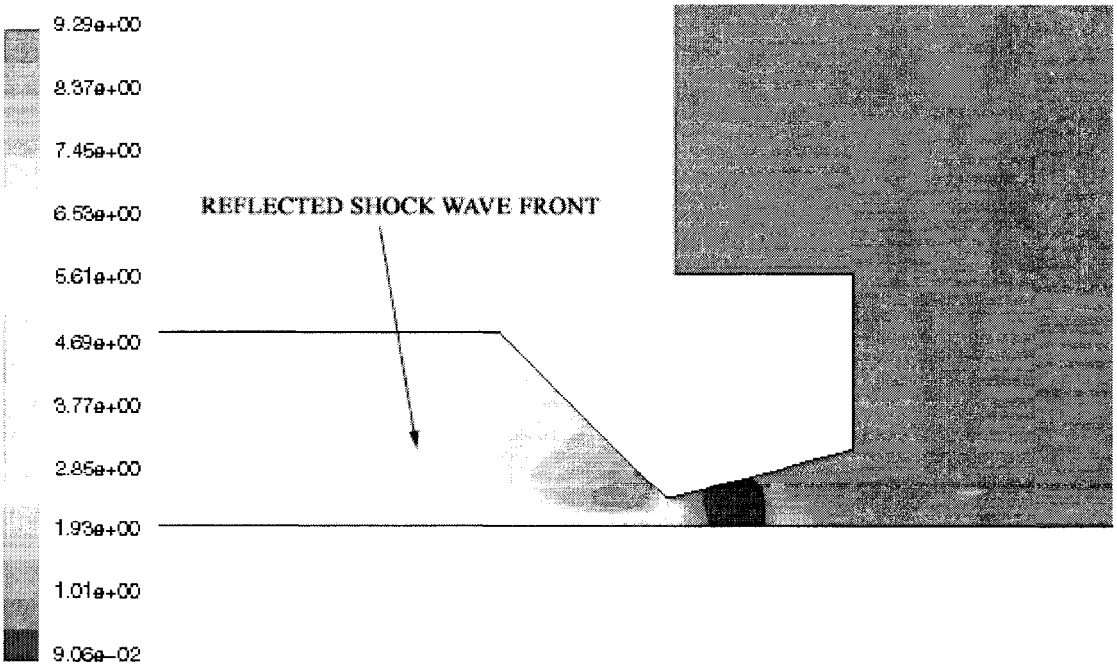

Figure 4.23 Pressure flow contour near the nozzle entrance.

The pressure flow contour at t = 8.9598 ms is shown in Fig. 4.24. The corresponding spatial distribution of the pressure is shown in Fig. 4.25, from which it follows that the reflected shock wave front is located at 1.22 m from the diaphragm station. The expected time of arrival of the reflected shock wave front at x = 1.22 m is given by Equation (4.3)

$$t_{R_{\exp ected}} = t_{i_{\exp ected}} + \frac{\Delta x_R}{V_R}, \tag{4.3}$$

where $t_{i_{\exp ected}}$ is the time of arrival of the incident shock wave front at the nozzle entrance, i.e., x = 2.3 m, (as calculated above), Δx_R is the distance travelled by the reflected shock wave front from the nozzle entrance along the axis of the shock tube, and V_R is the velocity of the reflected shock wave front (as calculated in Chapter 2, page 24).

Putting $t_{i_{\exp ected}}$ = 5.534 ms, Δx_R = 1.22–2.3= –1.08 m, and V_R = –277.10 m/s in Equation (4.3), one obtains

$$t_{R_{\exp ected}} = 5.534 \times 10^{-3} + \frac{(-1.08)}{(-277.10)} = 0.009431 = 9.431 \text{ ms}$$

From Figs. 4.24 and 4.25, it is evident that the reflected shock wave front arrives at x = 1.22 m at t = 8.9598 ms. Seeing that the expected time (9.431 ms) and the selected flow time (8.9598 ms) are significantly different, it can be concluded that the reflected shock wave front is moving faster than the quasi-equilibrium estimate of 277.10 m/s. On the basis of Equation (4.3), one can write

$$t_{R_{new}} = t_{i_{\exp ected}} + \frac{\Delta x_R}{V_{R_{new}}},$$

where $t_{R_{new}}$ is the selected time pertaining to the pressure flow contour presented in Fig. 4.24, and $V_{R_{new}}$ is the increased mean velocity of the reflected shock wave front.

Hence,

$$V_{R_{new}} = \frac{\Delta x_R}{t_{R_{new}} - t_{i_{\exp ected}}} \tag{4.4}$$

Putting Δx_R = –1.08 m, $t_{R_{new}}$ = 8.9598 ms, and $t_{i_{\exp ected}}$ = 5.534 ms in Equation (4.4), one obtains

$$V_{R_{new}} = -315.789 \text{ m/s}$$

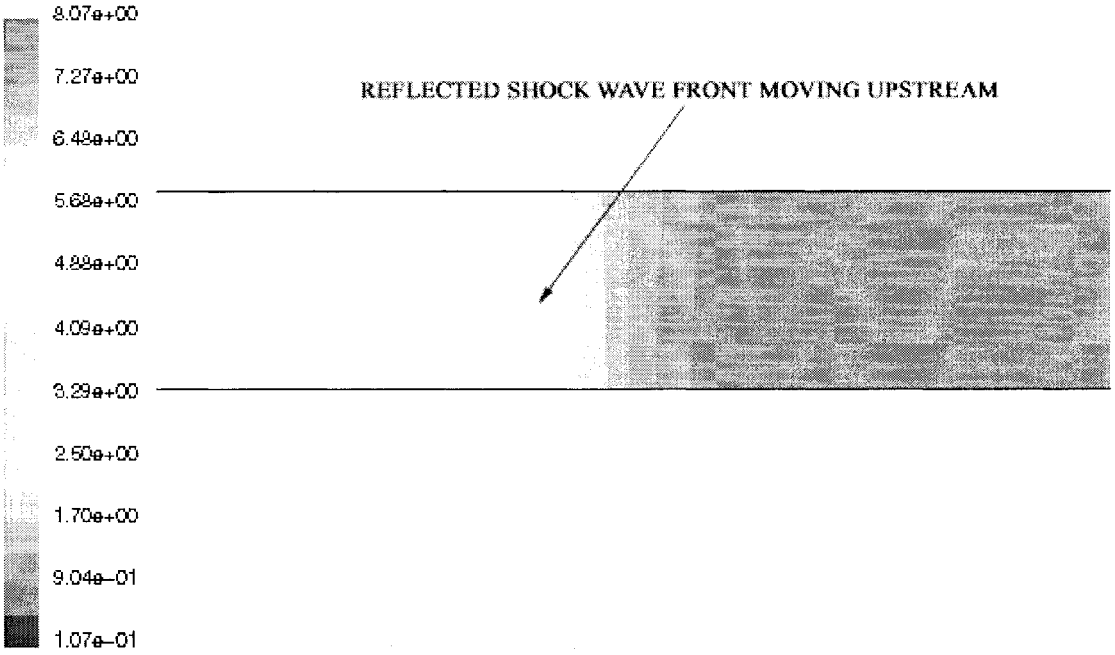

Figure 4.24 Pressure flow contour at $t = 8.9598$ ms.

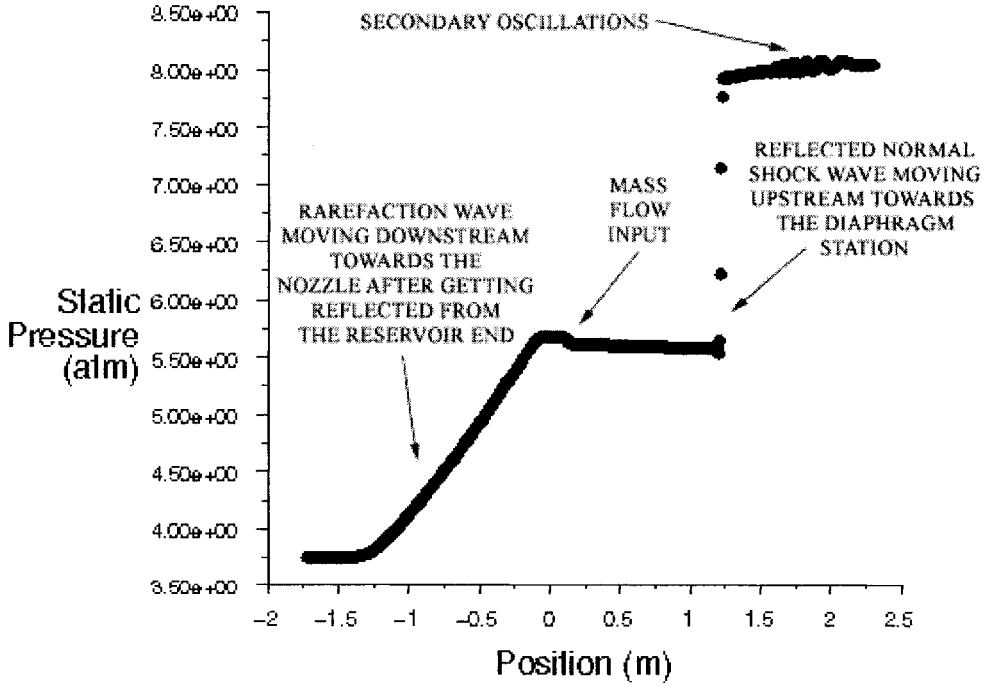

Figure 4.25 Static pressure along the length of the shock tube relative to diaphragm station at $t = 8.9598$ ms, centre axis (nozzle region not included).

Using, $V_{R_{new}} = -315.789$ m/s, the expected time of collision between the downstream-moving contact surface and the upstream-moving reflected shock wave front is determined by equating Equations (2.53) and (2.54), which yields

$$V_{cs}(t_2 + t_{test}) = V_S t_2 + V_R t_{test},$$

where,

V_{cs}=107.365 m/s (see Chapter 2, page 23)

$t_c = t_2 + t_{test}$ (from equation (2.51))

$l = V_S t_2$= 2.3 m (see Chapter 2, page 24)

$V_R = V_{R_{new}}$ = –315.789 m/s (as calculated above)

Hence, $$107.365(t_c) = 2.3 - 315.789(t_c - 5.534 \times 10^{-3})$$

so that $$t_c = 9.577 \text{ ms}$$

From Equation (2.56), the collision occurs at

$$x_c = V_{cs} t_c = 107.365 * 9.577 \times 10^{-3} = 1.02826 \text{ m},$$

relative to the diaphragm station. Therefore, the expected time of collision of the reflected shock wave front with the contact surface is given by

$$t_{\substack{R_{\text{expected}} \\ \text{at} \\ \text{collision}}} = t_{i_{\text{expected}}} + \frac{(x_c - 2.3)}{V_{R_{new}}} \tag{4.5}$$

Putting $t_{i_{\text{expected}}}$=5.534 ms, x_c=1.03 m, and $V_{R_{new}}$ = –315.789 m/s in Equation (4.5), one obtains

$$t_{\substack{R_{\text{expected}} \\ \text{at} \\ \text{collision}}} = 5.534 \times 10^{-3} + \frac{(1.03 - 2.3)}{-315.789} = 9.561 \text{ ms}$$

Fig. 4.26 depicts the pressure flow contour at t = 9.5768 ms. From the corresponding spatial distribution of the pressure (which is not shown), it follows that the location of the collision between the downstream-moving contact surface and the upstream-moving reflected shock wave front is in fact 1.03 m from the diaphragm station. This establishes that there is a reasonable correlation between the selected flow time (9.5768 ms) and the expected collision time (9.561 ms).

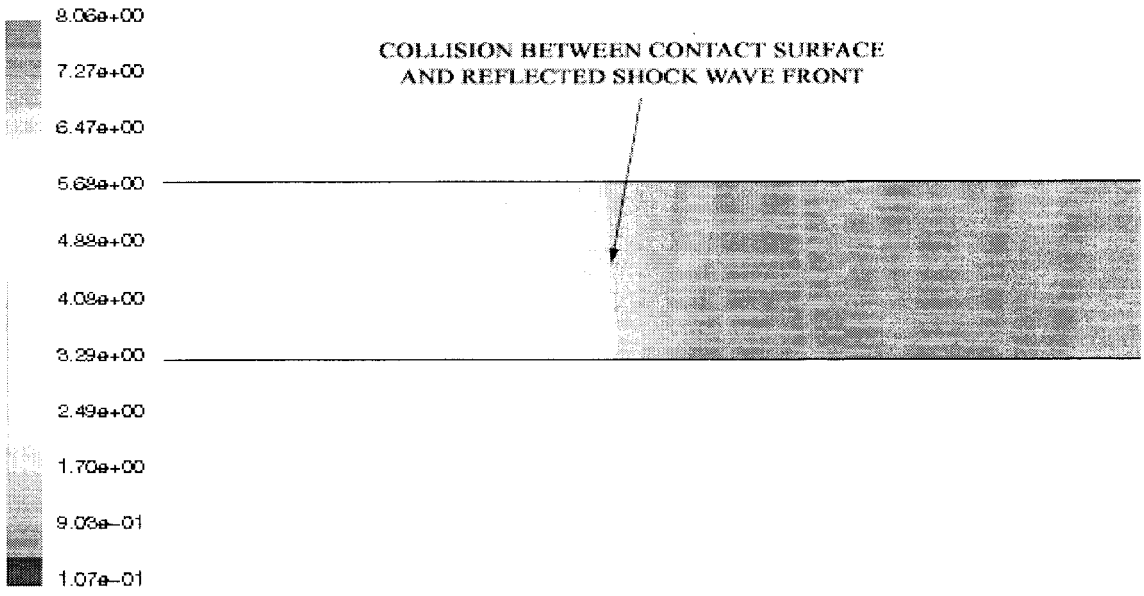

Figure 4.26 Pressure flow contour at $t = 9.5768$ ms.

After the collision between the downstream-moving contact surface and the upstream-moving reflected shock wave, new downstream-moving compression waves are generated. As soon as these compression waves arrive at the transducer location they form a small ramp referred to as BUMP A, as shown in Fig. 4.27. The expected time of arrival of these new compression waves at $x = 2.2$ m, which is the transducer location, can be estimated via

$$t_{CW-A} = t_{\substack{R_{\text{exp ected}} \\ \text{at} \\ \text{collision}}} + \frac{(x - x_c)}{(u_5 + a_5)}, \tag{4.6}$$

where $t_{\substack{R_{\text{exp ected}} \\ \text{at} \\ \text{collision}}}$ is the time taken by the reflected shock wave front to reach x_c, a_5 is the speed of sound (as calculated in Chapter 2, page 24), and u_5 is the local flow velocity (see Chapter 2, page 24). Putting $t_{\substack{R_{\text{exp ected}} \\ \text{at} \\ \text{collision}}} = 9.561$ ms, $x = 2.2$ m, $x_c = 1.03$ m, $a_5 = 370.65$ m/s, and $u_5 = 5.15$ m/s in Equation (4.6), one obtains the following estimate:

$$t_{CW-A} = 12.67 \text{ ms}$$

One can observe from Fig. 4.27 that BUMP A appears at $t = 12.3$ ms, which is in reasonable agreement with 12.67 ms. From this, one can conclude that BUMP A is

formed by the new downstream-moving compression waves resulting from the collision. Further in time, these compression waves move downstream and are reflected from the convergence region of the nozzle. The expected time of arrival of these reflected waves at the transducer location is estimated from Equation (4.7) given below

$$t_{CWR-B} = t_{CW-A} + \frac{|\Delta x|}{a_5 + u_5} + \frac{|\Delta x|}{a_5 - u_5} \tag{4.7}$$

where Δx is the distance between $x = 2.2$ m and the nozzle entrance.

Putting t_{CW-A}= 12.67 ms, Δx= 0.1 m, a_5=370.65 m/s, u_5=5.15 m/s in Equation (4.7), one obtains

$$t_{CWR-B} = 12.67 \times 10^{-3} + \frac{0.1}{(370.65 + 5.15)} + \frac{0.1}{(370.65 - 5.15)} = 13.21 \text{ ms}$$

BUMP B in Fig. 4.27 appears at 12.8 ms. Again, this is in reasonable agreement with t_{CWR-B}, signifying that the reflected waves are generated from the reflection of the new compression waves from the nozzle convergence region.

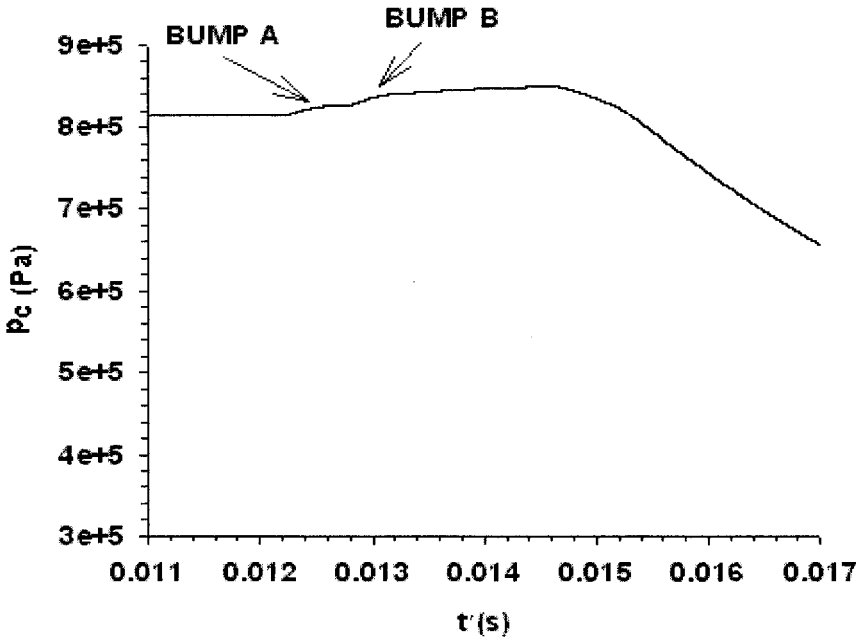

Figure 4.27 Enlarged view of predicted pressure bump for a driven channel pressure of 375 kPa, 10 cm upstream of the nozzle, at the wall of the shock tube.

The observed experimental trend of an increase in the pressure of the initial pressure spike with increasing driven channel pressure is investigated by numerically

predicting the pressure-time profiles at higher driven channel pressures of 444 kPa and 750 kPa (which is twice 375 kPa), as shown in Figs. 4.28 and 4.29.

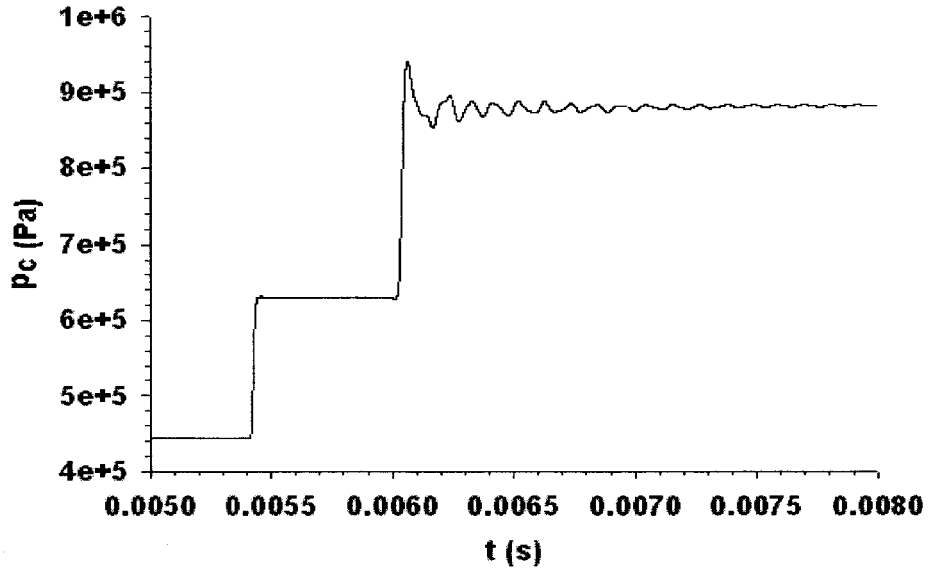

Figure 4.28 Enlarged view of predicted pressure-time profile for a driven channel pressure of 444 kPa, 10 cm upstream of C-D nozzle, at the wall of the shock tube.

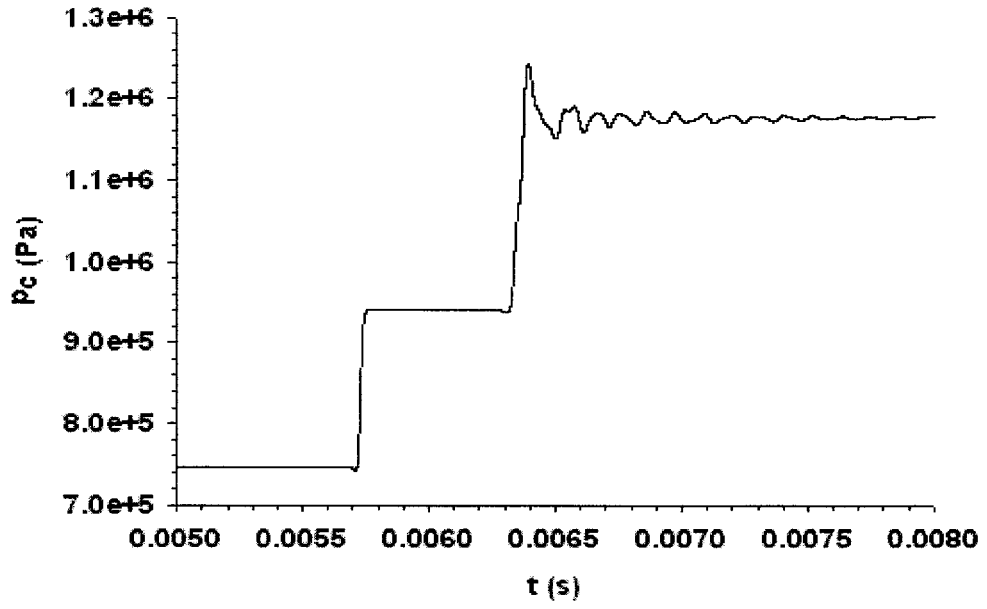

Figure 4.29 Enlarged view of predicted pressure-time profile for a driven channel pressure of 750 kPa, 10 cm upstream of C-D nozzle, at the wall of the shock tube.

The magnitudes of the initial pressure spike for driven channel pressures of 375 kPa, 444 kPa, and 750 kPa are 48 kPa, 60 kPa, and 64 kPa, respectively, relative to the reflected shock's base strength. These results suggest that the magnitude of the initial pressure spike depends on the driven channel pressure, increasing as the latter increases, but at a decreasing rate.

4.3 Experimental and Numerical Results for Orifice Plate

In addition to the above profiles for the reference nozzle, experimental and numerical profiles for the 0°-inclination orifice plate having the same experimental conditions as in the case of the C-D nozzle are shown below. It should be noted that the diameter of the orifice is the same as that of the reference C-D nozzle throat diameter. As before, the static pressure is measured at the channel wall, 10 cm upstream of the orifice plate. Figs. 4.30, 4.31, 4.32, and 4.33 show overpressure-time profiles for the driven channel pressures of 340 kPa, 375 kPa, 409 kPa, and 444 kPa, respectively. Fig. 4.34 depicts an enlarged view of Fig. 4.31.

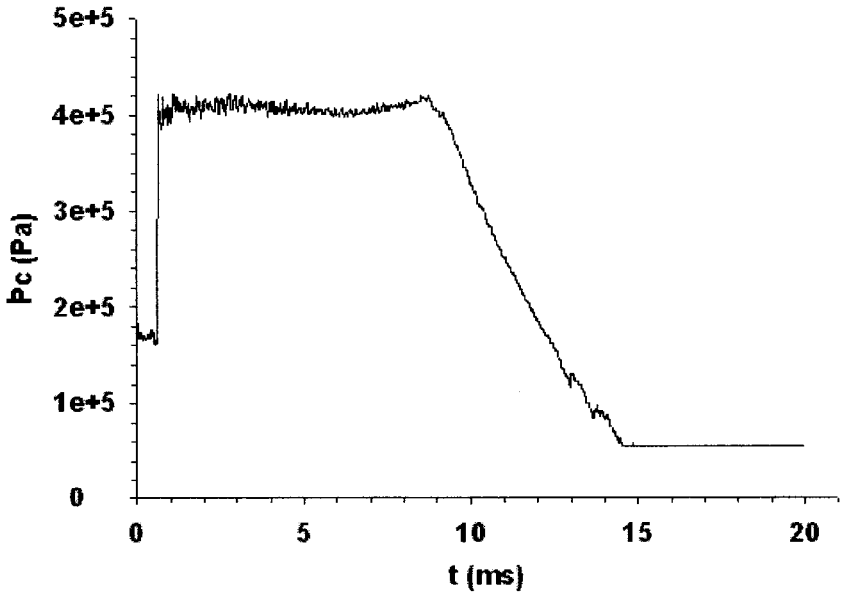

Figure 4.30 Experimental overpressure-time profile for a driven channel pressure of 340 kPa, orifice plate.

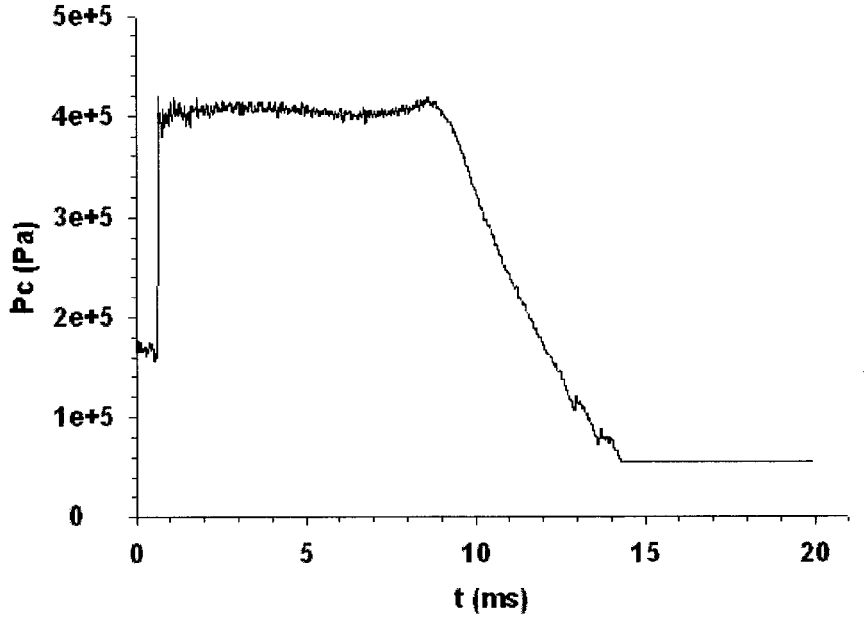

Figure 4.31 Experimental overpressure-time profile for a driven channel pressure of 375 kPa, orifice plate.

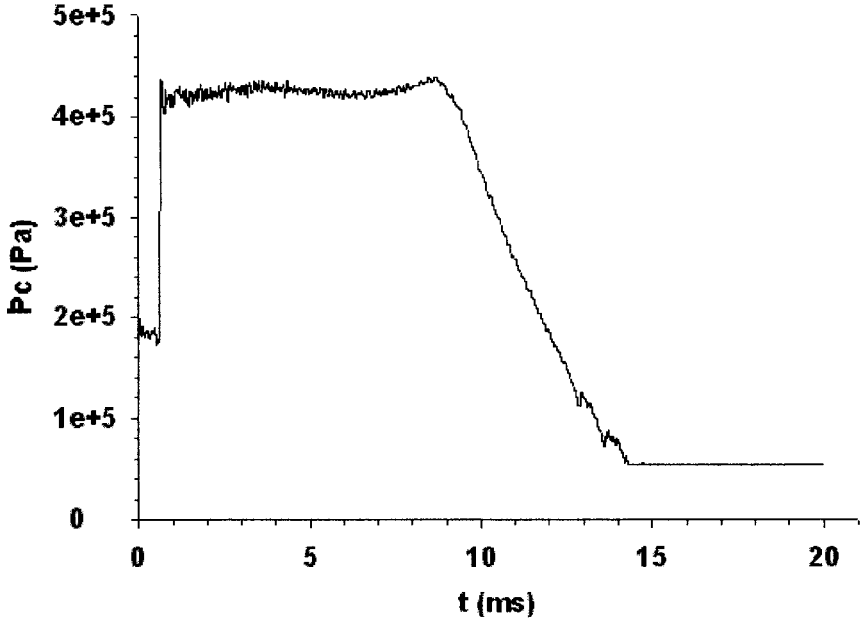

Figure 4.32 Experimental overpressure-time profile for a driven channel pressure of 409 kPa, orifice plate.

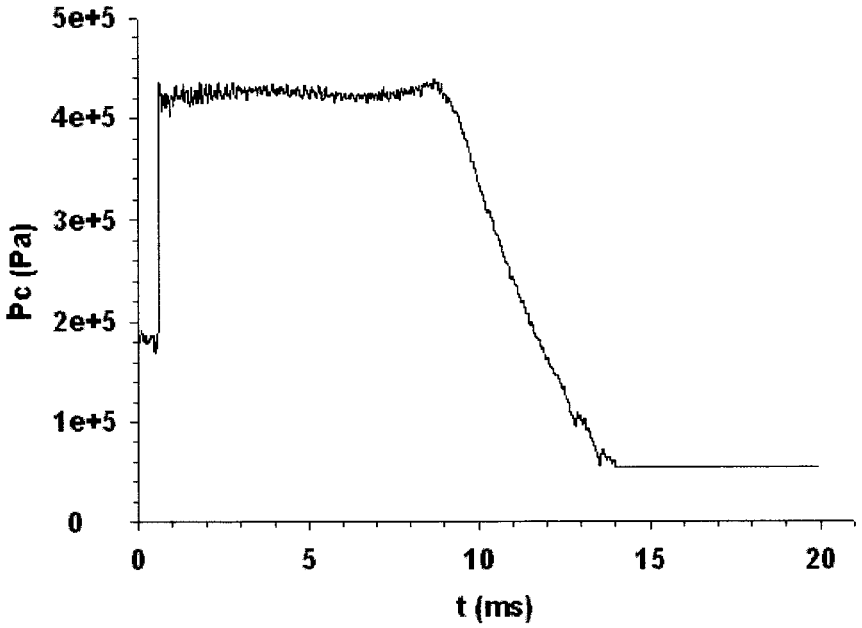

Figure 4.33 Experimental overpressure-time profile for a driven channel pressure of 444 kPa, orifice plate.

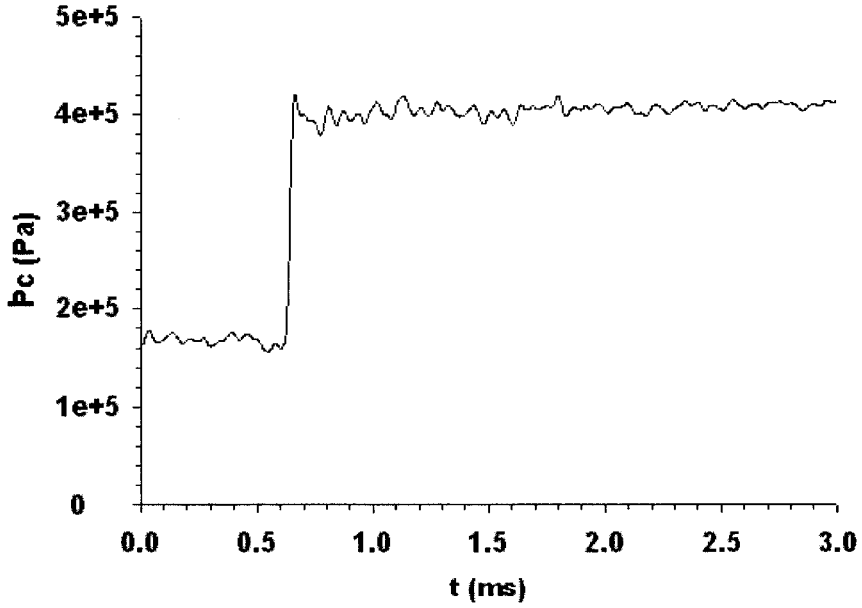

Figure 4.34 Enlarged view of predicted pressure-time profile for a driven channel pressure of 375 kPa, orifice plate.

Fig. 4.34 reveals that for an orifice plate, the reflected shock does not appear to have a substantial initial spike, relative to the case of the reference nozzle (shown in Fig. 4.5). When the incident shock wave arrives at the entrance of an orifice section, the centre portion of the shock wave passes, at first undisturbed, through the orifice, while the outer portion of the shock wave gets reflected from the solid wall.

The resulting difference between the pressures in the front of the solid wall and the open portion of the orifice settles out quickly as the reflected wave reaches quasi-equilibrium. The absence of a ramped conical surface (as in the case for the nozzle convergence) undoubtedly limits the generation of any secondary radial waves, as is also evident from the corresponding FLUENT results shown in Figs. 4.35, 4.36, 4.37, and 4.38.

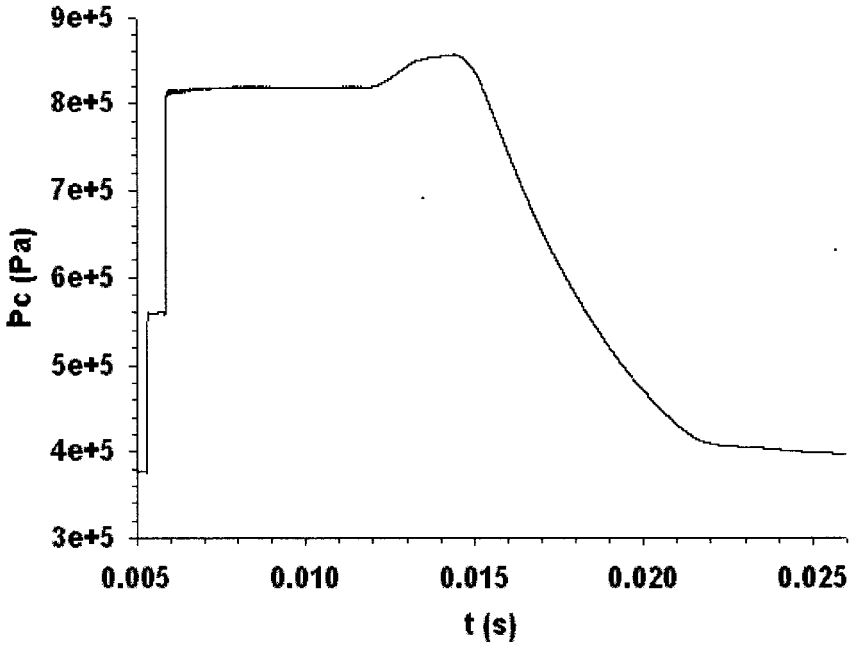

Figure 4.35 Predicted pressure-time profile for a driven channel pressure of 375 kPa, 10 cm upstream of 0°-inclination orifice plate, at the wall of the shock tube.

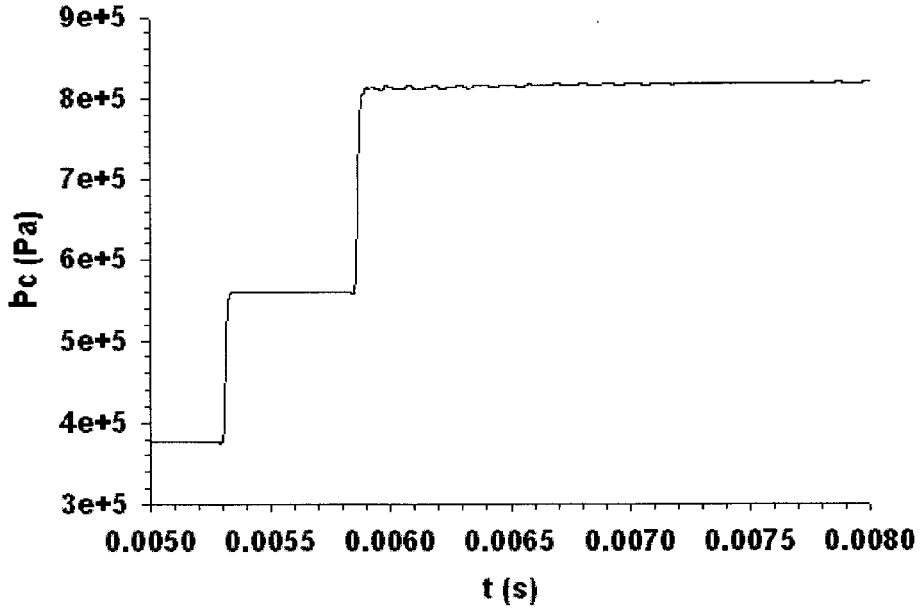

Figure 4.36 Enlarged view of predicted pressure-time profile for a driven channel pressure of 375 kPa, 10 cm upstream of 0° -inclination orifice plate, at the wall of the shock tube.

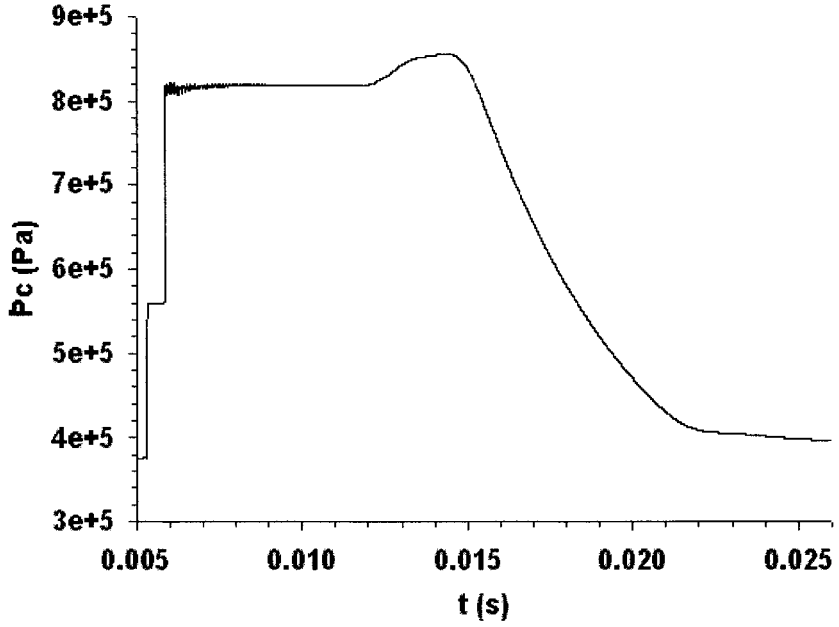

Figure 4.37 Predicted pressure-time profile for a driven channel pressure of 375 kPa, 10 cm upstream of 0° -inclination orifice plate, at the centre axis of the shock tube.

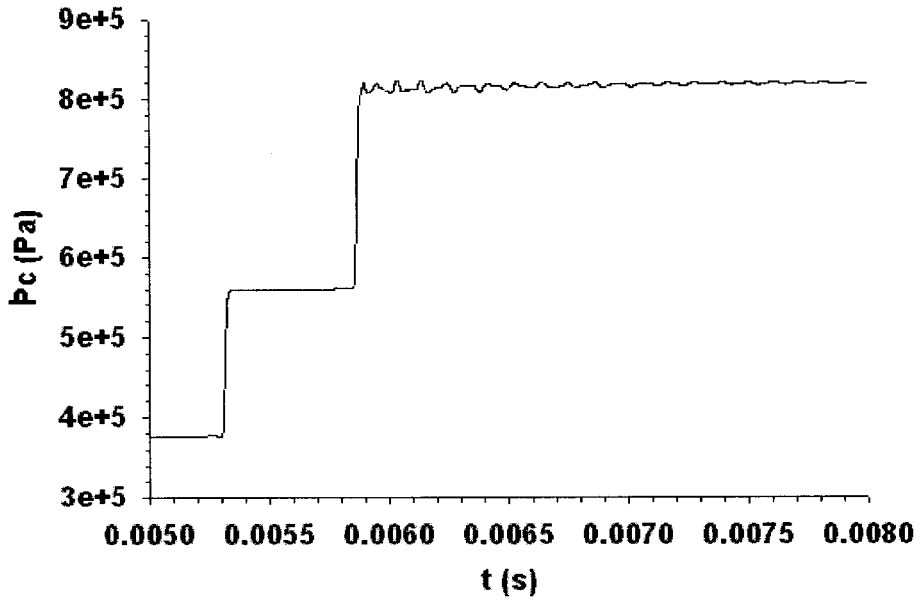

Figure 4.38 Enlarged view of predicted pressure-time profile for a driven channel pressure of 375 kPa, 10 cm upstream of 0° -inclination orifice plate, at the centre axis of the shock tube.

In addition to the 0° -inclination orifice plate, numerical modelling of the 45° -inclination orifice plate is also of interest, so as to identify any potential differences in the radial wave activity occurring in different orifice plate geometries. Numerically predicted pressure-time profiles for a 45° -inclination orifice plate at driven channel pressure of 375 kPa at the wall and at the centre axis of the shock tube are presented in Figs. 4.39, 4.40, 4,41, and 4.42.

Figs. 4.40 and 4.42 display similar pressure profiles as observed in Figs. 4.36 and 4.38. This is not surprising, given that the flow is essentially supersonic in the immediate vicinity downstream of the orifice entrance, thus precluding any upstream-moving disturbance from this region reaching the channel transducer position. The amplitude of the radial waves is higher at the centre axis than at the wall, and the radial waves decay with each reflection in the transverse direction, as is observed in the reference nozzle case.

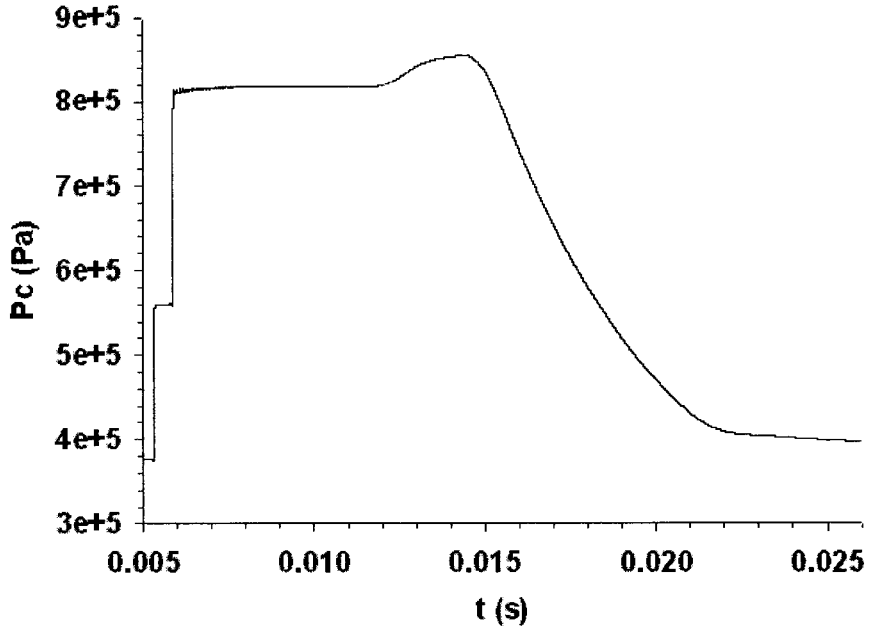

Figure 4.39 Predicted pressure-time profile for a driven channel pressure of 375 kPa, 10 cm upstream of 45° -inclination orifice plate, at the wall of the shock tube.

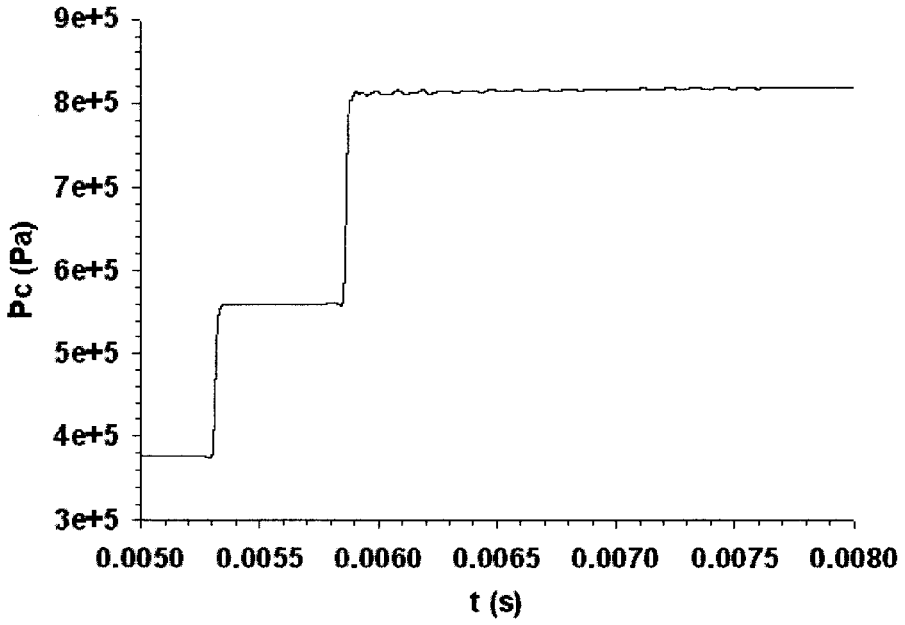

Figure 4.40 Enlarged view of predicted pressure-time profile for a driven channel pressure of 375 kPa, 10 cm upstream of 45° -inclination orifice plate, at the wall of the shock tube.

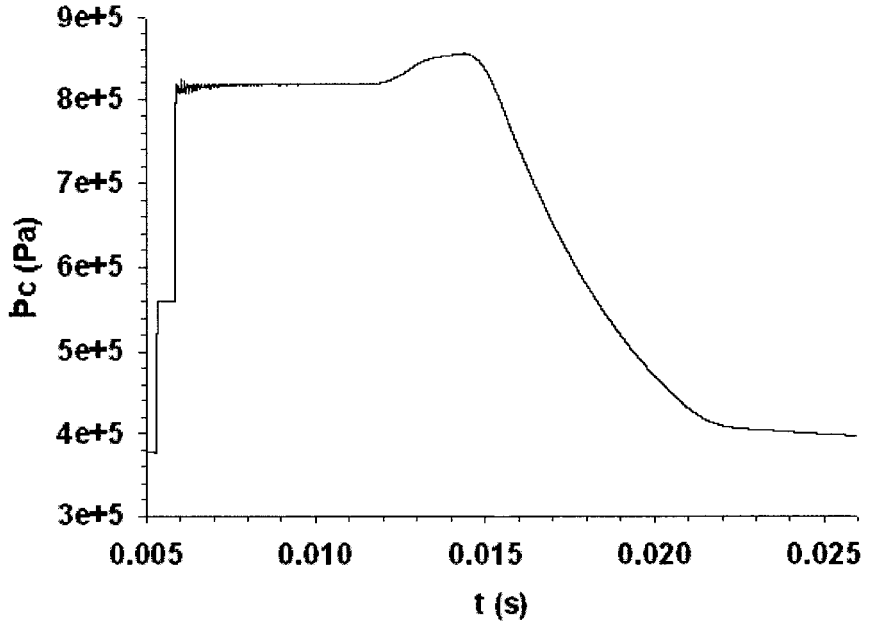

Figure 4.41 Predicted pressure-time profile for a driven channel pressure of 375 kPa, 10 cm upstream of 45° -inclination orifice plate, at the centre axis of the shock tube.

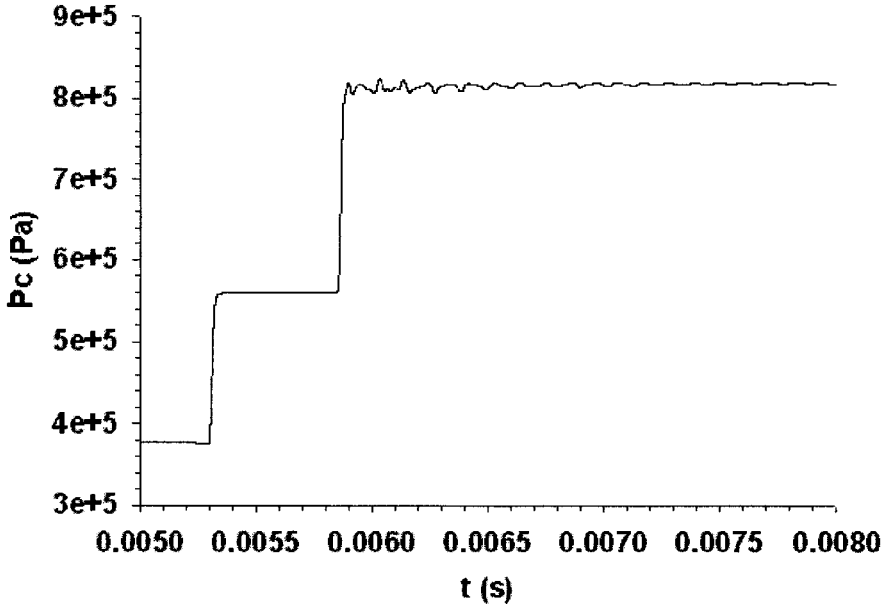

Figure 4.42 Enlarged view of predicted pressure-time profile for a driven channel pressure of 375 kPa, 10 cm upstream of 45° -inclination orifice plate, at the centre axis of the shock tube.

4.4 Numerical Results for C-D Nozzle having 30° and 60° Half-Cone Convergence Angles

In addition to considering different orifice geometries, different geometries of the converging-diverging nozzle are also considered. The variation of the half-cone angles for the nozzle convergence section is of interest. (It should be noted that, in this case, changing the half-cone convergence angle causes the length of the nozzle to change.) Results for 30° and 60° half-cone convergence angles at different axial and transverse locations are illustrated below.

4.4.1 30° Convergence Angle

The numerical results at the wall, 5 cm upstream of the C-D nozzle having a 30° half-cone convergence angle, are presented in Figs. 4.43 and 4.44. The magnitude of the predicted initial pressure spike (see Fig. 4.44) is around 80 kPa relative to the reflected shock's base strength, higher than that observed at the wall, 5 cm upstream of the reference C-D nozzle (see Fig. 4.7). Fig. 4.44 also exhibits prominent higher-order frequencies superimposed on the mean radial wave frequency. The mean radial wave frequency at the wall, 5 cm upstream of the C-D nozzle having a 30° half-cone convergence angle is around 9.2 kHz, marginally higher than that in Fig. 4.7. The radial wave activity has a shorter duration and is weaker at 5 cm upstream of the C-D nozzle having a 30° half-cone convergence angle as compared to the reference C-D nozzle case at the wall for the same axial position.

Figs. 4.45 and 4.46 show the numerical results at the centre axis of the shock tube, 5 cm upstream of the C-D nozzle having a 30° half-cone convergence angle. The magnitude of the predicted initial pressure spike in Fig. 4.46 is of the order of 180 kPa relative to the reflected shock's base strength, higher than that observed at the centre axis for the reference C-D nozzle (see Fig. 4.9). The mean radial wave frequency is around 9.1 kHz, higher than that noted in Fig. 4.9. Other features such as the duration and strength of the radial waves have similar values to that seen in Fig. 4.9.

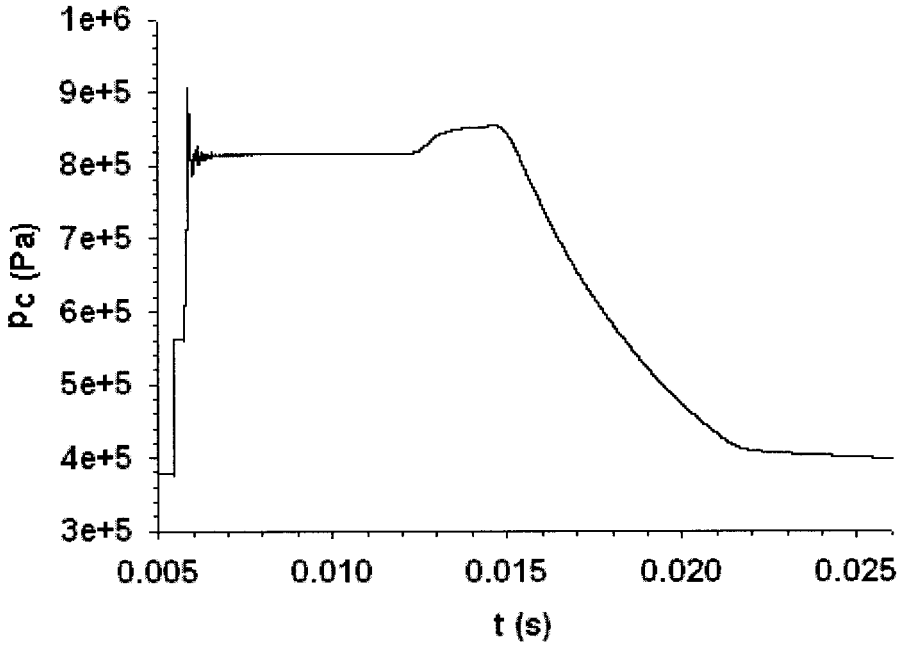

Figure 4.43 Predicted pressure-time profile for a driven channel pressure of 375 kPa, 5 cm upstream of C-D nozzle having a 30° half-cone convergence angle, at the wall of the shock tube.

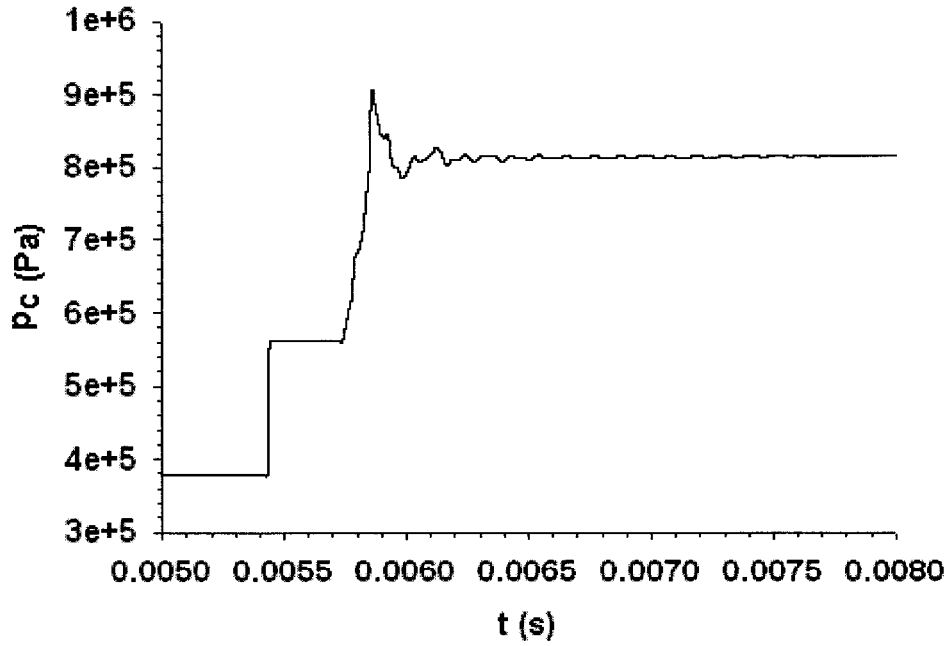

Figure 4.44 Enlarged view of predicted pressure-time profile for a driven channel pressure of 375 kPa, 5 cm upstream of C-D nozzle having a 30° half-cone convergence angle, at the wall of the shock tube.

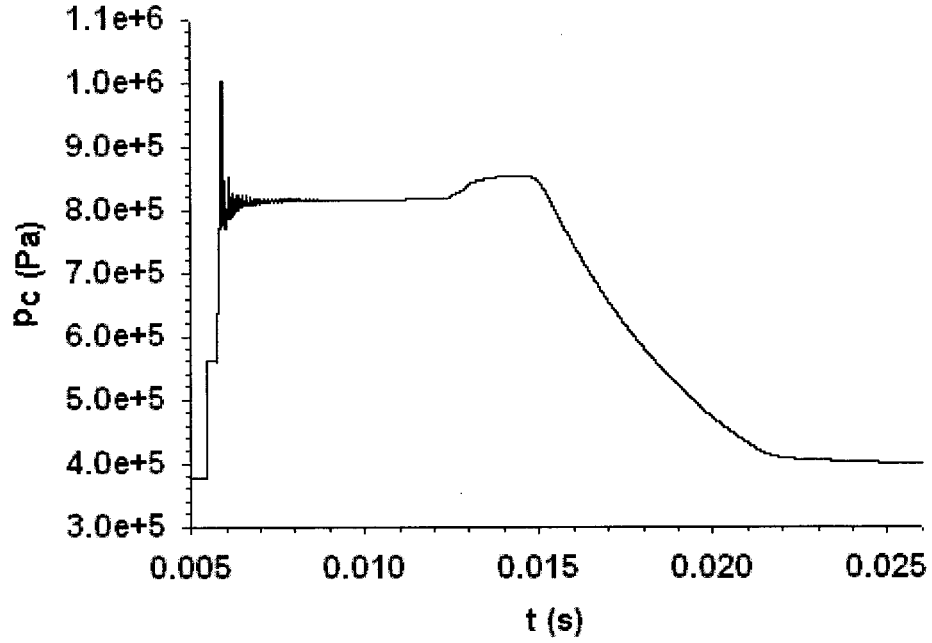

Figure 4.45 Predicted pressure-time profile for a driven channel pressure of 375 kPa, 5 cm upstream of C-D nozzle having a 30° half-cone convergence angle, at the centre axis of the shock tube.

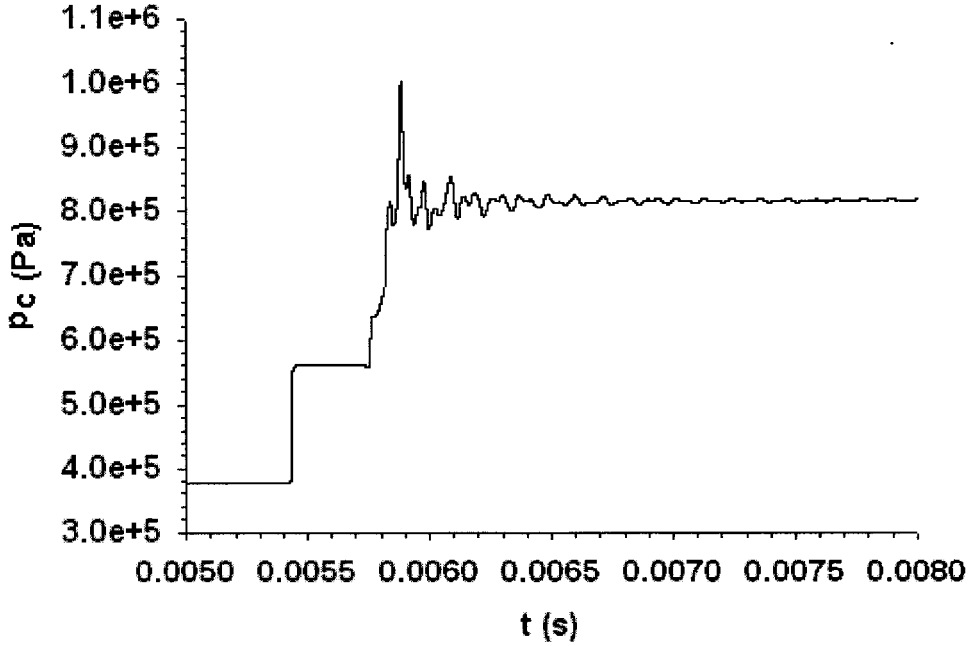

Figure 4.46 Enlarged view of predicted pressure-time profile for a driven channel pressure of 375 kPa, 5 cm upstream of C-D nozzle having a 30° half-cone convergence angle, at the centre axis of the shock tube.

Fig. 4.47 shows the predicted results at the wall, 10 cm upstream of the C-D nozzle having a 30° half-cone convergence angle and the enlarged view is shown in Fig. 4.48.

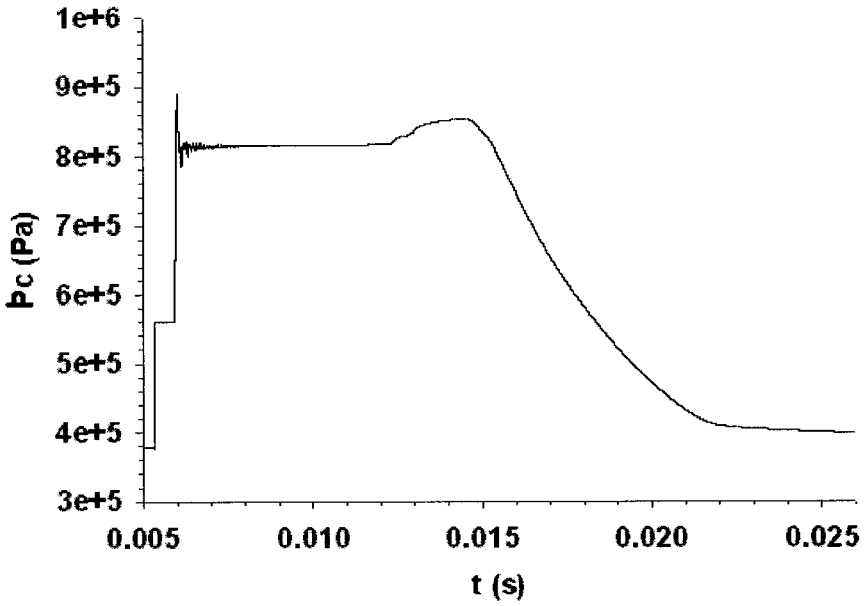

Figure 4.47 Predicted pressure-time profile for a driven channel pressure of 375 kPa, 10 cm upstream of C-D nozzle having a 30° half-cone convergence angle, at the wall of the shock tube.

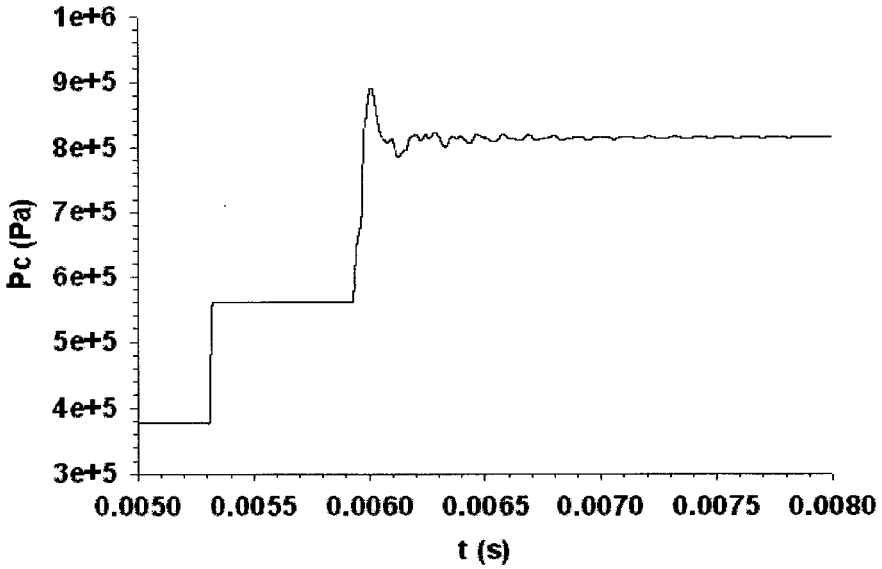

Figure 4.48 Enlarged view of predicted pressure-time profile for a driven channel pressure of 375 kPa, 10 cm upstream of C-D nozzle having a 30° half-cone convergence angle, at the wall of the shock tube.

In Fig. 4.48, the magnitude of the predicted initial pressure spike is similar to the value noted at the wall, 10 cm upstream of the reference C-D nozzle (see Fig. 4.11). The mean radial wave frequency at the wall at 10 cm upstream of the C-D nozzle having a 30° half-cone convergence angle is substantially higher than that at the wall for the reference nozzle case (see Fig. 4.11). The strength of the radial waves is lower in Fig. 4.48 when compared to that in Fig. 4.11; however, the duration of radial wave activity is same in both cases.

The numerical results at the centre axis of the shock tube, 10 cm upstream of the C-D nozzle having 30° half-cone convergence angle, are presented below in Figs. 4.49 and 4.50. For a C-D nozzle having a 30° half-cone convergence angle, the magnitude of the predicted initial pressure spike at the centre axis is substantially higher than that at the wall of the shock tube at the 10-cm position, and relative to the 45° convergence case, as seen in Fig. 4.48 and Fig. 4.50. The strength of secondary oscillations is higher at the centre axis than at the wall, with levels comparable to the 45° predictions. The mean radial wave frequency at 10 cm upstream of a C-D nozzle having a 30° half-cone convergence angle is higher at the wall as compared to that at the centre axis.

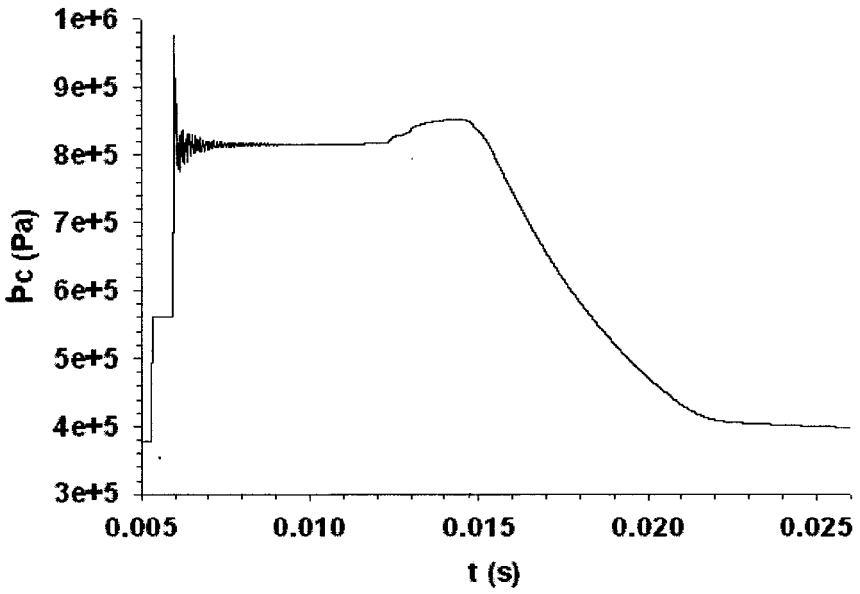

Figure 4.49 Predicted pressure-time profile for a driven channel pressure of 375 kPa, 10 cm upstream of C-D nozzle having a 30° half-cone convergence angle, at the centre axis of the shock tube.

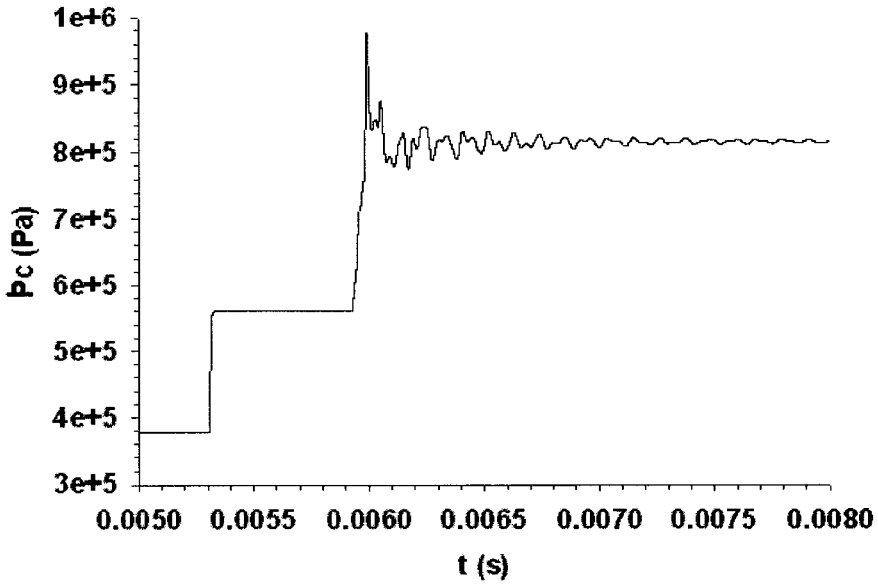

Figure 4.50 Enlarged view of predicted pressure-time profile for a driven channel pressure of 375 kPa, 10 cm upstream of C-D nozzle having a 30° half-cone convergence angle, at the centre axis of the shock tube.

Fig. 4.51 shows the predicted profile at the wall, 15 cm upstream of the C-D nozzle having a 30° half-cone convergence angle and Fig. 4.52 depicts an enlarged view of Fig. 4.51. The magnitude of the predicted initial pressure spike (see Fig. 4.51) is substantially higher than that noted at the wall, 15 cm upstream of the reference C-D nozzle (see Fig. 4.17). The mean radial wave frequency is around 11 kHz, higher than that determined in Fig. 4.17. The duration and strength of the radial waves have similar values in both the cases, as apparent from Figs. 4.17 and 4.52.

The numerical results at the centre axis of the shock tube, 15 cm upstream of the C-D nozzle having a 30° half-cone convergence angle are presented in Figs. 4.53 and 4.54. In Fig. 4.54, the magnitude of the predicted initial pressure spike is higher than that observed at the centre axis, 15 cm upstream of the reference C-D nozzle (see Fig.4.19). Unlike other pressure-time profiles for various axial positions for the reference C-D nozzle as well as for a C-D nozzle having a 30° half-cone convergence angle, this initial pressure spike at the centre axis is not substantially higher when compared to that at the wall. The mean radial wave frequency at the centre axis (see Fig. 4.54) is around 10 kHz,

lower than that determined at the wall (see Fig. 4.52); however, the duration and strength have similar values.

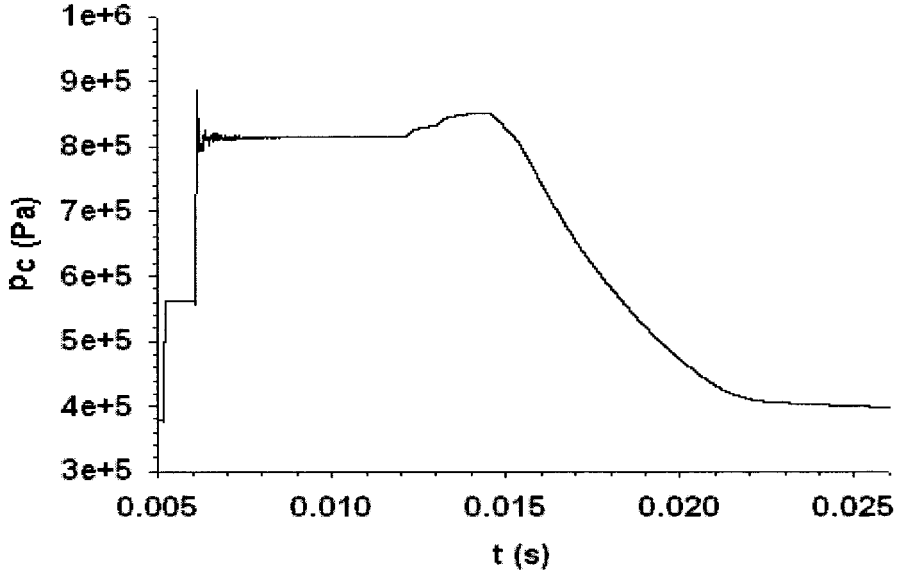

Figure 4.51 Predicted pressure-time profile for a driven channel pressure of 375 kPa, 15 cm upstream of C-D nozzle having a 30° half-cone convergence angle, at the wall of the shock tube.

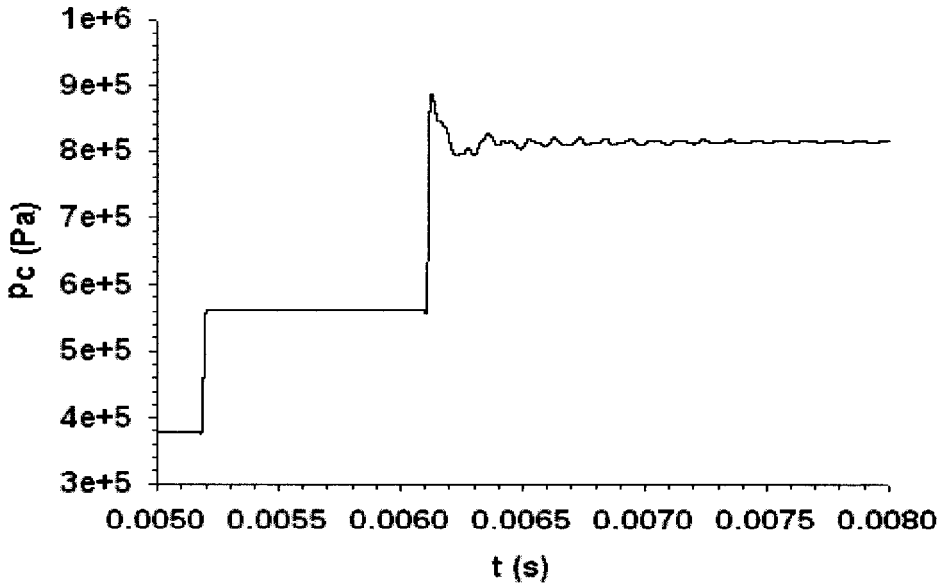

Figure 4.52 Enlarged view of predicted pressure-time profile for a driven channel pressure of 375 kPa, 15 cm upstream of C-D nozzle having a 30° half-cone convergence angle, at the wall of the shock tube.

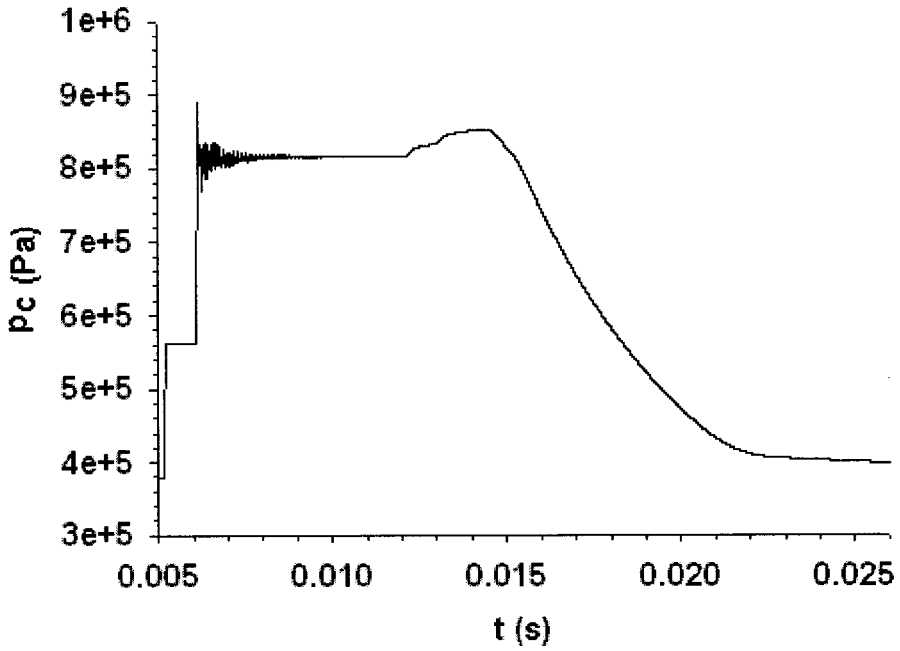

Figure 4.53 Predicted pressure-time profile for a driven channel pressure of 375 kPa, 15 cm upstream of C-D nozzle having a 30° half-cone convergence angle, at the centre axis of the shock tube.

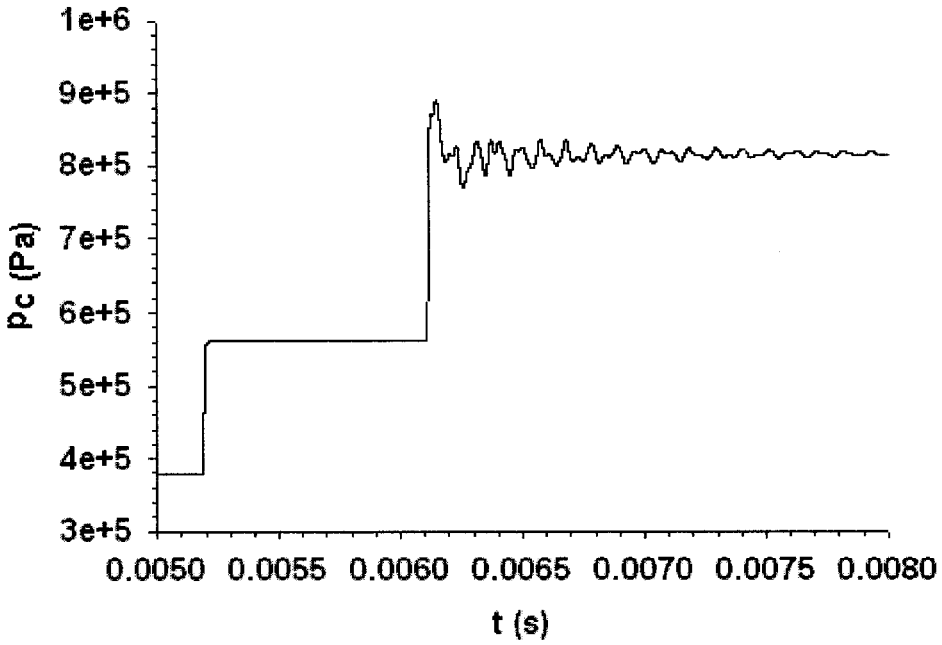

Figure 4.54 Enlarged view of predicted pressure-time profile for a driven channel pressure of 375 kPa, 15 cm upstream of C-D nozzle having a 30° half-cone convergence angle, at the centre axis of the shock tube.

4.4.2 60° Convergence Angle

After modelling a C-D nozzle having a shallower convergence angle (viz., 30° half-cone convergence angle), a C-D nozzle having a steeper convergence angle (viz., 60° half-cone convergence angle) relative to the reference case is also modelled, and the respective pressure-time profiles at different axial and radial locations are presented here.

Numerical results in Figs. 4.55 and 4.56 show the predicted profiles at the wall, 5 cm upstream of the C-D nozzle having a 60° half-cone convergence angle. At the wall, 5 cm upstream of the C-D nozzle having a 60° half-cone convergence angle (see Fig. 4.56), the magnitude of the predicted initial spike is substantially lower than that observed at the wall, 5 cm upstream of the 45° C-D nozzle (see Fig. 4.7). The mean radial wave frequency at the wall, 5 cm upstream of the C-D nozzle having a 60° half-cone convergence angle, is around 10 kHz, significantly higher than that determined at the wall at the corresponding axial location for the 45° C-D nozzle. However, the strength of radial waves at the wall for the 5-cm axial position is stronger in the 60° C-D nozzle case.

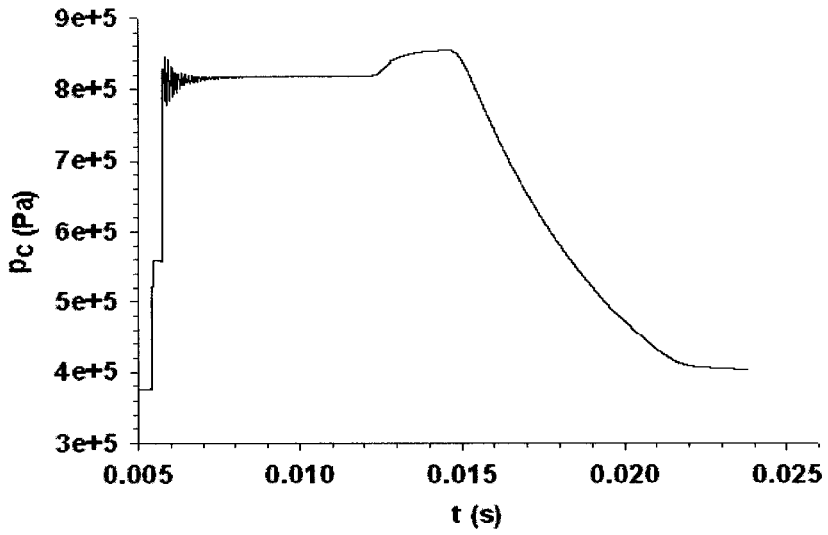

Figure 4.55 Predicted pressure-time profile for a driven channel pressure of 375 kPa, 5 cm upstream of C-D nozzle having a 60° half-cone convergence angle, at the wall of the shock tube.

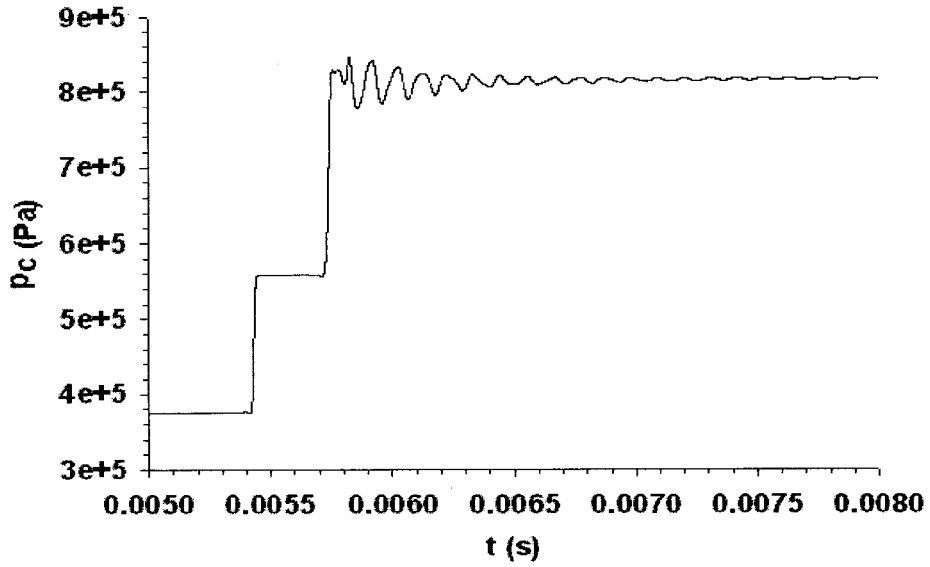

Figure 4.56 Enlarged view of predicted pressure-time profile for a driven channel pressure of 375 kPa, 5 cm upstream of C-D nozzle having a 60° half-cone convergence angle, at the wall of the shock tube.

Fig. 4.57 shows the predicted profile at the centre axis, 5 cm upstream of the C-D nozzle having a 60° half-cone convergence angle and the enlarged view is shown in Fig. 4.58. The magnitude of the predicted initial pressure spike at 5 cm upstream of the C-D nozzle having a 60° half-cone convergence angle, at the centre axis (see Fig. 4.58), is substantially higher than that at the wall (see Fig. 4.56), and is also higher than that noted at the centre axis, 5 cm upstream of the reference C-D nozzle (see Fig. 4.9). The secondary oscillations are stronger at the centre axis in comparison to that at the wall for the 5-cm axial position for a C-D nozzle having a 60° half-cone convergence angle. At 5 cm upstream of the C-D nozzle having a 60° half-cone convergence angle, the mean radial wave frequency is higher at the wall as compared to that at the centre axis.

Figs. 4.59, 4.60, 4.61, and 4.62 show the numerical results at 10 cm upstream of the C-D nozzle having a 60° half-cone convergence angle. At the wall, 10 cm upstream of the nozzle the magnitude of the initial pressure spike (see Fig. 4.60) is similar to the value obtained at the wall, 10 cm upstream of the reference C-D nozzle (see Fig. 4.11). Also, the strength of secondary oscillations and the mean radial wave frequency are approximately the same in both the cases.

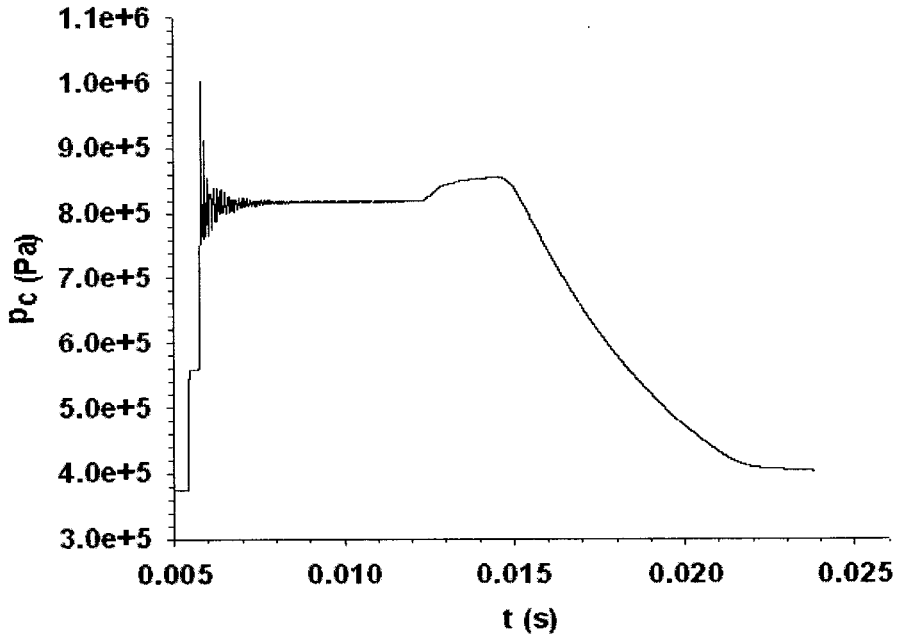

Figure 4.57 Predicted pressure-time profile for a driven channel pressure of 375 kPa, 5 cm upstream of C-D nozzle having a 60° half-cone convergence angle, at the centre axis of the shock tube.

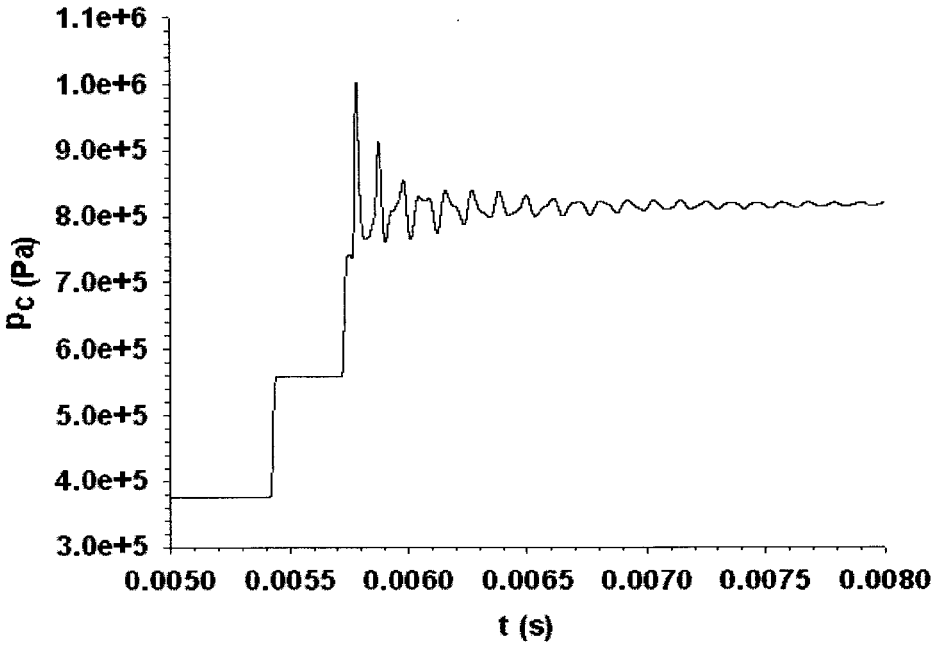

Figure 4.58 Enlarged view of predicted pressure-time profile for a driven channel pressure of 375 kPa, 5 cm upstream of C-D nozzle having a 60° half-cone convergence angle, at the centre axis of the shock tube.

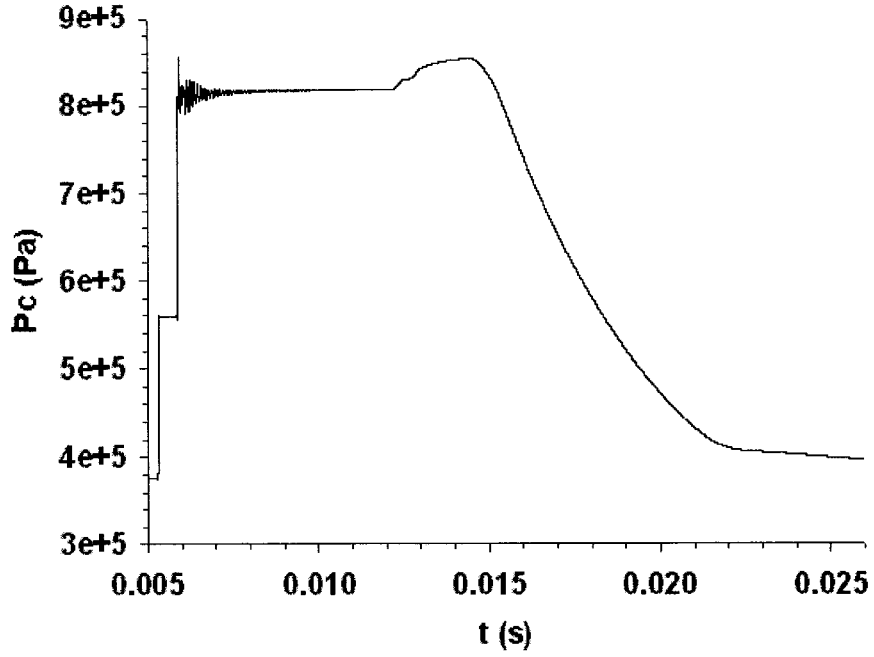

Figure 4.59 Predicted pressure-time profile for a driven channel pressure of 375 kPa, 10 cm upstream of C-D nozzle having a 60° half-cone convergence angle, at the wall of the shock tube.

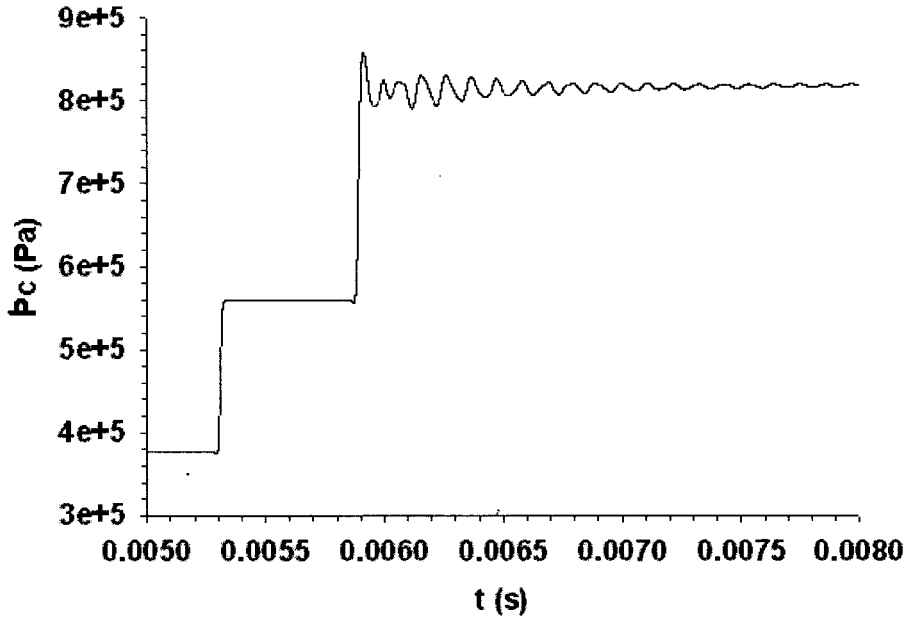

Figure 4.60 Enlarged view of predicted pressure-time profile for a driven channel pressure of 375 kPa, 10 cm upstream of C-D nozzle having a 60° half-cone convergence angle, at the wall of the shock tube.

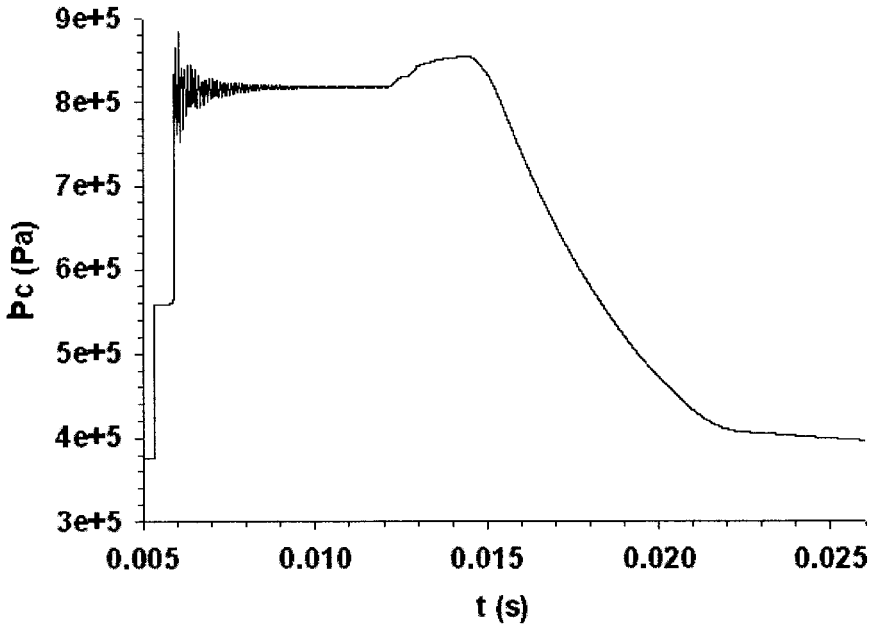

Figure 4.61 Predicted pressure-time profile for a driven channel pressure of 375 kPa, 10 cm upstream of C-D nozzle having a 60° half-cone convergence angle, at the centre axis of the shock tube.

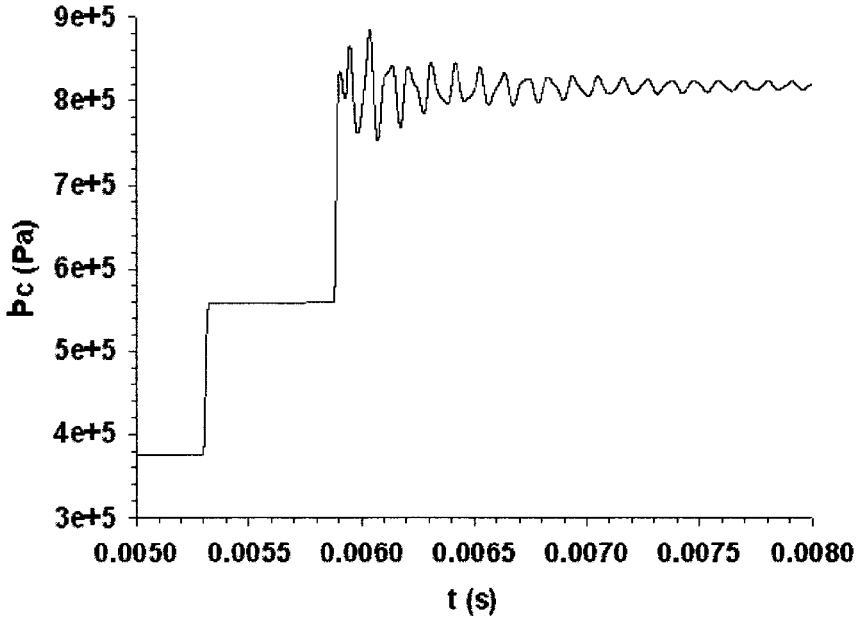

Figure 4.62 Enlarged view of predicted pressure-time profile for a driven channel pressure of 375 kPa, 10 cm upstream of C-D nozzle having a 60° half-cone convergence angle, at the centre axis of the shock tube.

At the centre axis of the shock tube, 10 cm upstream of a C-D nozzle having a 60° half-cone convergence angle (see Fig. 4.62), the magnitude of the predicted initial pressure spike is lower than that at the centre axis, 10-cm position, relative to the 30° case (see Fig. 4.50). On the other hand, the initial spike, and the subsequent oscillations, is stronger here in comparison to the 45° case, at the centre axis (see Fig. 4.13). At the centre axis of the shock tube, a C-D nozzle having a 60° half-cone convergence angle produces a longer duration of radial wave activity at the measurement location, as compared to the other two C-D nozzle geometries.

Figs. 4.63, 4.64, 4.65, and 4.66 show the numerical results at the wall, 15 cm upstream of the C-D nozzle having a 60° half-cone convergence angle.

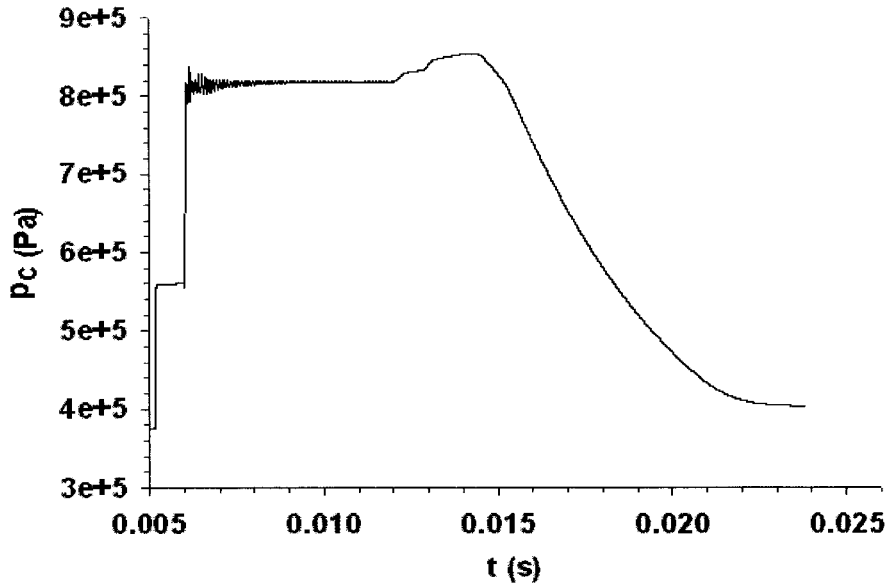

Figure 4.63 Predicted pressure-time profile for a driven channel pressure of 375 kPa, 15 cm upstream of C-D nozzle having a 60° half-cone convergence angle, at the wall of the shock tube.

At the wall, 15 cm upstream of the nozzle (see Fig. 4.64), the magnitude of the predicted initial pressure spike is lower to that at the wall at 15 cm upstream of the reference C-D nozzle (see Fig. 4.17). However, the strength and the mean frequency of the radial waves are somewhat similar in both cases.

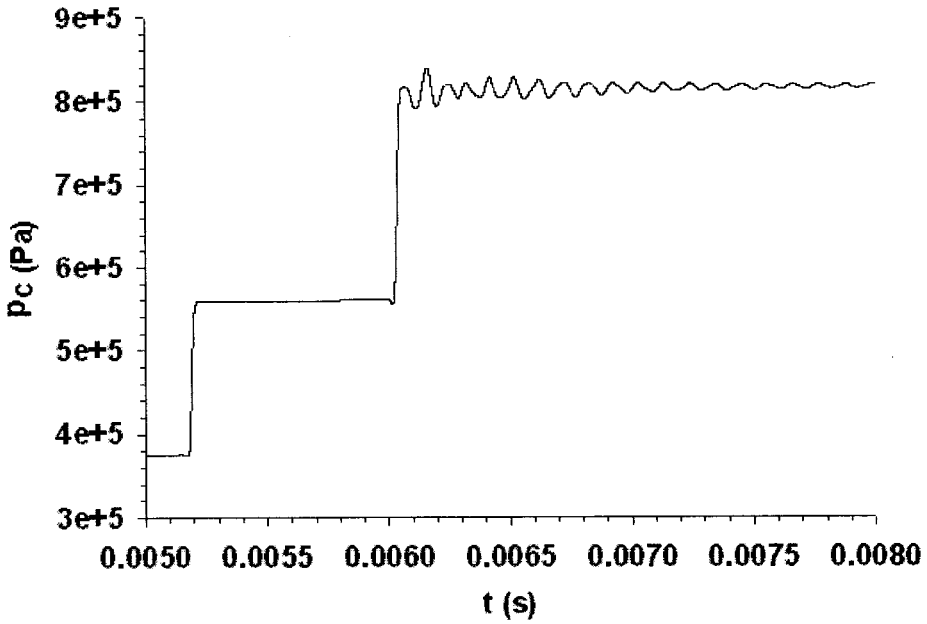

Figure 4.64 Enlarged view of predicted pressure-time profile for a driven channel pressure of 375 kPa, 15 cm upstream of C-D nozzle having a 60° half-cone convergence angle, at the wall of the shock tube.

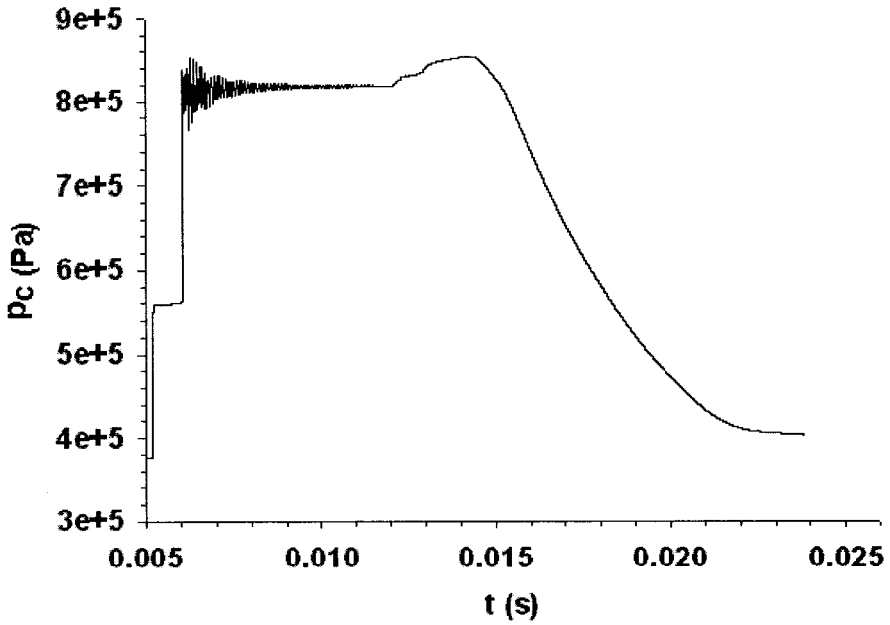

Figure 4.65 Predicted pressure-time profile for a driven channel pressure of 375 kPa, 15 cm upstream of C-D nozzle having a 60° half-cone convergence angle, at the centre axis of the shock tube.

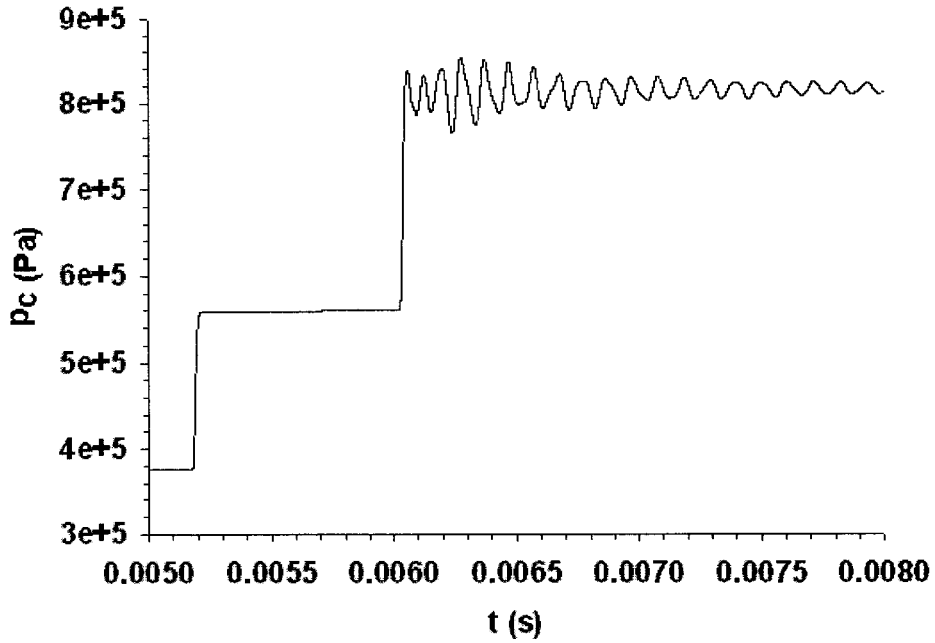

Figure 4.66 Enlarged view of predicted pressure-time profile for a driven channel pressure of 375 kPa, 15 cm upstream of C-D nozzle having a 60° half-cone convergence angle, at the centre axis of the shock tube.

At the centre axis, 15 cm upstream of the C-D nozzle having a 60° half-cone convergence angle (see Fig. 4.66), the magnitude of the predicted initial pressure spike is substantially lower when compared with various other numerically predicted pressure-time profiles at the centre axis and different axial positions for different nozzle geometries; however, the strength of the secondary oscillations and the mean radial wave frequency are comparable.

A comparison of various predicted pressure-time profiles for the different C-D nozzle geometries (discussed in this Chapter) reveals that the radial waves are stronger and of longer duration for the C-D nozzle having a 60° half-cone convergence angle than for the C-D nozzles having 30° and 45° half-cone convergence angles. At the wall, one can observe corresponding trends. Axial position, as well as radial position, undoubtedly plays a role in the local pressure profile behaviour that is observed.

The various experimental and numerical pressure-time profiles, at different driven channel pressures and at different axial and radial positions, tend to confirm the

appearance of substantial radial wave activity following the initial incidence of the normal shock wave on the convergence region of the nozzle. For an SRM experiencing axial combustion instability symptoms, the transient radial wave action superimposed on the main reflected wave front of a traversing axial compression wave could potentially instigate an augmentation of the local propellant burning in the aft port region, which in turn might act to reinforce the axial wave, possibly leading to unsafe operation of the SRM.

Earlier work done by various researchers has identified different potential combustion-related driving mechanisms (a few of which are discussed in Section 1.1) for sustained limited-amplitude pressure waves inside the combustion chamber of an SRM that might be supported or enhanced by the radial wave activity observed in this study. For example, if the radial wave frequency is at or near (or a harmonic of) the natural frequency of the local propellant/casing or the propellant's combustion response function, resonance could occur, potentially leading to the further growth of axial waves inside the combustion chamber of an SRM, unless a countering mechanism, such as one involving particles in the flow, is used to inhibit transverse wave development.

Chapter 5 Summary, Conclusions and Recommendations

5.1 Summary and Conclusions

This thesis deals with one of the primary symptoms of non-linear axial combustion instability in SRMs, viz., a limited-amplitude axial (compression) wave traversing back and forth along the combustion chamber of an SRM. On the basis of previous experimental observation of pressure-time profiles in the combustion chamber and propellant base burning rates, a potential driving mechanism for this symptom, which is gasdynamic in nature, involving reinforcement of a reflected shock wave in the nozzle convergence region of an SRM, was suggested. The particular mechanism in question was the main focus of the current investigation. Specifically, experiments and numerical simulations were employed to examine the various aspects surrounding the interaction of an incident travelling normal shock wave on the exhaust nozzle of an SRM.

For the experimental component of this study, a customized shock tube apparatus, with room-temperature air as the working fluid, was developed. A two-dimensional axisymmetric model of the shock tube was developed for computational fluid dynamics simulations. Various experimental and numerical pressure-time profiles were presented in Chapter 4. Assessment of these profiles was done by means of the magnitude of the initial pressure spike, the mean radial wave frequency, and the strength and duration of the radial waves generated in each case.

For the reference C-D nozzle (i.e., the nozzle with a half-cone convergence angle of 45°), at each axial position, the magnitude of the initial pressure spike and the strength of the radial waves are higher at the centre axis than that at the wall of the shock tube. The mean radial wave frequency at the wall increases as the axial position increases from 5 cm upstream to 15 cm upstream of the nozzle. Also, the mean radial wave frequency at the centre axis of the shock tube decreases as the axial position increases from 5 cm upstream to 15 cm upstream of the nozzle; however, the value is higher for the 15-cm axial position than it is for the 10-cm position. Generally, as expected, the radial waves strengthen as one moves radially from the wall to the centre axis of the shock tube. No generalization can be made for the observed mean radial wave frequency.

The predicted inviscid flow pressure-time profiles obtained for the reference C-D nozzle imply that for a relatively low pressure situation (as in the present study), viscous effects on the pressure wave development are negligible; however, there is the possibility that these effects might be more significant in a higher pressure scenario.

The occurrence of pressure "BUMPS", designated as BUMP A and BUMP B in the various experimental and numerical pressure-time profiles, was explained by means of estimates of the times of arrival of compression waves at the transducer location. The calculations establish that BUMP A was formed by (new) downstream-moving compression waves arising due to the collision between the upstream-moving reflected shock wave and the downstream-moving contact surface; BUMP B was caused by the reflected waves generated from the reflection of these (new) compression waves from the nozzle convergence region.

The various experimental and numerical pressure-time profiles for different orifice plate geometries do not exhibit substantial initial pressure spikes as compared to the reference C-D nozzle case; moreover, the strength of the radial waves is low. The absence of a ramped conical surface (as in the case of the C-D nozzle) undoubtedly limits the generation of radial waves. However, the radial waves are stronger at the centre axis than at the wall of the shock tube, as in the case of the reference C-D nozzle.

Similar to the reference nozzle case, the C-D nozzle having 30° and 60° half-cone convergence angles exhibit much the same trends for the initial pressure spike and the strength of the radial waves; however, the values are different. For each axial position, the initial pressure spike is higher at the centre axis than at the wall of the shock tube, and the radial waves strengthen as one moves radially from the wall to the centre axis of the shock tube. Again, no generalization can be made with regard to the mean radial wave frequency for these two C-D nozzle geometries.

A comparison of various predicted pressure-time profiles for the different C-D nozzle geometries in the present study reveals that the radial waves are stronger and of longer duration for the C-D nozzle having a 60° half-cone convergence angle (as compared to 30° and 45°). Also, a comparison of the experimental and numerical results for the reference C-D nozzle (having a 45° half-cone convergence angle) suggest that the

magnitude of the initial pressure spike depends on the driven channel pressure, increasing as the latter increases, but at a decreasing rate.

The various experimental and numerical pressure-time profiles, at different driven channel pressures and at different axial and radial positions, confirm the appearance of substantial radial wave activity following the initial incidence of the normal shock wave on the convergence region of the nozzle. In the analogous case of an SRM encountering non-linear axial combustion instability, the transient radial wave action superimposed on the main reflected wave front of a traversing axial compression wave could potentially instigate an augmentation of the local propellant burning in the aft port region, which in turn might act to reinforce the axial wave, possibly leading to nonsteady combustion behaviour inside the combustion chamber of an SRM. Also, the different potential combustion-related driving mechanisms might be supported or enhanced by the radial wave activity observed in the present study. For example, if the radial wave frequency is at or near the natural frequency of the local propellant/casing or the propellant's combustion response function, resonance will occur, likely leading to the growth of axial waves inside the combustion chamber of an SRM and unsafe SRM operation, unless a countering mechanism, such as one involving particles in the flow, is used to inhibit transverse wave development.

5.2 Recommendations

In order to more closely emulate actual SRM conditions, it is recommended that the shock tube apparatus be operated at higher channel pressures in a future study. Higher pressure air, or various combinations of monatomic and diatomic gases, could be used in the driver and driven channels of the shock tube, if an adequate gas supply is available for the test duration. Such a study would entail utilizing a pressure transducer having a higher operating range and would depend on the structural limits of the experimental apparatus (which may require substantial strengthening). Moreover, the present work could be expanded to investigate the reflected shock wave interaction with the head-end of an SRM. The effect of increasing or decreasing the gap (axially) between the head-end

wall and the end-face of the propellant grain would be one factor of potential interest in future work.

REFERENCES

1. Culick, F.E.C., *"Combustion Instabilities: Mating Dance of Chemical, Combustion, and Combustor Dynamics,"* 36th AIAA/ASME/SAE/ASEE Joint Propulsion Conference, AIAA Paper No. 2000-3178, Huntsville, July 16-19, 2000.

2. Kuo, K.K., and Summerfield, M. (ed.), *"Fundamentals of Solid-Propellant Combustion,"* Progress in Astronautics and Aeronautics, Vol. 90, AIAA Publications, 1984.

3. Greatrix, D.R., and Harris, P.G., *"Structural Vibration Considerations for Solid Rocket Internal Ballistics Modelling,"* 36th AIAA/ASME/SAE/ASEE Joint Propulsion Conference, AIAA Paper No. 2000-3804, Huntsville, July 17-19, 2000.

4. Harris, P.G., Wong, F.C., and de Champlain, A., *"The Influence of Structural Vibrations on Pulse-Triggered Nonlinear Instability in Solid Rocket Motors: An Experimental Study,"* 32nd AIAA/ASME/SAE/ASEE Joint Propulsion Conference, AIAA Paper No. 96-3250, Florida, July 1-3, 1996.

5. Greatrix, D.R., *"Combined Structural Oscillation Effects on Solid Rocket Internal Ballistics,"* 35th AIAA/ASME/SAE/ASEE Joint Propulsion Conference, AIAA Paper No. 99-2509, Los Angeles, June 20-24, 1999.

6. Karnesky, A.L., and Colucci, S.E., *"Recent Occurrences of Combustion Instability in Solid Rocket Motors,"* Journal of Spacecraft and Rockets, Vol. 12, No. 1, January 1975, pp. 33-38.

7. Greatrix, D.R., *"Structural Vibration and Solid Rocket Combustion Instability,"* Canadian Aeronautics and Space Journal, Vol. 44, No. 1, March 1998, pp. 9-24.

8. Blomshield, F.S., and Beiter, C.A., *"Nonlinear Stability Testing and Pulsing of Full Scale Tactical Motors,"* 27th AIAA/ASME/SAE/ASEE Joint Propulsion Conference, AIAA Paper No. 91-1953, Sacramento, June 22-26, 1991.

9. Greatrix, D.R., *"Numerical Study of Axial Motor Oscillation Effects on Solid Rocket Internal Ballistics,"* Canadian Aeronautics and Space Journal, Vol. 40, No. 4, December 1994, pp. 178-186.

10. Solanki, N., Greatrix, D.R., Gottlieb, J.J., *"Externally Generated Pressure Pulse in Rocket Chamber,"* Canadian Aeronautics and Space Journal, Vol. 47, No. 2, March 2001, pp. 345-355.

11. Solanki, N., Greatrix, D.R., and Gottlieb, J.J., *"External Pulse Effects on Solid Rocket Internal Ballistics,"* 36th AIAA/ASME/SAE/ASEE Joint Propulsion Conference, AIAA Paper No. 2000-3188, Huntsville, July 17-19, 2000.

12. Brownlee, W.G., *"Nonlinear Axial Combustion Instability in Solid Propellant Motors,"* AIAA Journal, Vol. 2, No. 2, February 1964, pp. 275-284.

13. Harrje, D.T., *"Liquid Propellant Rocket Combustion Instability,"* National Aeronautics and Space Administration, NASA SP-194, Washington, D.C., 1972.

14. Greatrix, D.R., *"Axial Motor Vibration and Associated Internal Ballistics,"* 33rd AIAA/ASME/SAE/ASEE Joint Propulsion Conference, AIAA Paper No. 97-3337, Seattle, July 7-9, 1997.

15. Blomshield, F.S. and Stalnaker, R.A., *"Pulsed Motor Firing: Pulse Amplitude, Formulation, and Enhanced Instrumentation,"* 34th AIAA/ASME/SAE/ASEE Joint Propulsion Conference, AIAA Paper No. 98-3557, Cleveland, July 12-15, 1998.

16. Baum, J.D., Levine, J.N., and Lovine, R.L., *"Pulsed Instability in Rocket Motors: A Comparison Between Predictions and Experiments,"* Journal of Propulsion and Power, Vol. 4, No. 4, July-Aug., 1988, pp. 308-316.

17. Price, E.W., *"Review of Experimental Research on Combustion Instability of Solid Propellants,"* Progress in Astronautics & Aeronautics, Vol. 1, AIAA Publications, 1960.

18. Gottlieb, J.J., and Greatrix, D.R., *"Numerical Study of the Effects of Longitudinal Acceleration on Solid Rocket Motor Internal Ballistics,"* Journal of Fluids Engineering (ASME), Vol. 114, No. 3, September 1992, pp. 404-410.

19. *"Solid Propellant Selection and Characterization,"* National Aeronautics and Space Administration NASA SP-8064, Washington, D.C., 1971.

20. Levine, J.D., and Baum, J.D., *"Modeling of Nonlinear Combustion Instability in Solid Propellant Rocket Motors,"* Nineteenth International Symposium on Combustion, pp. 769-776, 1982.

21. Greatrix, D.R., *"Transverse Vibration and Rocket Combustor Internal Ballistics,"* 33rd AIAA/ASME/SAE/ASEE Joint Propulsion Conference, AIAA Paper No. 97-3338, Seattle, July 7-9, 1997.

22. Yang, V., Brill, T.B., and Ren, W.Z. (ed.), *"Solid Propellant Chemistry, Combustion, and Motor Interior Ballistics,"* Progress in Astronautics and Aeronautics, Vol. 185, AIAA Publications, 2000.

23. Hugget, C., Bartley, C.E., and Mills, M.M., *Solid Propellant Rockets*, Princeton University Press, New Jersey, 1960.

24. Shafer, J.I., *Solid Rocket Propulsion*, John Wiley & Sons, Inc., New York, 1939.

25. Sutton, G.P., *Rocket Propulsion Elements*, 6th ed., John Wiley & Sons, Inc., New York, 1992.

26. Glass, I.I., *"Shock Tubes,"* Proceedings of the Seventh International Shock Tube Symposium, pp. 751-759, 1969.

27. Ben-Dor, G., Igra, O., and Elperin, T., *Handbook of Shock Waves: Theoretical, Experimental, and Numerical Techniques,* Vol. 1, Academic Press, San Diego, 2001.

28. Anderson, J.D.Jr., *Modern Compressible Flow with Historical Perspective*, 2nd ed., McGraw-Hill Publishing Company, U.S.A., 1990.

29. Zucrow, M.J., Hoffman, J.D., *Gas Dynamics Volume 1,"* John Wiley & Sons, Inc., New York, 1976.

30. Liepmann, H.W., Roshko, A., *Elements of Gasdynamics,* John Wiley & Sons, Inc., New York, 1957.

31. John, J.E.A., *Gas Dynamics,* 2nd ed., ALLYN AND BACON, INC., Massachusetts, 1933.

32. Anthoine, J., Buchlin, J-M., and Guery, J-F., *"Experimental and Numerical Investigations of Nozzle Geometry Effect on the Instabilities in Solid Propellant Boosters,"* 36th AIAA/ASME/SAE/ASEE Joint Propulsion Conference, AIAA Paper No. 2000-3560, Huntsville, July 17-19, 2000.

33. *"Pressure Catalog,"* by Pressure and Force Sensors (PFS) Division, PCB PIEZOELECTRONICS Inc., Printed in U.S.A., 1998.

34. *"WaveBook User's Manual,"* by IOtech, Inc., Printed in U.S.A., 1999.

35. *"FLUENT User's Manual,"* by Fluent, Inc., Lebanon, 2001.

Appendix A PROCEDURES FOR EXPERIMENTS

Procedure 1:

Testing Procedure for Data Acquisition Equipment

Initially, before the data acquisition equipment was installed on the shock tube apparatus, it was tested in the Propulsion Research Facility (PRF at QE-128B, Ryerson University) to gain familiarity with the use of the data acquisition system (i.e., WaveBook) and the process of saving the data. The testing proved to be useful; all the parameters to be inputted in the data acquisition software (i.e., WaveView) were known in advance. A step-by-step testing procedure is given below:

1. Turn "ON" the toggle valve connected to the compressed air supply.
2. Adjust the pressure regulator at some suitable value like 10 psig to achieve pressure calibration. One may turn the regulator in clockwise direction to increase the pressure and vice-versa.
3. Attach the pressure transducer to the air supply coming from the compressor.
4. Connect the transducer output to in-line charge amplifier.
5. Connect the output of charge amplifier to the input "XDRC" of sensor signal conditioner.
6. Connect the output to oscilloscope or high-speed data acquisition. A block diagram showing all these connections is shown in Fig. A.1.
7. Turn "ON" the sensor signal conditioner.
8. Switch "ON" the computer.
9. Switch "ON" the WaveBook.
10. Double click the WaveView icon on the desktop.
11. The WaveView Configuration window appears which provides information about the various channels, etc.
12. In order to begin acquiring data with WaveView, turn "ON" only those channels that have signal connections.

    This can be done by:

a. Double click on the channel's "ON/OFF" cell to select the proper status.
b. Click once on the channel's "ON/OFF" cell, then select "ON" or "OFF" from the list box above the spreadsheet. In our case, we have only one channel working, i.e., CH01.

13. Select the appropriate parameters for each channel.
14. Select Acquisition Configuration from the view pull down menu. When the acquisition configuration window is displayed, enter values for pre-trigger and post-trigger (scans or time periods) as desired. The time base for the acquisition can be set to frequency or period. The desired trigger source and parameters are selected in the trigger selection box.

The various set-up values for the acquisition configuration window are as follows:

DURATION:

1. Pre-trigger: 5 Scans
2. Post-trigger: 10,000 Scans
3. Convection: Scans

RATE:

1. Internal
2. Pre-trigger: 20 kHz
3. Post-trigger: 500 kHz
4. Convection: Frequency

TRIGGERING TYPE: Channel 1 Analog

EDGE: Rising

THRESHOLD: 0.1 V

15. Make sure that all the acquisition configuration settings are correct.

16. Click on "SCOPE" located in the menu bar. A WaveView scope window appears which enables to read data from WaveBook.
17. The initial readings that appear on the WaveView scope window are as follows:
    a. Status: Idle
    b. Scans: 0 / 0% Complete
    c. Scans in View: 10
    d. Pre-trigger Time Base: 25.000 ms/div
    e. Post-trigger Time Base: 1.000 ms/div
18. Click the arm button (Green colour) from the Menu Bar.

    Now, the scope window reads:
    a. Status: Waiting for Trigger
    b. Scans: 5 / 0% Complete
    c. Scans in View: 0
19. After clicking the arm, look at the status. It should read "WAITING FOR TRIGGER". At this time supply a manual trigger from air supply.

    Now, the scope window reads:
    a. Status: Idle
    b. Scans: 10,005 / 100% Complete
    c. Scans in view: 10,000
    d. Pre-trigger Time Base: 25.000 ms/div
    e. Post-trigger Time Base: 1.000 ms/div
20. After a manual trigger is given, a waveform appears in the WaveView scope window.
21. Save this waveform by clicking on the File Menu, then click on "SAVE DATA FILES AS". A dialog box will open asking for the filename. Give any filename with ". TXT" as an extension. Click "OK".

    For e.g.: Trial.txt
22. Exit WaveView by clicking on "EXIT" in the File Menu.
23. Switch "OFF" the WaveBook.
24. The saved file will be stored in:

    C:\Program Files\DaqX\Applications\ASCII

25. Open the file in "Microsoft Excel".
26. Select all the values that appear in the spreadsheet to plot a graph.
27. After selection, click on the Chart Wizard button in the Menu Bar.
28. Select a suitable chart type, which best depicts the nature of your graph. After selecting the chart type, press and hold to view the preview of the graph. If found satisfactory then click on next or choose some other type of chart. Click "NEXT".
29. Select the data range and series and then click "NEXT".
30. Provide a title, gridlines, legend, etc. to your graph and then click "NEXT".
31. Enter a name for your graph and give the location i.e. where you want to save the graph. Whether you want it as a new sheet or in the same sheet along with the spreadsheet.
32. Click on "FINISH".
33. Save the spreadsheet along with the graph at a desired location and take the print out of the graph.
34. Switch "OFF" your computer.

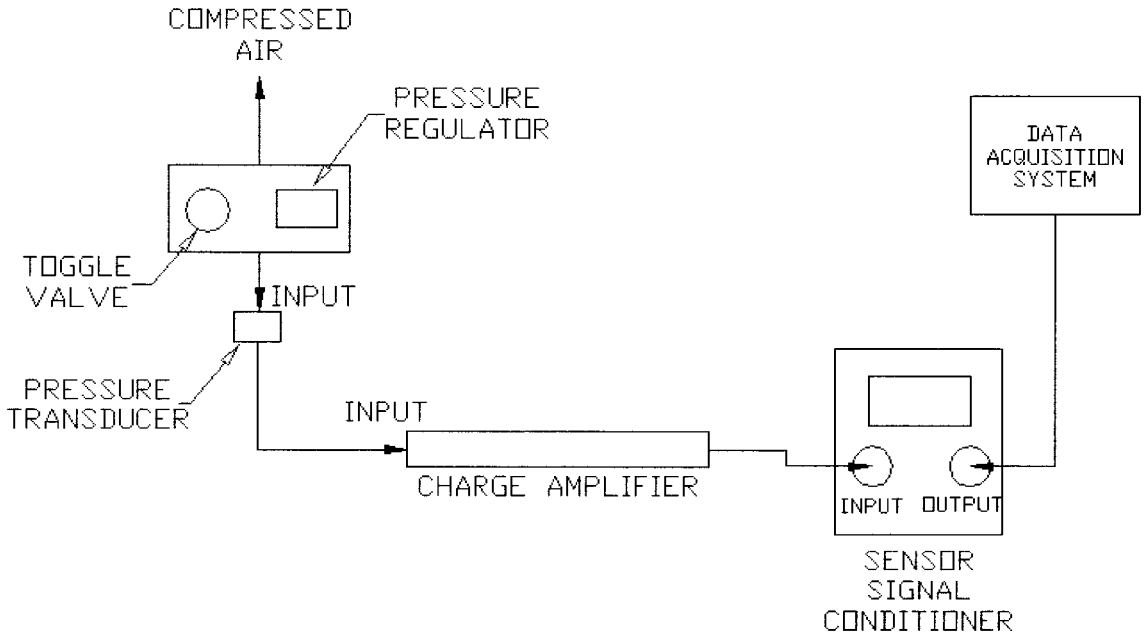

Figure A.1 Block diagram showing connections for testing data acquisition system.

Procedure 2:

Pressure Gauge Calibration Procedure

A pressure gauge calibration is conducted to assure that the applied and recorded pressures are correct. Continuous usage of such gauges results in loss of their accuracy and precision, and therefore these devices should be either calibrated or corrected manually. The calibration was done using a Mansfield & Green Twin Seal Pressure Test Unit (Type 10-2525, Serial No. 365-1). The procedure given below is used to calibrate gauges and to account for any kind of inaccuracies that may exist:

1. "OPEN" the pressure release valve and mount the pressure gauge to be tested on the unit via a quick-connect seal. After mounting, close the valve.
2. Use different weighing plates (such as Mansfield & Green type 1GT-208, 1GT-207, etc.) to load the piston and then use the pump to create pressure inside the piston chamber so as to counterbalance the weight applied on the piston.
3. As soon as, the plates are lifted off the support by the piston, the pressure gauge reading is recorded. This reading should match with the weight applied on the piston. If not, then gauge is manually adjusted to eliminate the error. This check is performed for each reading.
4. Readings are taken at every 10 psig. While calibrating low range (0-100 psig) gauges, loading of piston is done from 0 psig to 100 psig. However, for high range (0-200 psig and 0-300 psig) gauges loading is done from 0 psig to 200 psig.
5. After reaching maximum pressure, the plates are unloaded in 10 psig intervals and pressure is slowly released from the pressure chamber so that the piston is not forced out of the cylinder.
6. Readings are taken from the maximum test pressure to 0 psig. Again a check is performed to match the reading with the weight applied on the piston. If required, minor adjustments are done.
7. Once fully unloaded, the pressure release valve is opened to relieve any pressure remaining in the pressure chamber.
8. Steps 2-7 were performed for three gauges (i.e., gauge on reservoir tank, driver, and driven chamber).

9. A graph is plotted between actual and measured pressures for all the gauges. Theses graphs are shown in Fig. A.2, A.3, and A.4.
10. The tested pressure gauge is removed and any excess oil is wiped and cleaned from the connectors.

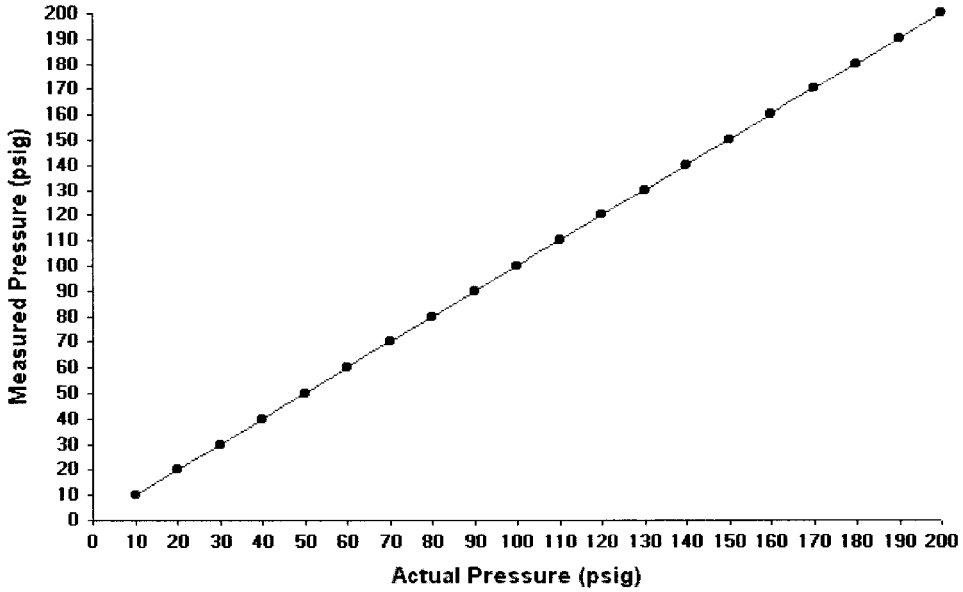

Figure A.2 Calibration chart for pressure gauge mounted at the reservoir tank (Serial No. 2089).

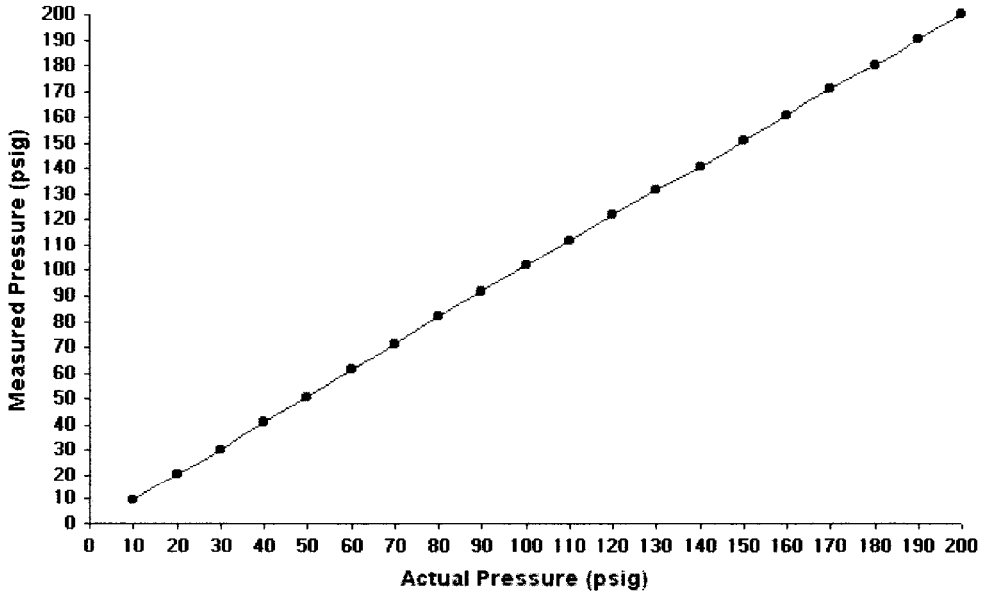

Figure A.3 Calibration chart for pressure gauge mounted at the driver chamber (Serial No. 435).

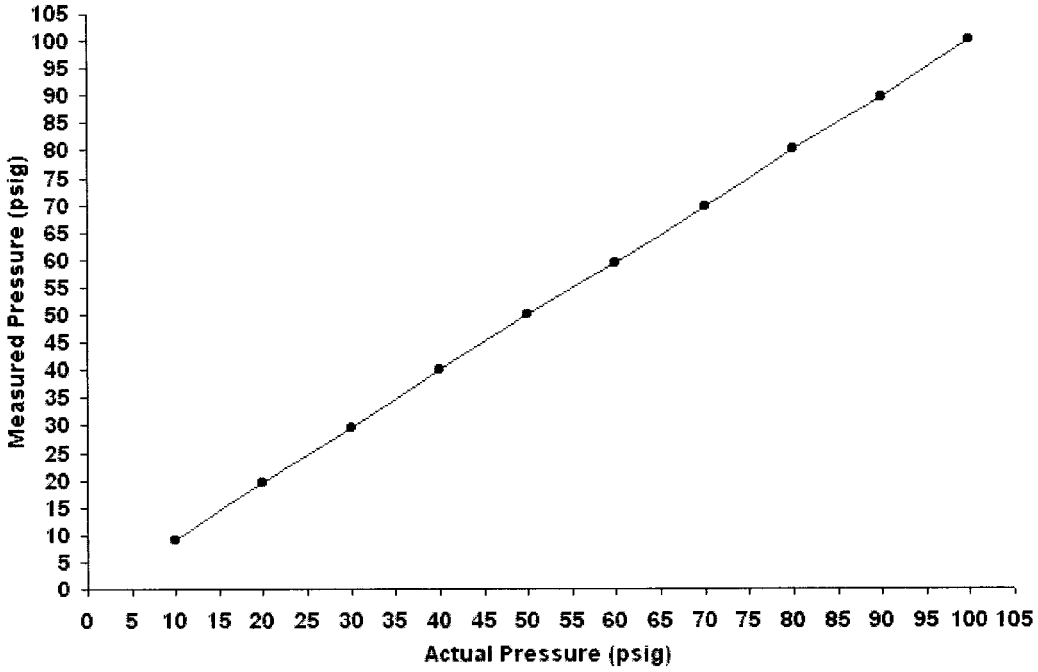

Figure A.4 Calibration chart for pressure gauge mounted at the driven chamber (Serial No. 8032).

Procedure 3:

Procedure for Determining Conversion Factor

This procedure is carried out to determine a conversion factor that allows converting the voltage reading obtained from the data acquisition system to a pressure reading (in Pa). The equipment consists of a pressure transducer, a sensor signal conditioner, an in-line charge amplifier, a data acquisition system (i.e., WaveBook), and a computer.

1. Using quick-release connectors, a pressure gauge and a push-button valve (i.e., toggle valve) are connected to the air reservoir tank.
2. Pressure transducer, sensor signal conditioner, and WaveBook are connected to the air supply from the compressor through a push-button valve. Ensure that the sensor signal conditioner gain is set to 1 so as to minimize the noise.
3. Switch "ON" the compressor.

4. WaveBook is initialized by setting the pre-trigger to 100 readings/scans, and the post-trigger to 9900 readings/scans. The triggering voltage is set at 0.002 mV.
5. The push-button valve is pressed to supply a trigger (i.e., a short burst of air to escape from the reservoir) at different pressures ranging from maximum of 100 psig to minimum of 10 psig.
6. Each time, a graph is plotted from the collected data, and the mean measured voltage is recorded.
7. Another graph of voltage versus pressure is plotted. A best-fitting line approach is used to find an equation representing these points. This is used to obtain a conversion factor, which allows the measurements in mV to be converted to psig. Such a conversion chart is shown in Fig. A.5.
8. Another measurement is taken, but this time the factor found in the previous measurement is used to produce the reading in psig.
9. If the reading produced the same pressure that is displayed on the pressure gauge attached to the air reservoir, then this conversion factor is recorded. If the factor is slightly off, an adjustment in the factor is done and another trial is conducted to ensure its accuracy.
10. Step 8 is repeated for as many times as needed to determine an accurate (within 1% error) conversion factor.
11. Steps 3-9 are repeated for different pressure values (as stated in step 5) at decreasing intervals of 10 psig.
12. The final conversion factors are recorded and graphed.

For the graph shown in Fig. A.5, the relevant straight line is

$$y = 0.0881x + 5.4748$$

Also, the x reading in mV is converted into V and a factor for conversion from psig to Pa is used. Hence, the final conversion equation is given by

$$y = ((0.0881 * 1000(x)) + 5.4748)(6894.7572)$$

The above equation is used for all the experimental results.

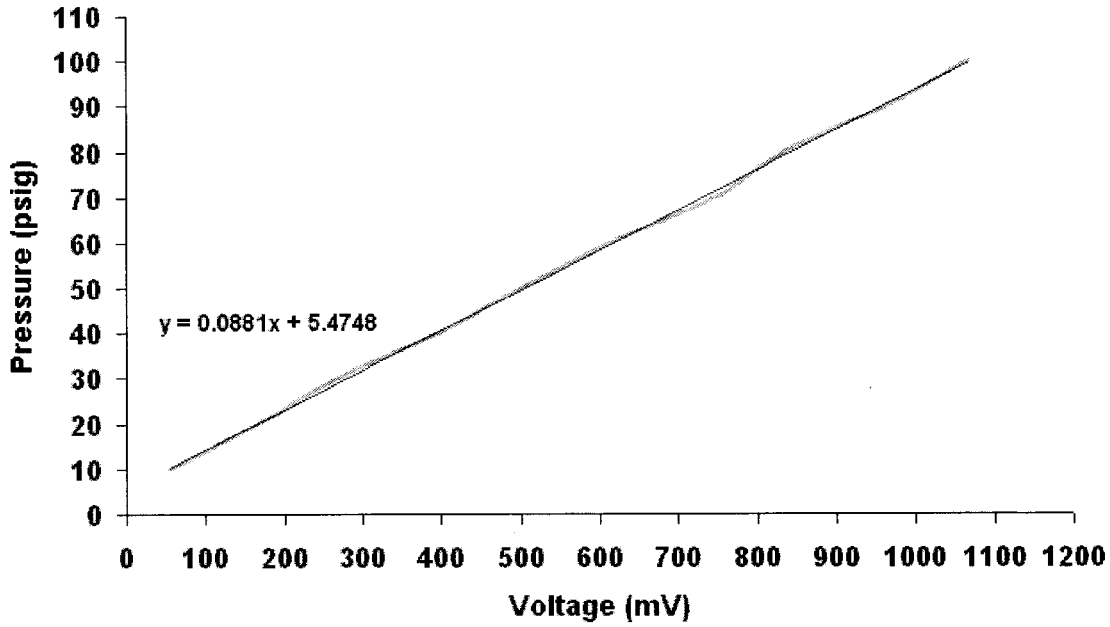

Figure A.5 Conversion chart for converting mV reading to psig reading.

Procedure 4:

Preliminary Test Procedure

Before conducting actual experimental firings, a preliminary test is performed to check for air leakage through pipe, coupling, and fittings and to verify proper mechanical working of the apparatus. This particular test is conducted without a diaphragm i.e., the diaphragm holder is empty, and in the absence of data acquisition equipment. The procedure for such a test is given below. While conducting the test, one should make sure that all the safety requirements are met and safety gear is worn.

1. Open the water tap so that water is filled in the cooling jacket of the compressor.
2. Switch "ON" the compressor by shifting the red switch located on the switchboard to "AUTO" position.
3. Make sure that the isolation ball valve is closed so that high-pressure air does not pass through the shock tube. Once, the maximum pressure in the reservoir tank is attained, the compressor will automatically shut down.

4. Open the air supply to the driver and driven chamber and check for air leakages; if any are found, try to eliminate them.
5. Check that there is no water or there are no dust particles in the separator, as moisture in the air might get condensed. Take out the water by opening the valve at the bottom of the separator. Don't forget to close this valve.
6. Pass some air through the shock tube so that there are no dust particles in the shock tube.
7. Open the nozzle and blow some air to remove any ruptured diaphragm pieces that may be left inside the shock tube from previous firings.

Procedure 5:

Procedure for Connecting the Pressure Transducer with the Shock Tube and the Data Acquisition System

1. Place the transducer in the pressure transducer tap and snug it (with extra care) with the help of a wrench. One should not apply excess pressure while tightening the transducer. Make sure that the transducer is mounted properly.
2. Connect one end of the co-axial cable along with the charge amplifier to the transducer mounted on the shock tube and the other end to the sensor signal conditioner (Model No.: 480E09). This end is connected to a socket named as "XDCR" on the Signal Conditioner.
3. Adjust the gain of the sensor signal conditioner to 1. This completes the connection of the transducer with the shock tube. These connections are shown in the form of block diagram in Fig. 2.20.
4. The data acquisition system (i.e., WaveBook) provides a number of channels so that number of devices can be connected to collect data. For the present experimentation, only sensor signal conditioner is connected to the system. Another co-axial cable is used to connect "CH1–ANALOG TRIGGER" of the system with "SCOPE" on the sensor signal conditioner. This completes the connection of the WaveBook with the sensor signal conditioner.

5. After all the connections are done, one should make sure that the battery in the sensor signal conditioner is charged, otherwise replace the battery. This can be done by shifting or pressing the red switch on the sensor signal conditioner to the "BATT TEST". As soon as the switch is pressed, the needle should move to the yellow region, which indicates that the battery is "OK" or has enough power. Within few seconds, the needle will automatically move to the green region, which indicates that the sensor signal conditioner is ready for use.
6. Once the data are being collected, switch "OFF" the red button on the sensor signal conditioner.

Procedure 6:

Procedure for Connecting the Data Acquisition System with the Computer

1. Place the data acquisition system (i.e., WaveBook) in a convenient position near the computer so that the connections with the computer can be done easily.
2. Connect the WaveBook to the required parallel port of the CPU with the help of a communication cable supplied with the WaveBook. The other end is connected to the WaveBook in the socket named as "TO COMPUTER".
3. Power supply is given to the WaveBook with the help of an adapter, which is connected to the socket named as "POWER IN". The power that can be supplied to the WaveBook is in the range of +10 V D.C. to +30 V D.C. This completes the connection of WaveBook with the computer. The block diagram is shown in Fig. A.6. The details of the adapter are:
    a) Company Name: GlobTek Inc.
    b) Serial No.: TR9CG2700N05-A1.
    c) Model No.: AD-740U-1150.
    d) Input: 100 V-240 V, 1 A, 50-60 Hz.
    e) Output: 15 V, 2.7 A.

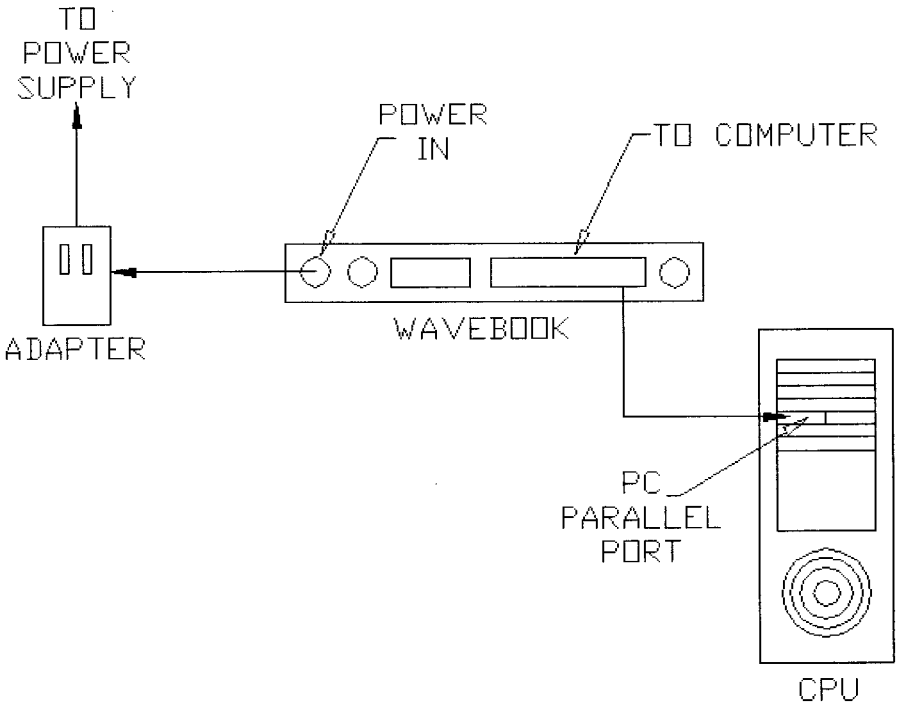

Figure A.6 Block diagram for connecting the data acquisition system with the computer.

Procedure 7:

Procedure for Initializing the Data Acquisition System

Once all the connections are done for the data acquisition equipment, it is necessary to initialize the data acquisition system (i.e., WaveBook) so as to collect the data.

1. Position the Data Acquisition equipment in such a way that the user has an unobstructed view of the monitor.
2. Switch "ON" the computer.
3. Once the computer is switched ON, then only switch "ON" the WaveBook by pressing the black power switch to position "1" (provided at the back of the WaveBook).
4. Double click the WaveView icon on the desktop of the computer so that the data acquisition software (i.e., WaveView) is started and one can see a window titled

as WAVEVIEW.CFG (WaveBook 0) having information about the number of channels in the channel configuration frame.

5. Click on the Edit Menu. Select the suitable options like Show All Channels, Hide Inactive Channels, etc.
6. Click on the View Menu. Set the Acquisition and Module Configuration separately. Both of the configuration set-ups are described in detail in the procedure 1.
7. Click on the System Menu. Click on the Select Device, after clicking a Select Device dialog box will be opened. Make sure you select the WaveBook 0 option otherwise the software will run in the Simulated Device mode and will not capture data. After selecting WaveBook 0, click "OK".
8. At this stage, all the settings in the software have been done. The system is ready for collecting the data.
9. Open the Scope window. Click the Arm (green arrow in the Menu Bar). After 5 scans, perform the actual experimental firing.
10. Save the data.
11. Click the cross button in the upper right corner so as to close the scope window.
12. Exit the data acquisition software by clicking Exit in the File Menu.

Procedure 8:

Actual Firing Procedure

Once the preliminary test is carried out, connect the data acquisition equipment to the shock tube. In this test, place a diaphragm in the diaphragm holder. Again all the safety requirements should be met and the safety gear must be worn. Steps listed below must be followed to obtain results from the apparatus.

1. Open the water tap so that water is filled in the cooling jacket of the compressor.
2. Switch "ON" the compressor by shifting the red switch located on the switchboard to "AUTO" position.
3. Make sure that the isolation ball valve is closed. Once, the maximum pressure is attained in the air reservoir tank, the compressor will automatically shut down.

4. Load the diaphragm and the desired nozzle (as firings are conducted with different nozzle geometries) at the end of the driven chamber, make sure all the pressure gauges and thermocouples are mounted properly, and the data acquisition system is initialized to capture the data.
5. Open the air supply to the driven (primary) chamber and try to maintain a desired pressure level (as firings are conducted at 340 kPa, 375 kPa, 409 kPa, and 444 kPa pressure levels in the driven chamber). While doing so, one may have to use additional air supply from the air reservoir tank, depending on the air pressure in the university's main air distribution line.
6. Simultaneously, pressurize the driver (secondary) chamber and note the pressure from the pressure gauge at which the diaphragm is ruptured.
7. As soon as the diaphragm is ruptured, one should get a number of peaks in the scope window of WaveView (i.e., data acquisition software). This means that data have been collected. One has to verify whether the data is correct or not.
8. Save the data.
9. Once the experiment is finished, open the nozzle and blow some air so that if there are any ruptured diaphragm pieces, they are removed.
10. If some more experiments are to be conducted then place a new diaphragm in the holder and repeat steps 5 to 8.
11. Once all the firings are conducted, follow the shutdown procedure.

Procedure 9:

Shutdown Procedure

After performing the actual experimental firing, shut down procedure should be followed as a part of safety requirement.

1. As soon as the diaphragm is ruptured, cut-off the air supply to the (driven) primary and (driver) secondary pressure chambers by closing the respective valves.
2. Switch "OFF" the compressor. Close the running water supply to the cooling jacket of the compressor.

3. Shutdown the power of WaveBook. Shutdown the computer.
4. Disconnect the transducer from the WaveBook and the shock tube. Switch "OFF" the sensor signal conditioner. Keep the transducer in a safe place so as to avoid any damage.
5. Replace the ruptured diaphragm from the diaphragm holder.
6. Gather all the tools used while conducting the experiment and keep them in the toolbox. If necessary, one should clean the tools.
7. Make sure all the electrical plugs, and switches are disconnected.
8. Clean the place near the apparatus.
9. Switch "OFF" the lights in the laboratory where the experiment was conducted.
10. Lock and shut the door while leaving the laboratory.

Appendix B LABORATORY SAFETY CONSIDERATIONS

While designing and manufacturing any experimental equipment, safety should be one of the important issues. The equipment should pose minimum risk to human health. In the present study, the independent variables of the overall system (i.e., the experimental apparatus) that may cause concerns are identified and discussed below. The basic safety requirements that should be taken into considerations are as follows:

1. Various safety messages are posted at the entrance to the laboratory and at the location where the experiment is being conducted. Hence, it is advised to follow these instructions carefully before entering the laboratory or conducting the experiment, to avoid any damage to human health.
2. Around the experimental apparatus, a yellow and black caution line has been drawn. While conducting the experiment, one should stay behind this line. In other words, do not cross the yellow line.
3. The apparatus includes piping, fittings, couplings, small valves, etc., so due to high operating pressures and long, continuous operation of the apparatus, this may the lead to loosening of some joints. Hence, it may happen that some parts may fly off, though extra care has been taken during the assembly of the apparatus. Therefore, eye protection, such as workshop goggles, must be worn. If possible, head protection, like a workshop helmet, should also be worn.
4. The sound pressure levels emitted from the nozzle are high similar to jet noise. The net estimated sound pressure level is 129 dB. Hence, it is highly recommended to wear ear protection, otherwise damage to hearing may occur.
5. As described in the shut down procedures (see Appendix A), one should switch off all the lights in the laboratory and cut down the power supply to the equipment, so as to avoid any kind of short circuit or electrical damage to the apparatus. Short circuits may cause fire hazards.

Appendix C STARTING FLUENT ON A UNIX SYSTEM

The numerical simulations are generated on Sun Microsystems computer machines installed in the Advanced Computational Laboratory (i.e., ATOP Lab at T-345, Ryerson University). These machines consist of fast processors having sufficient memory for conducting CFD analysis, and run on UNIX Operating System. FLUENT Version 6.0 is pre-installed on these machines.

The following section describes how to start FLUENT on a UNIX system and also provides a step-by-step procedure of how to select various menus given in FLUENT to run a simulation.

One has to supply a login name and password (provided by network administrator at the ATOP Lab) to use any of the computer machines in the ATOP Lab. Once login name and password is provided, open a terminal window so that commands can be executed at the command line of the terminal window. There are several ways to start FLUENT on a UNIX Operating System:

1. Start FLUENT by supplying the appropriate version at the command line.
2. Start the solver from the command line without specifying a version, and then use the "Select Solver panel" to choose the appropriate version.
3. Start the solver from the command line without specifying a version, and then read a case file (or a case file and data file) to start the appropriate version.

Among the various ways, simplest way to start FLUENT is by providing the appropriate version at the command line. FLUENT consists of single-precision and double-precision solvers. Along with it one can define the dimensionality, i.e., 2D and 3D of the problem. In order to generate simulations for the present case, "FLUENT 2d" command is executed at the command line. This command runs a 2-dimensional, single-precision solver. After initializing the solver, read the grid/mesh file in FLUENT and apply the various input parameters (discussed in Section 3.4).

A step-by-step procedure is prepared which describes the various menus used to input various parameters and solve a problem.

1. Read the grid/mesh file.

   File→Read→Case

2. Check the grid and grid scale.

   Grid→Check

   Grid→Scale

   Display→Grid

3. Define units for the problem.

   Define→Units

4. Define the various models used to solve the problem.

   Define→Models→Solver

   Define→Models→Viscous

   Define→Models→Energy

5. Define physical properties of materials and operating conditions.

   Define→Materials

   Define→Operating Conditions

6. Define boundary conditions.

   Define→Boundary Conditions

7. Define custom field functions to apply specific values to different regions/zones defined in the geometry.

   Define→Custom Field Function

8. Provide controlling parameters for solution.

   Solve→Controls→Solution

9. Initialize the solution.

   Solve→Initialize→Initialize

10. Patch custom field functions.

    Solve→Initialize→Patch

11. Plot residuals.

    Solve→Monitors→Residual

12. Save the input file.

    File→Write→Case

13. Iterate the solution.

    Solve→Iterate

14. Create surface points to collect static pressure.

Surface→Point

15. Define surface monitors.

    Solve→Monitors→Surface

16. Save the solution.

    File→Write→Data

17. Displaying the solution.

    Display→Contours

    Display→Velocity Vectors

    Plot→XY Plot

18. After saving the input and output files, exit/close the solver.

    File→Exit

19. Once the simulation is completed, close the terminal window and don't forget to logout.

Appendix D INPUT CONDITIONS FOR FLUENT

Boundary conditions:

The various boundary conditions discussed in Section 3.4.6 are listed below:

1. **INFLOW:**

   Boundary Type: mass-flow-inlet

   Mass flow Specification Method: mass flow rate

   Mass flow rate: 0.0430 kg/s (calculated in Section 2.2.2)

   Total Temperature: 294 K (Room temperature)

   Supersonic/Initial gauge pressure: 3.7 atm (determined in Section 2.2.2)

   Direction Specification Method: Direction Vector

   Axial-Component of flow direction: 0

   Radial-Component of flow direction: -1

   Turbulence Specification Method: Intensity & Viscosity Ratio

   Turbulence Intensity (%): 5 (common value for fully-developed, internal flow)

   Turbulence Viscosity: 2

2. **FAR-1:**

   Boundary Type: pressure-far-field

   Gauge pressure: 1 atm

   Mach number: 0

   Temperature: 294 K

   Axial-Component of flow direction: 1

   Radial-Component of flow direction: 0

   Turbulence Specification Method: Intensity & Viscosity Ratio

   Turbulence Intensity (%): 1 (low turbulence value at far-off location)

   Turbulence Viscosity: 1

3. **FAR-2:**

   Boundary Type: pressure-far-field

Gauge pressure: 1 atm

Mach number: 0

Temperature: 294 K

Axial-Component of flow direction: 0

Radial-Component of flow direction: -1

Turbulence Specification Method: Intensity & Viscosity Ratio

Turbulence Intensity (%): 1

Turbulence Viscosity: 1

4. **OUT-1:**

Boundary Type: pressure-outlet

Gauge pressure: 1 atm

Backflow total temperature: 294 K

Turbulence Specification Method: Intensity & Viscosity Ratio

Turbulence Intensity (%): 1 (low value at far-off location)

Turbulence Viscosity: 1

5. **OUT-2:**

Boundary Type: pressure-outlet

Gauge pressure: 1 atm

Backflow total temperature: 294 K

Turbulence Specification Method: Intensity & Viscosity Ratio

Turbulence Intensity (%): 1

Turbulence Viscosity: 1

6. **OUT-3:**

Boundary Type: pressure-outlet

Gauge pressure: 1 atm

Backflow total temperature: 294 K

Turbulence Specification Method: Intensity & Viscosity Ratio

Turbulence Intensity (%): 1

Turbulence Viscosity: 1

7. **RESERVOIR END:**

   Thermal Condition: Heat flux

   Heat flux: 0 W/m^2

   Wall thickness: 0

   Heat Generation Rate: 0

   Roughness Height: 0.0001 m

   Roughness Constant: 0.5

Custom field functions:

The various custom field functions applied to different regions in the model flow geometry are listed below:

1. **For Region 1:**

   $p_0 = 881527.5$ Pa

   $u_0 = 0$ m/s

   $T_0 = 294$ K

2. **For Region 1,2,3:**

   $p_3 = 374902.5$ Pa

   $u_3 = 4.777$ m/s

   $T_3 = 294$ K

3. **For Region 4:**

   $$p_4 = 374902.5 - 176841.51\left(\frac{x-2.3}{0.0215}\right) \text{ Pa}$$

   $$u_4 = 4.777 + 308.986\left(\frac{x-2.3}{0.0215}\right) \text{ m/s}$$

$$T_4 = 294 - 49\left(\frac{x-2.3}{0.0215}\right) \text{ K}$$

4. **For Region 5:**

   $p_5 = 198060.99$ Pa

   $u_5 = 313.756$ m/s

   $T_5 = 245$ K

5. **For Region 6:**

$$p_6 = 198060.99 - 193003.702\left(\frac{x-2.3225}{0.023}\right) \text{ Pa}$$

$$u_6 = 313.756 + 332.824\left(\frac{x-2.3225}{0.023}\right) \text{ m/s}$$

$$T_6 = 245 - 159.09\left(\frac{x-2.3225}{0.023}\right) \text{ K}$$

The above custom field functions are determined by the values of dependent variables (only p, u, and t in our analysis) in Section 2.2. However, functions for Region 4 and Region 6 also include dependency in terms of x (i.e., grid location).

Solution Control Parameters:

1. **Under-Relaxation Factors:**

   Solid: 1

   Turbulence Kinetic Energy: 0.8

   Turbulence Dissipation Rate: 0.8

   Viscosity: 1

2. **Discretization:**

   Flow: Second Order Upwind

   Turbulence Kinetic Energy: Second Order Upwind

   Turbulence Dissipation Rate: Second Order Upwind

3. **Solve Parameters:**

   Courant number: Ranging from 1 to 5 for steady-state calculations and 0.75 for transient state calculations.

Variables to be monitored and checked for convergence:

1. Normalization Scheme: Scaled Residuals
2. Print and Plot residuals
3. Continuity: Monitoring, check for convergence with criteria of 1×10^{-5}
4. X-Velocity: Monitoring, check for convergence with criteria of 0.001
5. Y-Velocity: Monitoring, check for convergence with criteria of 0.001
6. Energy: Monitoring, check for convergence with criteria of 0.001
7. Thermal Conductivity: Monitoring, check for convergence with criteria of 0.001
8. Epsilon: Monitoring, check for convergence with criteria of 0.001

Appendix E PARTS LIST FOR EXPERIMENT

Part Name	Manufacturer	Model Number	Serial Number	Range
Pressure Gauges:				
On driven chamber	Wika		8032	0-100 psig
On driver chamber	Wika		435	0-200 psig
On reservoir tank	Weksler Inc.		2089	0-300 psig
Reservoir Tank:	Ferro Metal Ltd.	QM-40-12C	6995	Max Pres. 170 psig
2-Stage Compressor:	Ingersol Rand	15TX type 30	18520	48 cu. ft.
Regulator:	Schrader Bellows		3566-2000	5-125 psig
Filter:	Schrader Bellows		3536-1000	Max Pres. 150 psig
Diaphragm:				Polyester film having thickness of 0.0000889 m
Diaphragm Holder:	Pro-Quip			Diameter of 0.0508 m
Nozzle:				0.0508mX0.007870mX0.0203m
Pressure Transducer	PCB PIEZOELEC-TRONICS Inc.	112A02	17993	0-1000 psig
Charge Amplifier	PCB	422 D02	6245	
Sensor Signal Conditioner	PCB	480 E09	24568	
DAQ System	IOtech	Wavebook/516	201727	
DAQ Software	IOtech	WaveView V7.8.104		
Thermocouple:	Decktronic	10-K1		

Appendix F PHOTOGRAPHS OF APPARATUS

Photographs of various components installed in the shock tube apparatus are shown below.

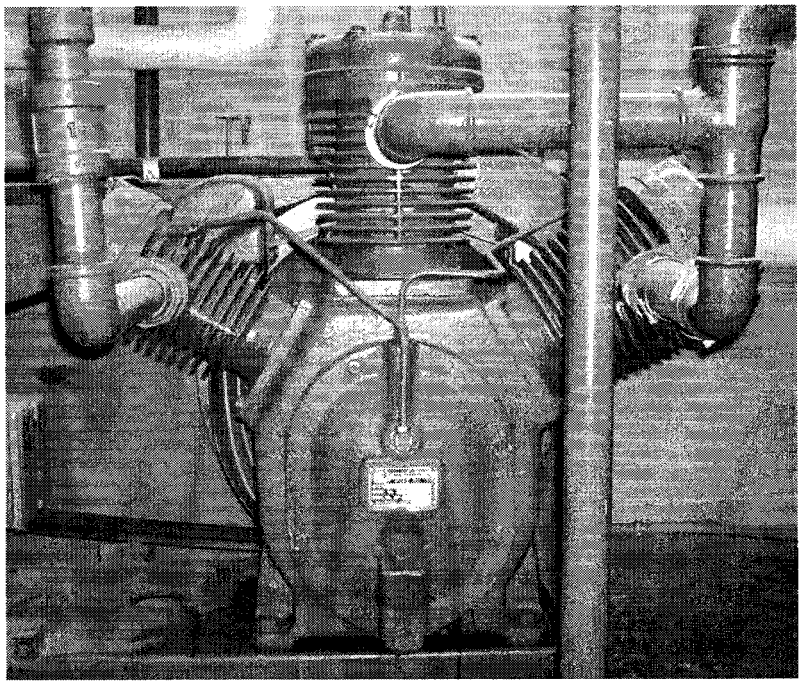

Figure F.1 Two-stage air compressor.

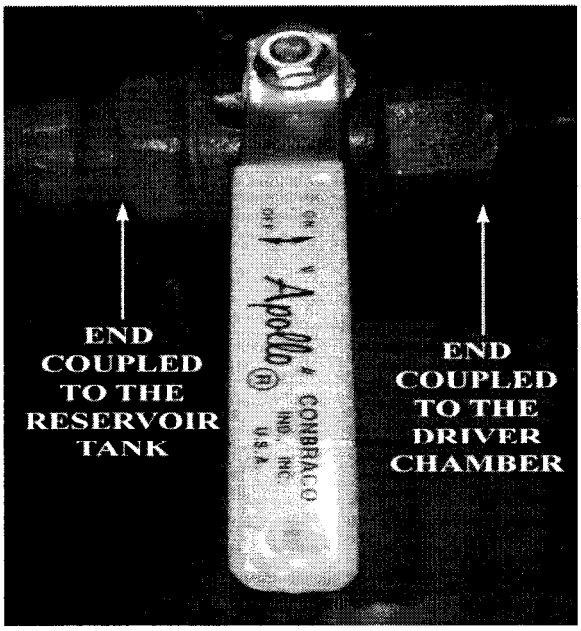

Figure F.2 Isolation ball valve.

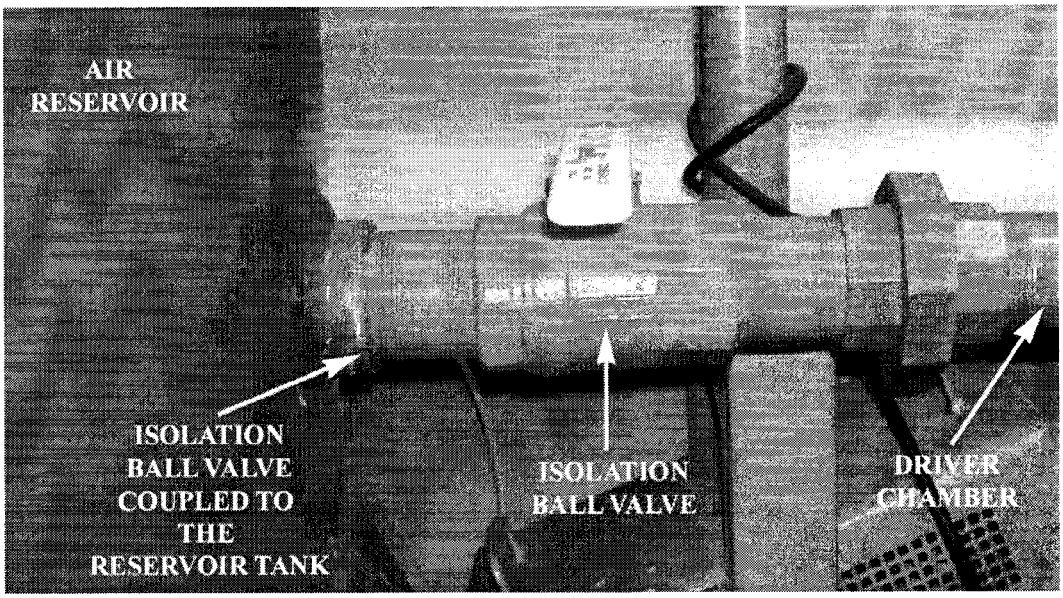

Figure F.3 Air reservoir connected to the driver chamber through an isolation ball valve.

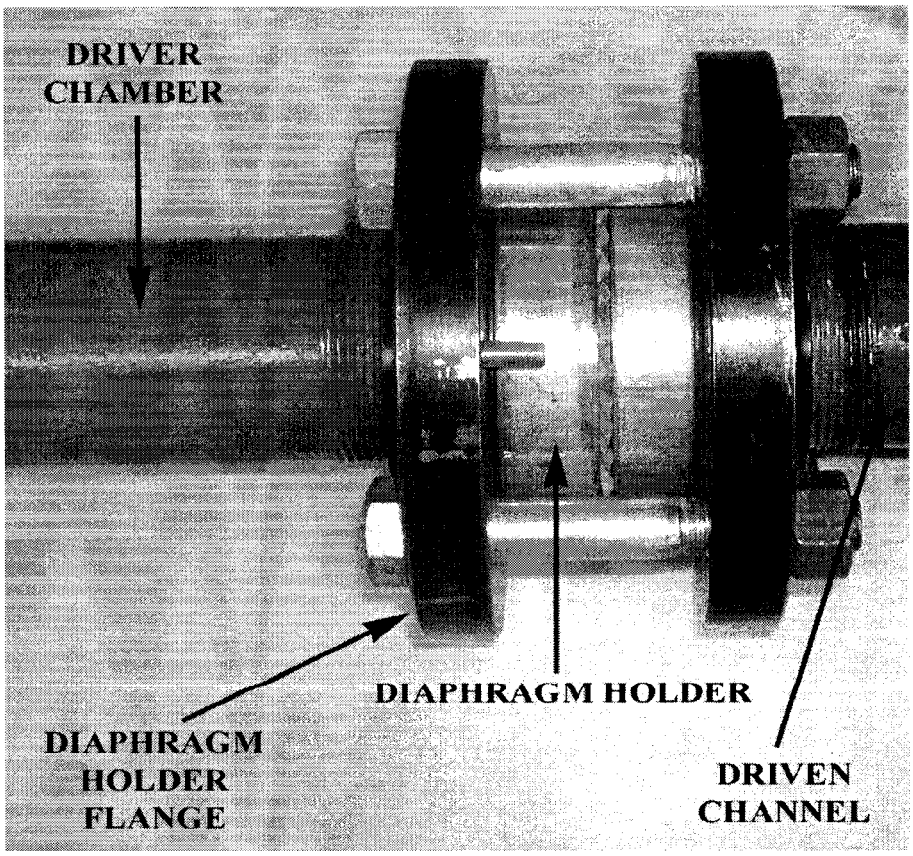

Figure F.4 Diaphragm holder assembly.

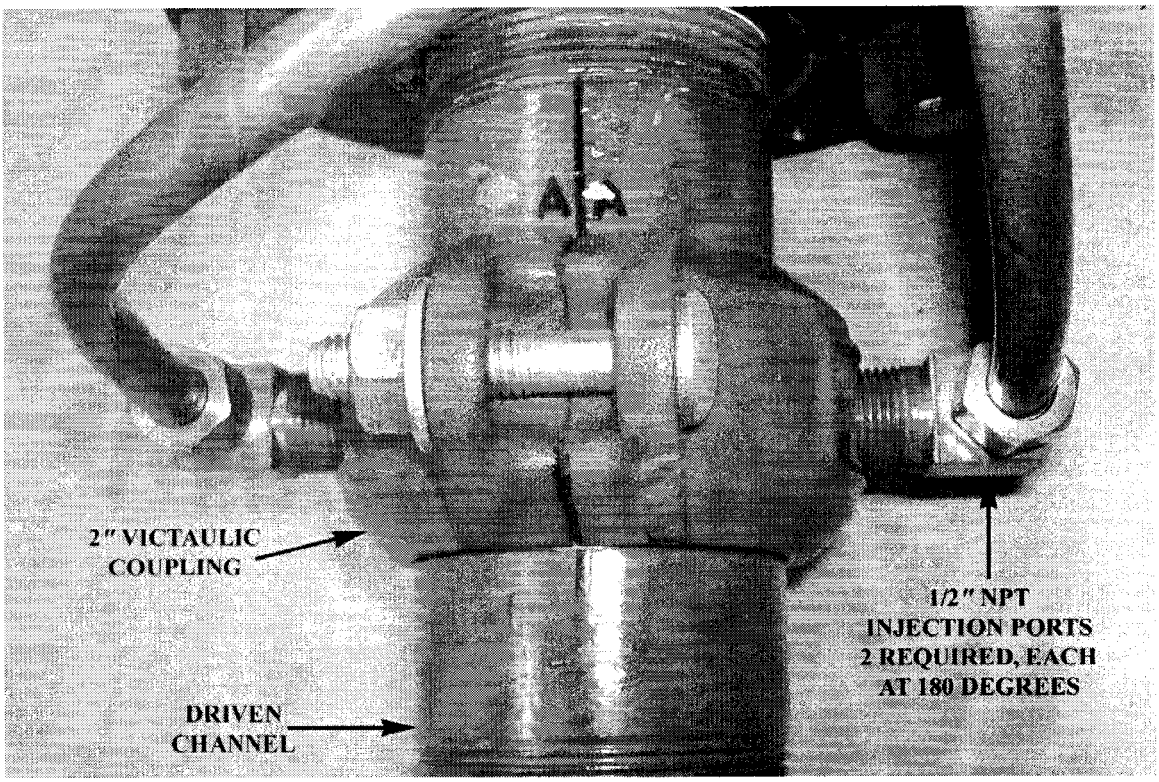

Figure F.5 Primary inlet air assembly.

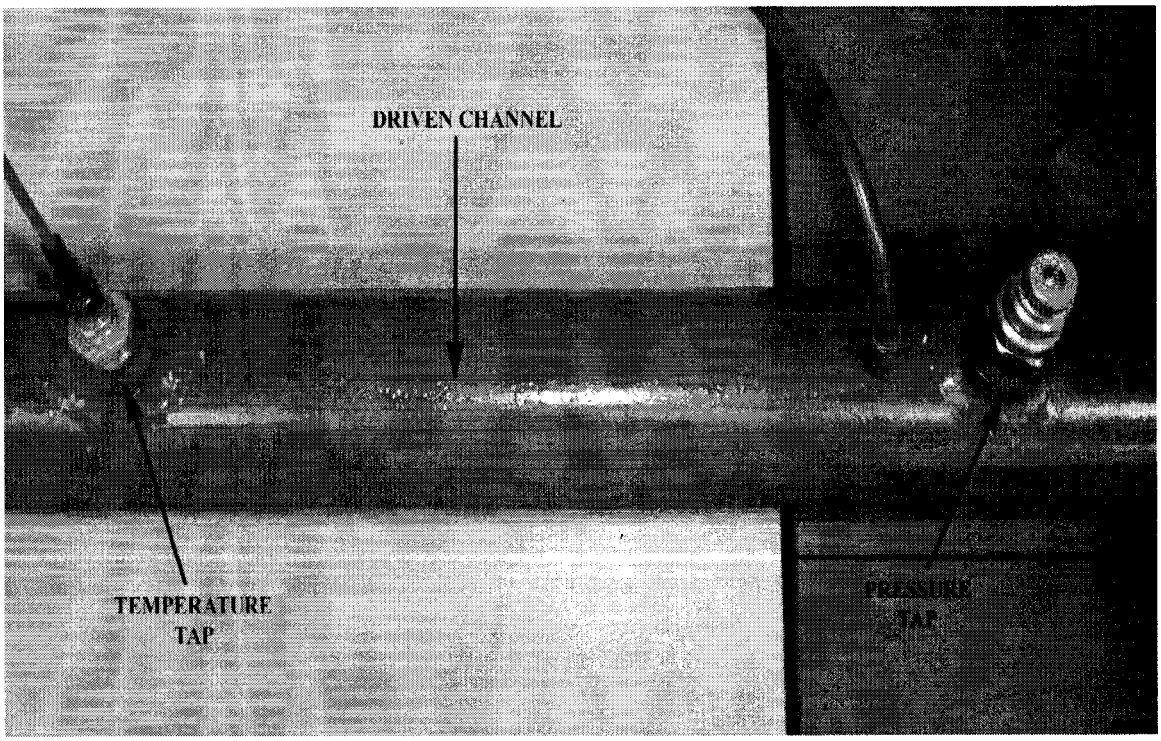

Figure F.6 Pressure and temperature taps.

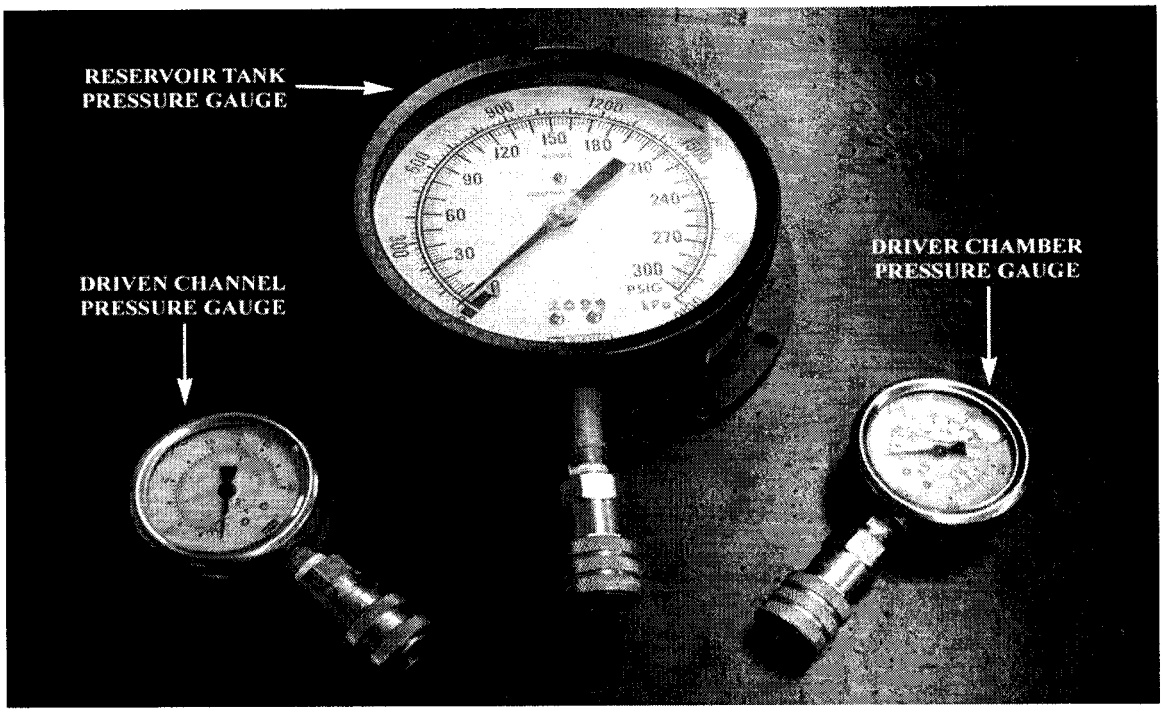

Figure F.7 Different pressure gauges employed at different locations.

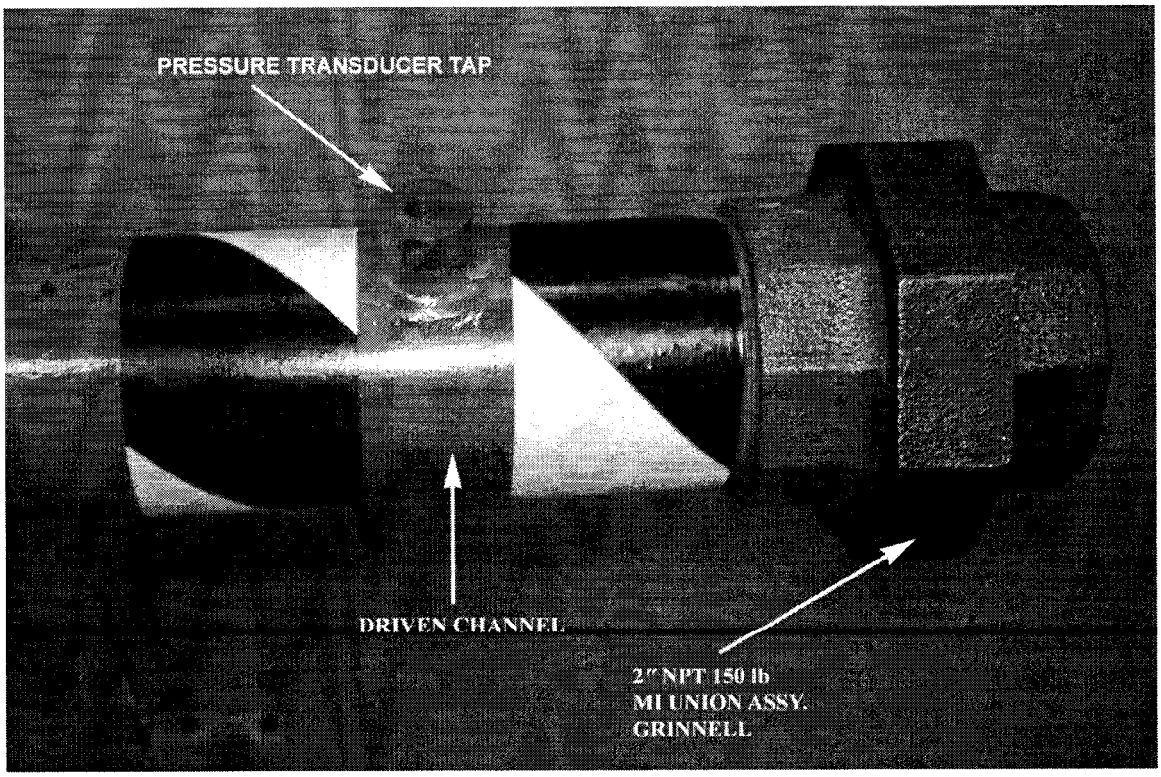

Figure F.8 Exhaust end of the shock tube.

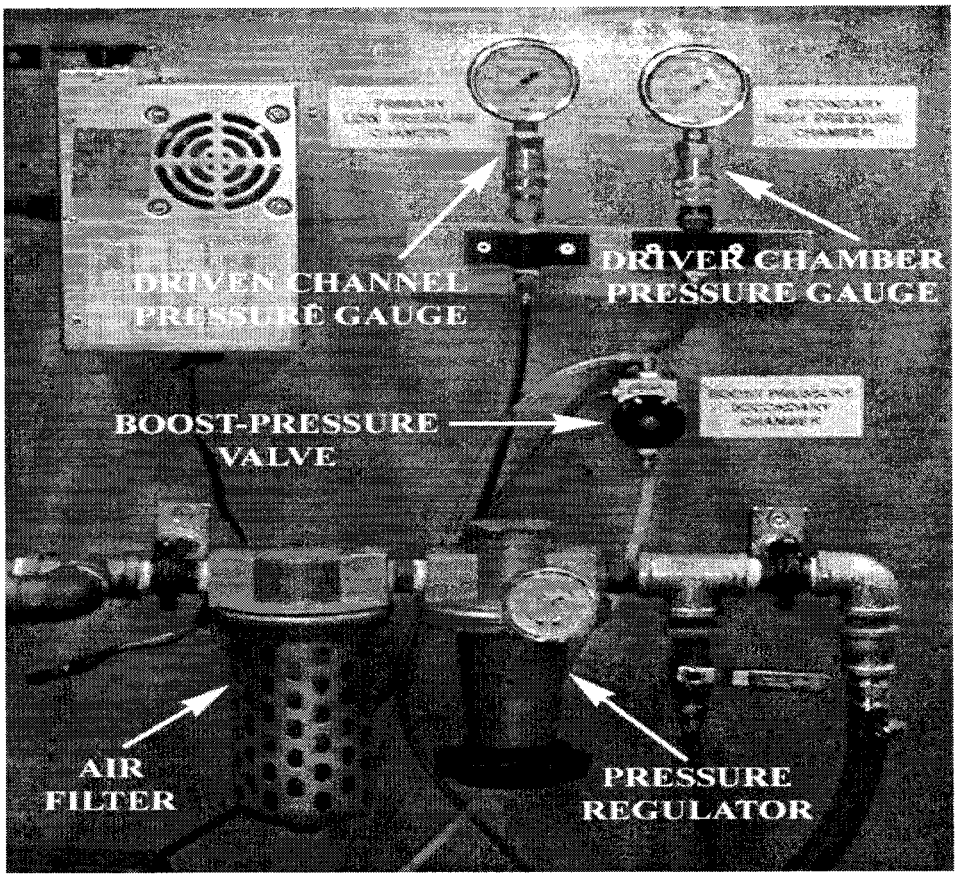

Figure F.9 Control panel of the shock tube apparatus.

Figure F.10 Convergence region of the nozzle.

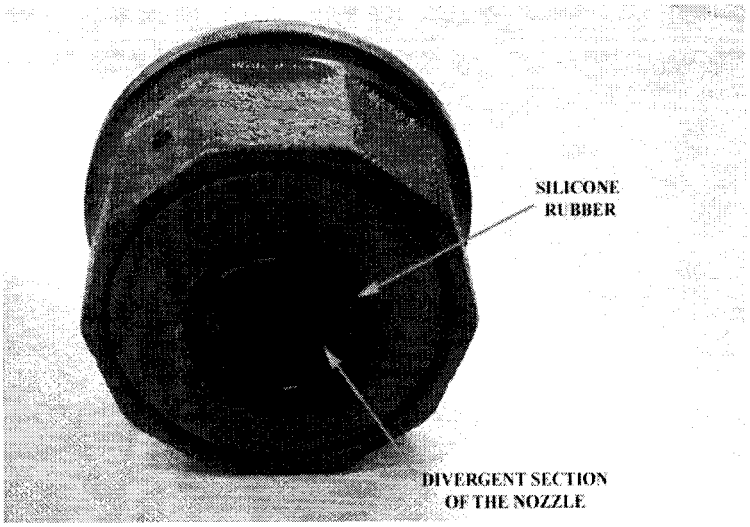

Figure F.11 Exit section of the nozzle.

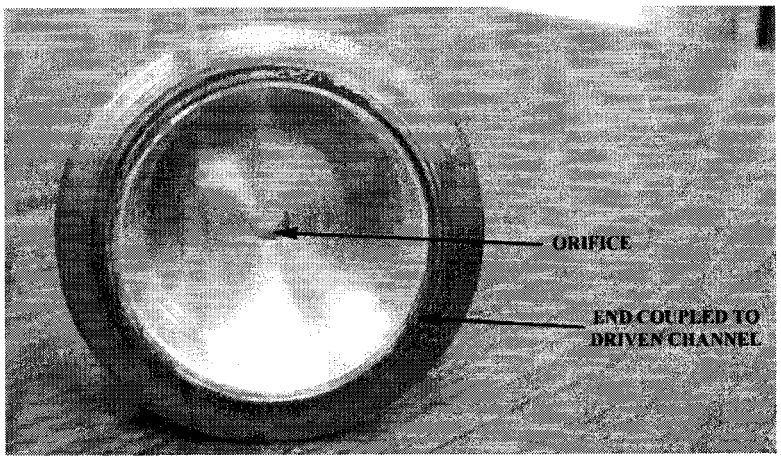

Figure F.12 Orifice plate.

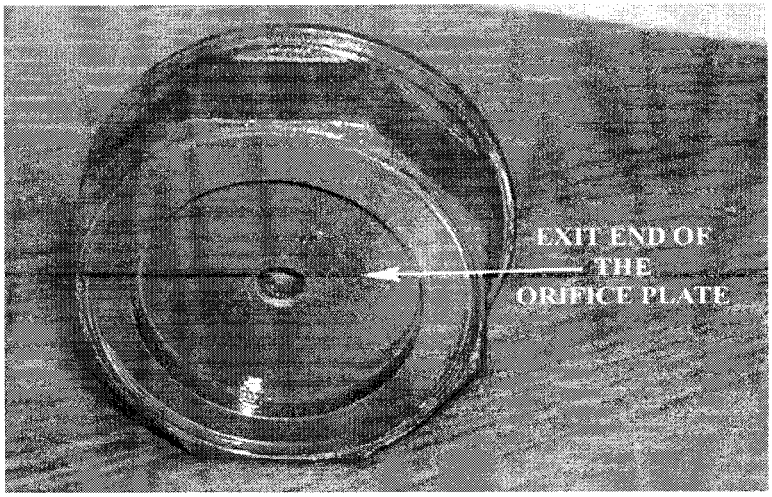

Figure F.13 Exit section of the orifice plate.

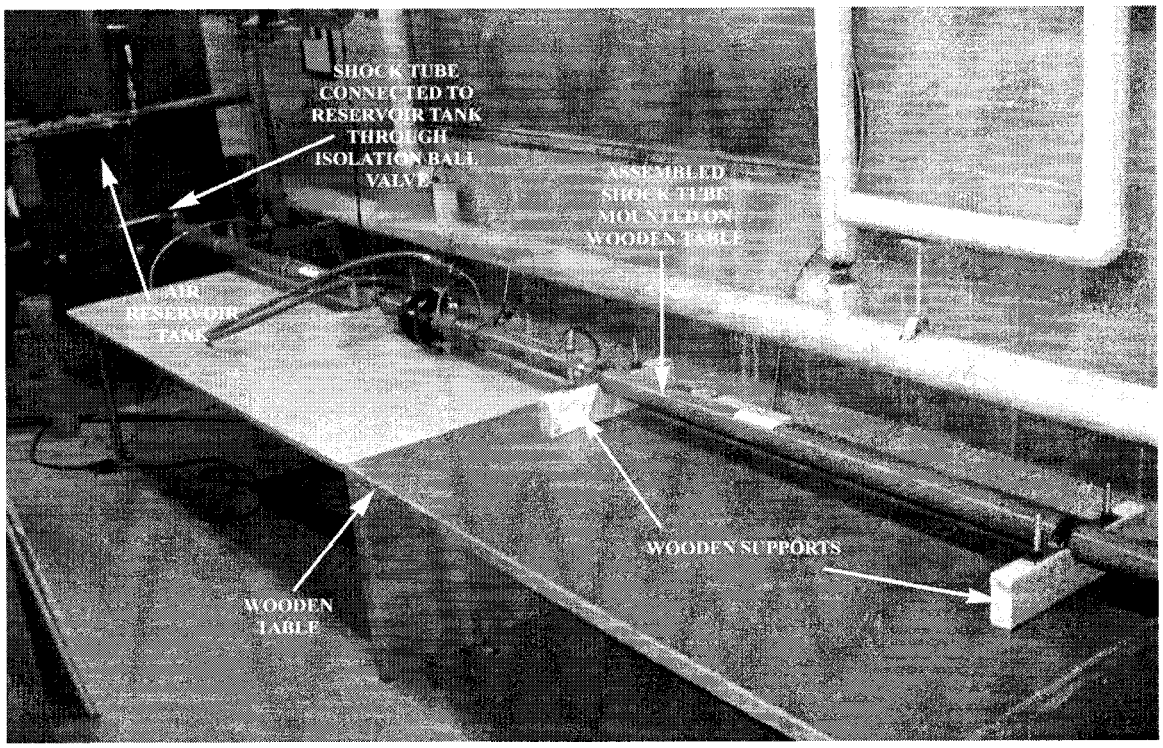

Figure F.14 Shock tube assembly.

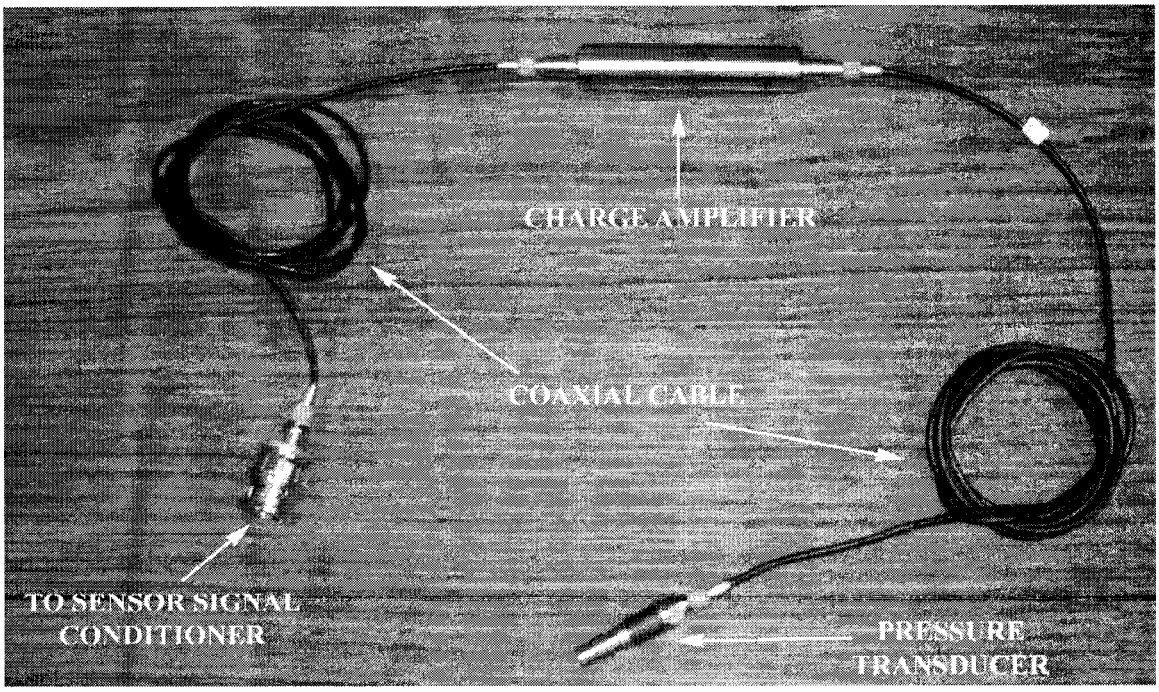

Figure F.15 Various components used to connect data acquisition system with a desktop PC.

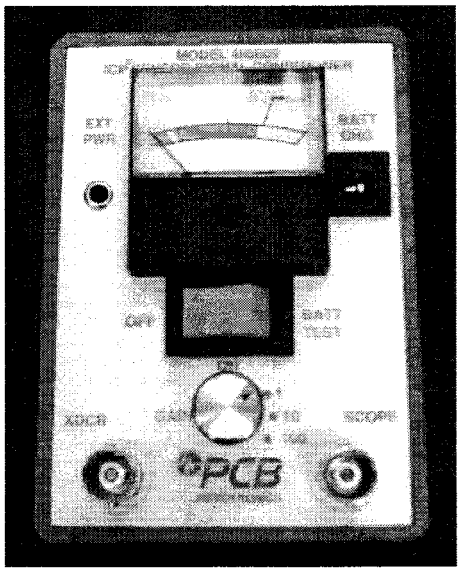

Figure F.16 Sensor signal conditioner.

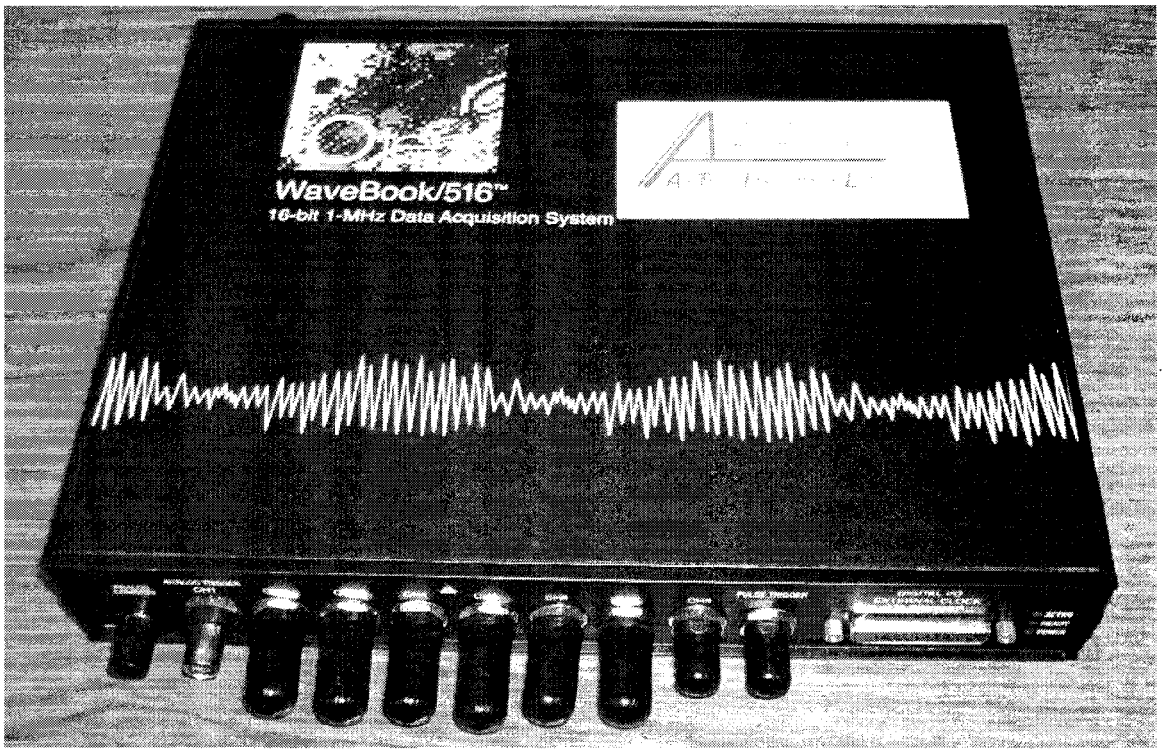

Figure F.17 High-speed data acquisition system.